Department of Physics and Astronomy
University College London
University of London

Investigation of the interaction of water with the calcite $\{10\bar{1}4\}$ surface using ab-initio simulation

Jennifer Susan Lardge

Submitted for the degree of
Doctor of Philosophy
at University College London
April 2009

I, Jennifer Susan Lardge confirm that the work presented in this thesis is my own. Where information has been derived from other sources, I confirm that this has been indicated in the thesis.

Abstract

Density functional theory calculations were employed to explore the interaction between water and the $\{10\bar{1}4\}$ surface of calcite. In addition a defective $\{10\bar{1}4\}$ surface and stepped surfaces in contact with water were investigated. A series of percentage water coverages and water configurations were explored, including dissociated water states. Static relaxations found associated water to be favourable on the $\{10\bar{1}4\}$ surface, although a metastable dissociated state 1.77eV higher in energy was found. Molecular dynamics (MD) simulations of low water coverage reveal fluctuations in the H-O_{water} bond when the H atom is directed towards a surface CO_3 ion. Desorption of an H_2O molecule was observed in simulations above 900K. Water was found to be strongly bound to the perfect $\{10\bar{1}4\}$ surface, with an adsorption energy of -0.91eV. MD simulations of a defective $\{10\bar{1}4\}$ surface found water to favour dissociation at CO_3 vacancies. However, water at Ca vacancies diffused across the surface to form a bond with the nearest surface Ca ion. Water was also found to favour an associated state at both acute and obtuse steps. On all these imperfect surfaces water was found to adsorb strongly to the surface, with adsorption energies ranging from -0.99eV to -1.60eV.

Acknowledgements

I would like to thank Dr Dorothy Duffy and Prof. Mike Gillan for their guidance and support during the past three and a half years. It is thanks to their knowledge and skill that I have reached this point.

Thanks must also go to Colin Freeman, David Cooke and Mat Watkins, for some very helpful discussions through the years. A special thank you to Flemming Ehlurs whose company and wit I have missed greatly since we moved away from Charlotte Street.

To my parents, a lardge thank you for providing such a loving home to grow up in and for supporting me in everything I do.

Finally, I would like to thank Olly for letting me be me and for his unswerving faith in me. I can't wait to be Mrs Dr Fenwick!

Contents

Chapter 1

Introduction

Calcite is an abundant biological mineral found in many places. All rock types contain at least traces of calcite, bones and teeth contain calcite and many living organisms use calcite as part of their structure [1]. In particular many sea creatures incorporate calcite structures in their anatomy, which in turn leads to the creation of biogenic sedimentary rocks that are formed through the deposition of dead aquatic organisms. Limestone and chalk are both sedimentary rocks composed of calcite. Evidence of preserved sea organisms is often visible in the rock, as illustrated in the chalk rock in Figure 1.1.

Calcite materials are used heavily in construction and in many other areas. 'Burnt lime' (created when limestone is heated to its decomposition temperature) is used by the paper industry to make paper bright. Chalk has been used for centuries as a writing material and the ancient Egyptians used limestone slabs for writing on, recording everything from funeral ceremonies to shopping lists.

While a lot of calcite is made by living organisms through biomineralisation processes, they are not essential to its formation. In many wet environments calcite particles precipitate out of water to form a crystal. The build up of limescale on domestic taps and drains is a prime example of this process. Precipitation from water also produces stalactites and stalagmites in caves and similar, undesired, structures in man-made concrete tunnels and air-conditioning units [2]. The opposite process, i.e. the dissolution of calcite by water, can lead to a 'karst' landscape, in which the shape of the land is determined by tunnels and caves created in the limestone

Figure 1.1: Picture of a chalk rock, taken from a beach near Copenhagen, containing fossilised sea organisms.

bedrock [3].

As previously mentioned, sea creatures often incorporate calcite structures in their anatomy. These organisms use organic molecules to control crystal growth and morphology, but detailed understanding of the biomineralisation process is lacking.

One very common type of simple organism, known as coccolithophores produce surprisingly complex materials called coccoliths through biomineralisation, some of which are shown in Figure 1.2. Coccoliths grow in two different ways, either organic material holds together the calcite crystals or the calcite crystals interlock through a mechanical fitting system. In the later case nucleation is believed to occur on an organic template, which controls the overall shape of the developing coccolith.

As biomineralisation generally occurs in an aqueous environment, the adsorption of organic molecules onto the crystal surface involves the displacement of water. Thus water adsorption and desorption on calcite surfaces is an important part of the biomineralisation process.

Understanding the biomineralisation processes that occur in nature could greatly improve human technology. Control of adsorption at the bio-inorganic interface would 'revolutionise' implant technology. Implants would be able to integrate com-

pletely into living tissue. The implant surface would be able to control molecular adsorption events. Experimental techniques are being developed to enable this kind of control [4], but modelling is needed to make full use of these techniques.

As the interaction between calcite and water is very common in nature, a full understanding of this system would be very useful. In order to obtain this knowledge it is necessary to ensure that, when looking at the interface on the atomic scale, theoretical predictions and experimental results agree about the behaviour of water at the surface. If the relationship between these two materials can be correctly predicted by theory, we can expand the simulated system to include more complex situations.

1.1 Experimental and Computational Models

A large amount of theoretical work has been performed on the calcite-water interface [6, 7, 8]. This modelling has largely been through classical molecular dynamics (MD) simulations, modelling water in its associated form on the calcite $\{10\bar{1}4\}$ surface, the most stable surface [8, 9]. However, some ab-initio calculations have been performed by Kerisit et al [9]. The $\{10\bar{1}4\}$ plane contains both Ca and CO_3 ions, making it charge neutral, and has a higher density of ions than other possible neutral planes, leading to its low surface energy and stable surface. One question that remains unresolved is that of whether water dissociates on the calcite surface. Water is known to dissociate on some oxide surfaces, but the question of whether water adsorbs in molecular form or dissociates to H^+ and OH^- on carbonate surfaces, such as calcite, has yet to be resolved.

Experimental work on the calcite-water interface provides strong evidence in favour of water dissociation on the calcite $\{10\bar{1}4\}$ surface [10]. Particularly strong evidence comes from XPS data, which shows both CaOH and HCO_3 on the surface [11]. Time-of-flight ion mass spectrometry (TOF-SIMS) and atomic force microscopy (AFM) experiments support the conclusion that water dissociates on this surface [12]. Fourier Transform Infrared Spectroscopy (FTIR) experiments showed evidence of peaks in the FTIR spectrum, indicating that hydroxyl species were present on the surface in bulk water [13]. However, previous ab-initio calculations [9] investigated

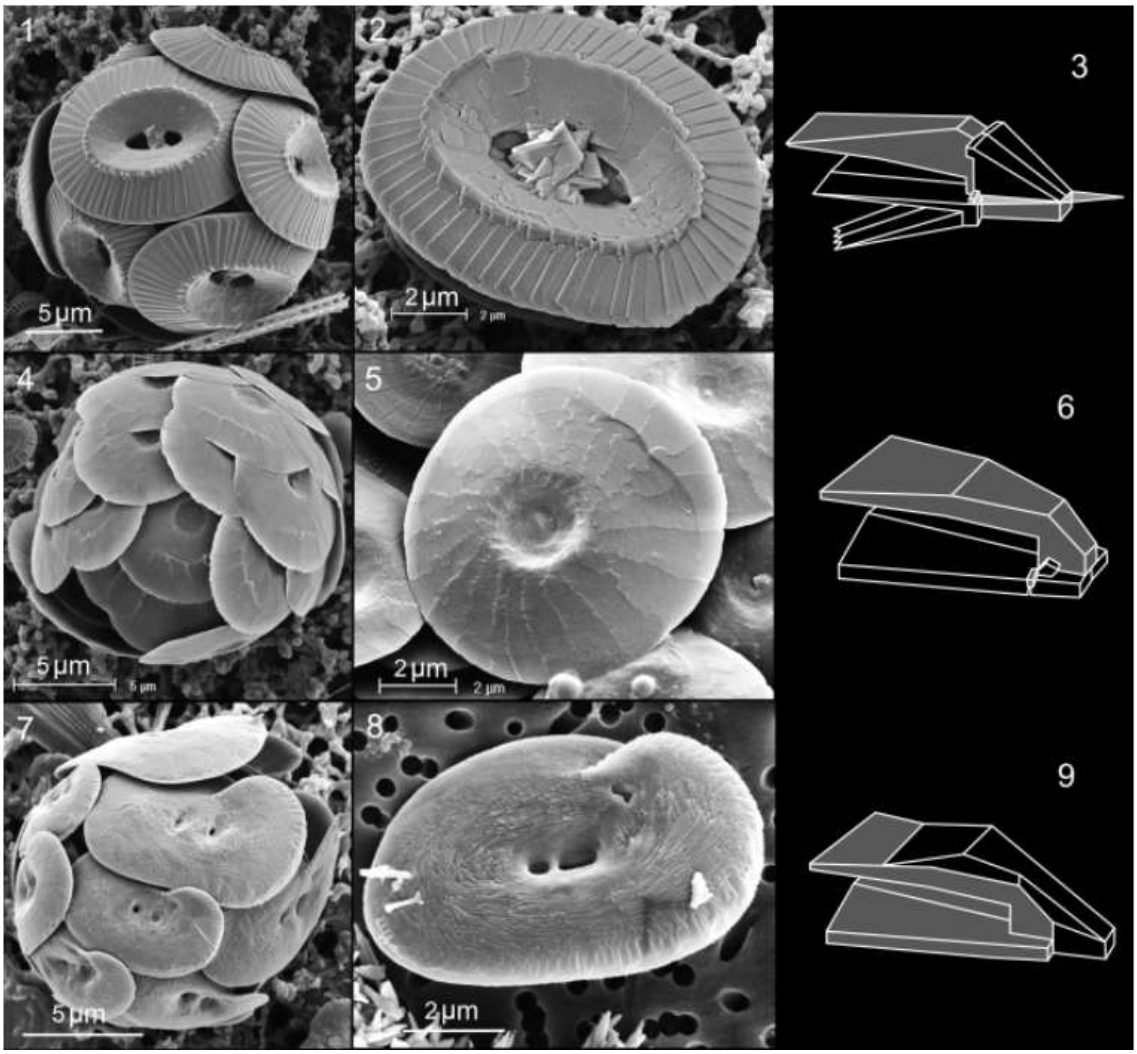

Figure 1.2: SEM images of coccoliths, along with diagrams of their building blocks. Images 1-3: *Coccolithus pelagicus*. Images 4-6: *Oolithotus fragilis*. Images 7-9: *Helicosphera carteri* [5]

a water configuration where one dissociated H_2O was initially placed above each Ca ion on the calcite $\{10\bar{1}4\}$ surface. The dissociated H_2O molecules spontaneously re-associated on the surface during static relaxation calculations, implying that the dissociated state is unstable. Along with a more general investigation of the calcite-water interface, this thesis aims to address the question of dissociation. The results of a comprehensive series of ab-initio static relaxations and MD simulations that aim to calculate the strength of the calcite-water interaction are reported.

1.2 Modelling of the Biological Interface with Materials Consortium

The work presented in this thesis has been undertaken as part of a consortium (the *Modelling of the Biological Interface with Materials Consortium*) investigating the bio-mineral interface. The consortium is formed from groups at four UK universities; the University of Cambridge, the University of Sheffield, the University of Warwick and University College London. The work of this consortium has focused on the development of methods for modelling organic-inorganic interfaces in order to understand processes such as biomineralisation and self-assembly of complex nanostructures. One aspect of this work is to derive a standard method for the development of new forcefields for classical simulations and to develop long-time scale and coarse grained methodology to describe the interactions that occur at these interfaces. Organic-water interfaces are currently well described by available models, as are some inorganic-water interfaces. However, while there are currently reliable potentials for minerals and for organic materials, we do not have reliable models for describing the interactions between the two types of material. The usual combination rules do not work well at this interface, leading to high binding energies. Combination rules for specific cases have been developed, but there is no protocol for producing reliable forcefields. The consortium members based at Sheffield have developed such a protocol, which will be described in Section 3.3 and is available in ref. [14].

When developing a potential it is almost always essential to use some experimental data to fit to. However, for many of the interaction cases we would wish to model,

there are no experimental data available, making it difficult to produce good interaction potentials [15]. One of the key interactions the consortium would like to model is that of the calcite-water interface. The work presented in this thesis is to be used to validate the new potential developed using the 'Sheffield protocol'. Ab-initio calculations (both static relaxations and MD) have been performed, the results of which can be compared with those of previous potentials and the consortium potential. As ab-initio calculations do not require any experimental data to fit to, they can be viewed as more reliable than the classical models. Thus, they will hopefully act as a useful comparison for developed potentials when there is no experimental data available for comparison.

1.3 Water dissociation on oxide surfaces

While the question of whether water dissociates on calcite remains unresolved, water dissociation has been observed both theoretically and experimentally on other mineral surfaces. However, the consensus on water behaviour on these surfaces was not reached without a degree of controversy along the way. In this section the contentions surrounding water dissociation on the oxide surfaces MgO (100) and TiO_2 (110) will be discussed.

1.3.1 MgO (100)

The presence of hydroxyl groups on the (100) surface of MgO had been detected through photoemission spectroscopy [16]. The spectra gave clear indications that water added to the surface during experiments dissociated. The amount of dissociation observed depended upon the conditions under which the experiment was prepared. Under some conditions a full monolayer of water was found to dissociate. Conversely, early theoretical, ab-initio, studies of isolated water molecules on MgO found that dissociation was unfavourable, although ab-initio MD simulations showed that dissociation did occur at steps [17, 18].

However, two studies by Giordano et al and Odelius, published in 1998, found that a 'mixed state' of both associated and dissociated water was the most stable

arrangement for water on the MgO (100) surface [19, 20]. Both studies found through ab-initio simulations that it was the interaction between the water molecules that caused them to dissociate, as isolated water molecules adsorbed associatively, supporting the previous work's conclusions.

The study by Giordano et al found, through a geometric optimization calculation, that in a monolayer of water one third of the molecules spontaneously dissociate upon relaxation and that the hydrogens transferred to the MgO surface where they formed surface OH groups [19]. The Odelius study used MD simulations, along with static relaxations, to investigate the dissociation. It was found that while a mixed state was favoured at coverages as low as half a monolayer in the static relaxations, the water molecules did not dissociate during a 1.2ps simulation at 200K, indicating a reasonably high barrier to dissociation at this temperature and coverage. However, the addition of one more water molecule to the simulation cell resulted in dissociation of a water molecule within 0.7ps at 160K. It was found that the ratio of associated and dissociated water molecules is determined by coverage, and that at monolayer coverage it is 2:1, in agreement with the findings of Giordano et al.

This conclusion was further supported by a study by Kim et al who compared density of states data from UPS (ultraviolet photoelectron spectroscopy) and MIES (metastable impact electron spectroscopy) spectra against the calculated density of states found when considering an adsorbed monolayer of water with a third of water molecules dissociated. The agreement was very good, providing strong evidence for the dissociation of a third of the molecules upon adsorption [21].

1.3.2 TiO_2 (110)

Whether or not water dissociated on the (110) surface of TiO_2 was the subject of investigation for some time. It had been predicted theoretically, but was not seen experimentally at low temperatures.

Ab-inito static relaxations that compared the adsorption energy of water in an associated form, with the adsorption energy of dissociated water were performed [22]. Two dissociated configurations were trialed at monolayer coverage, both of which were found to be more energetically favourable than the associated state.

The two states were described as a 'symmetrical' and an 'unsymmetrical' state. In the symmetrical state all the hydrogens pointed directly upwards, at 90^o angle to the surface. In the unsymmetrical state the hydrogens attached to a surface oxygen were allowed to bend towards the OH^- and the hydrogen of the hydroxyl group pointed away from this lone hydrogen. Of the two dissociated states, the 'unsymmetrical' dissociated state was more stable than the 'symmetrical' state. The calculations also predicted an increase in the adsorption energy as water coverage decreased, which can be attributed to the repulsion between hydroxyl groups.

However, experimental results did not support this theory entirely. A synchrotron radiation study of the TiO_2 (110) surface discovered that when they investigated the surface in contact with water at room temperature, evidence for hydroxyl species on the surface was found [23]. Conversely, when they conducted the same experiment at 160K there was no evidence of hydroxyl species and the data indicated that water adsorbed in a molecular form.

Experimental results such as these led to further theoretical investigation. A new study explored water dissociation further through ab-initio MD simulations [24]. When an additional water molecule was added into a 50% water coverage simulation, in which the water was dissociated at 250K, the new water molecule did not dissociate. Instead the new molecule arranged itself so that it formed a hydrogen bond with a nearby OH. This study also investigated three possible water scenarios using static relaxations. The scenarios were: (i) one dissociated and one associated water molecule (a 'mixed state'), (ii) two dissociated water molecules, (iii) two associated water molecules. These calculations supported the MD simulations in that they found the 'mixed state' was the most stable. However, the adsorption energy difference between this state and the others was only 0.19eV for state (ii) and 0.11eV for state (iii), which the authors felt would lead to the proportion of dissociated water observed changing with temperature, as seen in experiments.

Further explanation of this contradiction was offered by Lindan and Zhang in their ab-initio static relaxations, which also showed dissociation was the most stable configuration for water on the TiO_2 surface [25]. The calculations revealed that the amount to which dissociation is favoured increases with decreasing coverage. Their results also confirm that a 'mixed' state is more energetically favourable than two dissociated water molecules or two associated water molecules at one monolayer

of water coverage. However, this indicates that there are some dissociated water molecules at all coverages, and these would be expected to be seen in the experimental data. A possible explanation for their absence was uncovered by this theoretical study. It was found that the energy barrier to dissociation was high, and increased as the coverage decreased. This was a significant finding as in experiments the surface was dosed with water at ∼100K. The theoretical results would therefore lead to the prediction that at this temperature the water would remain in associated form, as the energy barrier would allow very little dissociation to occur, even over a period of several hours.

1.4 Thesis overview

In this thesis theoretical calculations on the calcite-water interface are presented. Chapter 2 will introduce previous work performed at this interface. Both theoretical and experimental work will be presented to give an overview of the field and to introduce the debate surrounding whether water dissociates on the $\{10\bar{1}4\}$ surface. Chapter 3 will introduce the computational methods used in the work presented here to explore the interface. Both density functional theory (DFT) and classical potentials will be discussed in this section.

The results of the calculations will be presented in Chapters 4, 5 and 6. In Chapter 4 ab-initio static relaxations performed in VASP will be discussed. Different levels of water coverage on the perfect $\{10\bar{1}4\}$ calcite surface were explored as well as associated and dissociated water states.

In Chapter 5, ab-initio molecular dynamics (MD) simulations of water on this surface will be discussed. A range of percentage water coverages were investigated with the MD simulations allowing more configuration space to be explored.

Chapter 6 will introduce both static relaxations and MD simulations performed on imperfect calcite surfaces. Vacancies of Ca and CO_3 ions in the $\{10\bar{1}4\}$ surface were explored as well as acute and obtuse steps. The behaviour of water at these defects was observed with the aim of predicting how water will behave on real calcite surfaces.

Finally, Chapter 7 will summarise the findings of this thesis and draw conclusions about how we can expect water on calcite surfaces to behave based on the results presented in this thesis.

Chapter 2

Calcite Structure and Water Interaction

This chapter reviews our current understanding of calcite and its interaction with water. As discussed in the Introduction (Chapter 1), calcite is an abundant mineral that is commonly found in aqueous environments. Experimental and theoretical investigation of the calcite-water interface is therefore important if we are to gain an understanding of processes such as biomineralisation. In this Chapter, the structure of the calcite crystal is discussed before experimental data and previous modelling studies of the interface are examined. Studies with water on the perfect $\{10\bar{1}4\}$ surface are reviewed, followed by studies investigating stepped calcite surfaces. The evidence surrounding the question of whether water dissociates on the calcite surface is then discussed, before a brief consideration of dissolution and growth processes is undertaken.

2.1 Calcite Crystal Structure

Calcite is one of three polymorphs of calcium carbonate that occur in nature; the other two being aragonite and vaterite. Calcite is by far the most abundant of these polymorphs. It is stable at atmospheric pressure and temperature and only decomposes at 700^0C, becoming calcium oxide [13]. Aragonite is the most stable

polymorph in high pressure environments, although it is possible for aragonite to form at atmospheric pressure in certain conditions, such as hot springs [26]. Vaterite is a metastable form of calcium carbonate, and either changes to form another polymorph, or is stabilised by water adsorption on its surfaces [6]. The differences between the three polymorphs originate from the different arrangement of the CO_3 ions in their crystal structures [13]. A calcium carbonate hexahydrate also exists, known as ikaite. This form of calcium carbonate forms at low temperatures, between -1.6 and 3^0C, in the presence of phosphate groups (both of these conditions inhibit the growth of calcite or aragonite). Ikaite is stable up to 25^0C at high pressures, but in atmospheric pressure and room temperature it is unstable and the crystal rearranges to form vaterite [8].

Calcite is a very abundant mineral and is often used by sea creatures for constructing their structures. However, due to its orthorhombic structure, aragonite is favoured by some marine organisms over calcite (as it has a rhombohedral unit cell). Aragonite favours the formation of long, thin crystals that form a strong elastic material when packed together [10]. However, calcite is the more stable phase and is favoured by many marine organisms. The shape calcite crystals take depends on many conditions such as the temperature, pressure and solution composition at formation.

The rhombohedral crystal structure of calcite was determined using X-ray diffraction by Bragg in 1914. The structure can be pictured through a comparison with the face-centred cubic sodium chloride structure, shown in Figure 2.1(a). To accommodate the carbonate ions of calcite this cell needs to be distorted by compressing the cube diagonal by 77%, the sodium ions are replaced with calcium ions and the chlorine ions are replaced with carbonate groups [1]. The rhombohedral calcite unit cell is shown in Figure 2.1(b).

Any crystal with a rhombohedral crystal structure can be defined using hexagonal axes and calcite surface planes are usually refered to using hexagonal indices[1]. The hexagonal unit cell has carbonate ions lying flat on the basal plane and has $a = b =$ 4.990Å and $c = 17.061$Å $\alpha = \beta = 90^o$ and $\gamma = 120^o$ [28]. The hexagonal unit cell is pictured in Figure 2.2.

[1]While it is possible to refer to crystal planes in hexagonal crystals with three Miller indices, it is more usual to use four, and this convention will be followed in this thesis. The first three indices refer to the basal plane of the cell and the fourth describes the intercept on the c-axis [27].

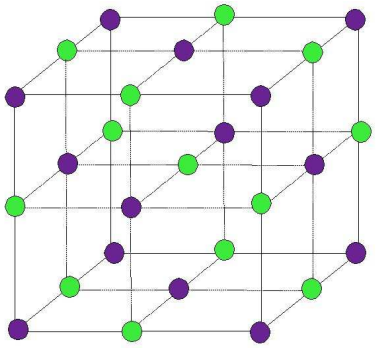

(a)

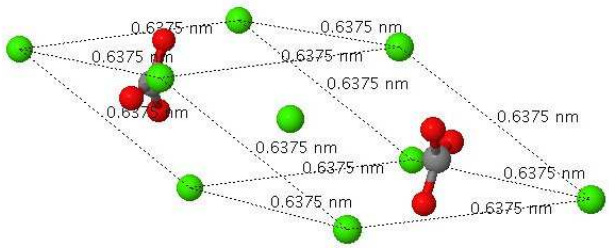

(b)

Figure 2.1: (a) Sodium chloride lattice. Na ions are purple, Cl are green. (b) Calcite rhombohedral unit cell. Ca ions are green, C are grey and O are red.

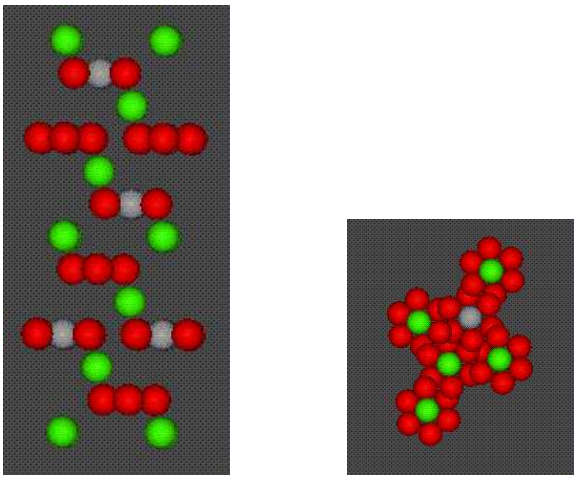

(a) (b)

Figure 2.2: Calcite hexagonal lattice (a) side view (b) top view.

The calcite surface unit cell is rectangular, containing two calcium and two carbonate ions. The surface cell is illustrated in Figure 2.3. The dimensions of the surface cell, found from experiment, are $\mathbf{a}_1 = 8.097$Å along $\mathbf{x}$ and $\mathbf{a}_2 = 4.991$Å along $\mathbf{y}$. $\mathbf{a}_3$ is the vector that relates the surface to neighbouring layers and is given by $\mathbf{a}_3 =$ -3.077$\mathbf{x}$ -2.4964$\mathbf{y}$ +3.036$\mathbf{z}$. These parameters give a surface unit area of 40.41Å^2 and layer spacing in the direction normal to the surface of 3.036Å. The shape and size of the surface cell have been observed in a number of experiments including X-ray scattering and AFM imaging [29, 30].

The calcium and carbonate ions in calcite are held together through ionic bonding. It is therefore relatively easy to cleave the crystal, as an external force can cause a plane of atoms to shift into a position where ions with the same charge are next to each other, causing repulsion and cleavage [1]. There are many possible cleavage planes, but the lowest energy surface is the $\{10\bar{1}4\}$ surface [6, 9, 8, 31], illustrated in Figure 2.4.

Cleavage along the $\{10\bar{1}4\}$ plane gives rise to the characteristic rhombohedral shape of calcite crystals, displayed in Figure 2.5. The plane contains both Ca and CO_3 ions, making it charge neutral. It also has a higher density of ions compared to other possible neutral planes, leading to its stable surface and low surface energy. Two other surfaces are shown in Figure 2.4, the $\{01\bar{1}2\}$ and the $\{00\bar{0}1\}$ surfaces. These

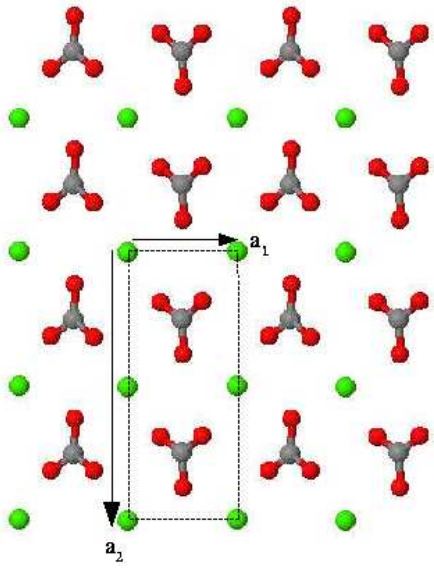

Figure 2.3: The calcite surface unit cell. $|\ \mathbf{a}_1\ | = 8.097$Å and $|\ \mathbf{a}_2\ | = 4.991$Å.

planes are polar as they are terminated by either a layer of calcium ions or a layer of carbonate ions, leading to a positively or negatively charged surface respectively. Polar surfaces are unstable by themselves and will either reconstruct to neutralise the dipole moment or adsorb ions to remove the dipole moment. However, they can be stabilised when grown on charged substrates. The work presented in this thesis focused on investigation of the low energy $\{10\bar{1}4\}$ surface.

2.2 The Calcite-Water Interface

The calcite-water interface has been widely studied with many techniques and under many different conditions. The high interest in this interface comes from the importance of calcite in our lives and its common occurrence in aqueous environments. Both growth and dissolution occur in water, and if we are to understand these processes we must first have a thorough understanding of the standard behaviour of water on calcite. Investigation of the calcite-water interface has been undertaken with a large number of experimental techniques. Results from a variety of techniques will be discussed in the following sections, including X-ray photoelectron spectroscopy (XPS), time-of-flight secondary ion mass spectrometry (TOF-SIMS),

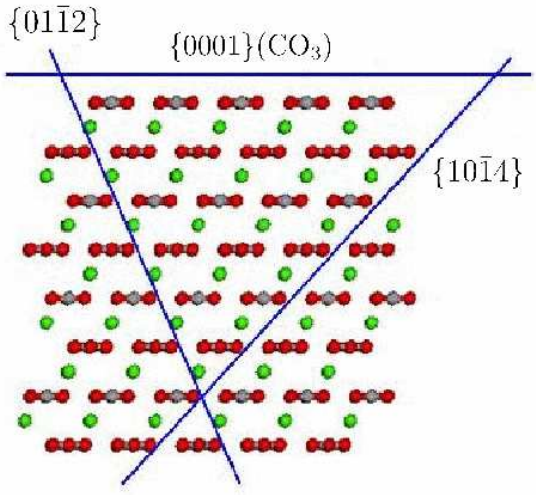

Figure 2.4: Illustration of the {01$\bar{1}$2}, {0001} and {10$\bar{1}$4} surfaces of calcite. The {01$\bar{1}$2} and {0001} surfaces are charged, while the {10$\bar{1}$4} surface is charge neutral.

Figure 2.5: Photograph of a calcite crystal, displaying its characteristic rhombohedral shape. [32]

low energy electron diffraction (LEED), atomic force microscopy (AFM), fourier transform infrared spectroscopy (FTIR) and X-ray scattering.

A large amount of theoretical modelling has also been performed. The eventual aim of this kind of modelling work is to be able to predict the behaviour of systems that are difficult to replicate in the laboratory and awkward or dangerous to experiment on in situ. For example, many calcite systems only exist at high temperatures and pressures in the earth's crust [10]. Properties of the calcite-water interface, such as the arrangement of water molecules on the surface, as well as surface and adsorption energies have been investigated using atomistic simulation techniques [6, 9, 33, 34, 7]. While the majority of the work done on the calcite-water interface has used classical methods, some work using electronic structure methods has been performed. Notably Kerisit et al. in their construction of the surface phase diagram of the calcite surface in contact with a gaseous phase of water and carbon dioxide [35]. This theoretical work will be discussed along with the experiments in the following sections.

The first section will focus on modelling that has investigated the surface energy of the numerous possible surface planes. This will be followed by a discussion of the calcite-water interface on both perfect $\{10\bar{1}4\}$ surfaces and on stepped surfaces. The experimental evidence in favour of water dissociation on the surface will then be discussed, along with previous theoretical modelling results that contradict the conclusion that water dissociates. Finally calcite dissolution and growth processes will be considered.

Before discussing the experiments it is worth noting that while calcite is an abundant mineral in the environment, obtaining pure calcite for use in experiments can be difficult. A large amount of the work discussed in the following section was carried out by S.L.S. Stipp. from the University of Copenhagen, who used crystals of natural Iceland spar calcite from Chihuahua in Mexico in experiments. This type of calcite is more than 99% pure [10]. Some of the other work used synthesised calcite and the method of synthesis is briefly described before the results from the experiments are presented.

2.2.1 Surface energy

As discussed in section 2.1, there are many possible calcite surfaces, depending on how the crystal is cleaved. A theoretical study investigating the surface energy of some of these planes was conducted by de Leeuw and Parker [6]. Their study showed, using classical static relaxations, that the $\{10\bar{1}4\}$ surface had the lowest energy at 0.59Jm^{-2}, compared with the next lowest, the $\{0001\}$Ca surface (a plane terminated with a layer of Ca ions) at 0.97Jm^{-2}. Electronic structure relaxations obtained an energy of 0.43Jm^{-2} for the $\{10\bar{1}4\}$ surface [9], lower than that found using classical techniques. In all theoretical calculations, the $\{10\bar{1}4\}$ surface is consistently found to have the lowest surface energy [8, 31].

Another study, also using classical static relaxations, which included stepped surfaces found that the stepped $\{10\bar{1}3\}$ and $\{10\bar{1}5\}$ surfaces (which contain $\{10\bar{1}4\}$ planes offset by steps) had lower surface energies than the $\{0001\}$Ca surface [8], although these surfaces had to be altered slightly to remove the dipole on the step as each one consists of only either Ca or CO_3 ions. In the calculations, the dipole was removed by taking half the Ca ions, or half the CO_3 ions, from the step edge and moving them to the bottom of the unit cell. This created a step edge with 50% vacancies. While de Leeuw and Parker note there is no experimental evidence for this 'crenellated' step structure, they tentatively suggest the surface does restructure itself in this way and it is this arrangement that gives rise to the 'tongues' of calcite growth observed moving outwards from steps in experiments [36].

2.2.2 Hydrated surfaces

Calcite is often found in aqueous environments and it is therefore important to try and understand the hydrated calcite surface. Low energy electron diffraction (LEED)[2] patterns can be used to determine atomic order in the top-most layers in a solid and have been used to establish that there is little restructuring at the surface when it is hydrated [11]. The pattern produced provides evidence of a surface cell pattern measuring 5.0×8.1Å. Weaker reflections in the pattern indicate a 2×1

[2]To form a LEED pattern, a beam of low-energy electrons is shone on a sample normal to the surface. If the upper layers are ordered then electrons, which are elasticaly backscattered, form a diffraction pattern on a fluorescent screen above the sample.

relaxation, meaning the surface unit cell doubles along the **a** direction to 10.0Å [12]. However, a more recent theoretical study predicts a 2×1 superstructure on stepped calcite surfaces, indicating this could be a structural property rather than an effect of the reactive species at the surface [37].

Time-of-flight secondary ion mass spectroscopy (TOF-SIMS)[3] data reveals information about the composition of the top one or two layers of a solid, although only charged particles can be detected. The data provided by TOF-SIMS analysis of the calcite surface, cleaved in and exposed to air for approximately 10 minutes before analysis, showed high levels of O and H being ejected from the surface, particularly at step edges, providing evidence of water adsorption across the surface [12]. The brightness in the maps at the steps is more likely to be due to them being at a more preferential angle to the detector, rather than due to a greater density of water at step edges [10].

The surface charge has been investigated with electrokinetic experiments. These established which ions control the surface charge of calcite in aqueous conditions and found that it is controlled by the Ca^{2+} and ${CO_3}^{2-}$ surface ions. The study also ruled out the possibility that the surface electrical properties were influenced by H^+, $CaOH^+$, ${CaHCO_3}^{2+}$ and ${HCO_3}^{2-}$ species on the surface [38].

A theoretical study using classical static relaxations investigated different hydration levels on several calcite surfaces and found that as the water coverage increased the surface energy decreased [8]. A full monolayer of water was considered in a study using electronic structure relaxations, which found a hydrated surface energy of $0.04 \mathrm{Jm}^{-2}$, significantly lower than a dry surface ($0.43 \mathrm{Jm}^{-2}$). The water adsorption energy was found to be -92.3kJmol^{-1} (found by comparing the energy of the pure surface and an isolated water molecule with the energy of the hydrated surface). The Ca-O_{water} distance was 2.38Å after relaxation [9]. The same Ca-O_{water} distance was found when a monolayer of water was investigated with classical relaxations. The pattern of water formed on the surface after energy minimization can be seen in Figure 2.6. The H_2O molecules in the monolayer lay flat on the surface with each surface CO_3 ion coordinated to two hydrogen ions from different H_2O. The bond length varied, being 1.87Å for one H-$O_{surface}$ bond and 1.97Å for the other [6].

[3]TOF-SIMS determines, from the time taken to fly from a sample to the detector, the mass of ejected or secondary ions.

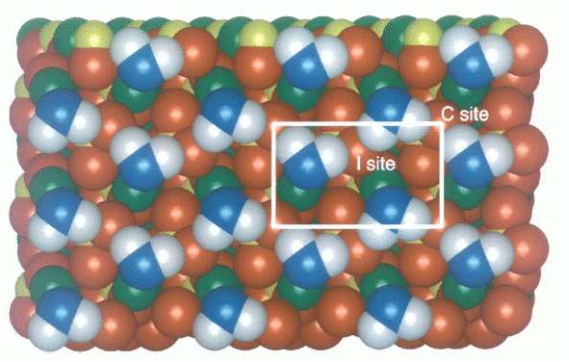

Figure 2.6: Plan view showing the adsorption pattern of water on the $\{10\bar{1}4\}$ surface. (O=red, Ca=green, C=yellow, O_{water} =blue, H=white.) [8]

A separate study, which also used classical simulations, took this structure as the starting configuration for static relaxations. A different potential was used to that of the previous study and it found a Ca-O_{water} distance of 2.55Å [39].

The calcite interface with bulk water has also been the subject of investigation. A classical molecular dynamics (MD) study simulating bulk water on a $\{10\bar{1}4\}$ surface at 300K suggested that the first two layers of water at the surface are structured [33]. In the first layer, 2.2Å above the surface, the molecules lie flat on the surface with the oxygen coordinated with a surface calcium. In the second layer, 3.2Å above the surface, the molecules are perpendicular to the surface with a hydrogen atom coordinated with a surface oxygen. The water density profile can be seen in Figure 2.7.

The existence of this arrangement is supported by experimental X-ray scattering data that found two inequivalent water molecule layers at the calcite surface in bulk water [29]. This technique is particularly useful for this type of investigation as X-rays can penetrate liquids with limited attenuation, allowing information about the underlying crystal to be gathered as well as the liquid layer [40]. Further investigation showed that the experimental X-ray data obtained could not be explained by an ideally terminated calcite surface with no ordering of the water near the surface [29]. A structural model was developed that was consistent with the data. The model shows a hydration layer at the surface consisting of two H_2O molecules per surface Ca ion sitting at 2.3 ± 0.1 Å and 3.45 ± 0.2 Å above the surface. The surface restructuring detected the Ca and CO_3 ions move 0.017 ± 0.004 towards and 0.12 ± 0.01 Å away from the bulk crystal respectively. The tilt of the carbonate groups in relation

to the surface was also noted to have changed upon hydration. However, the LEED experiments showed there was little restructuring upon hydration [11], so these effects can be assumed to be relatively small.

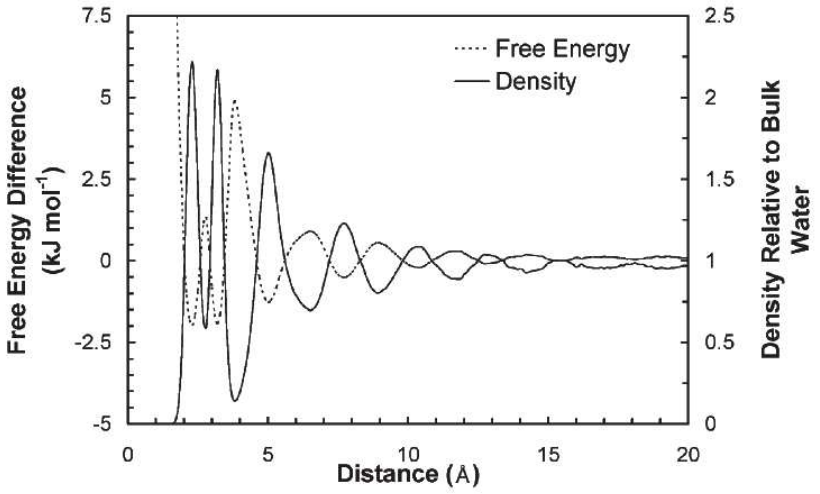

Figure 2.7: Water density and free energy profiles of water on the $\{10\bar{1}4\}$ surface as a function of distance. [7]

A more detailed analysis of further layers in the classical modelling suggests there is still order in the third layer of water [34], although this is not seen in experimental data. In the third layer the water molecules are starting to interact strongly with each other through hydrogen bonds, meaning the influence of the surface is weakened. An orientation order parameter was introduced, which showed that in the first layer water molecules within 2Å of the surface lie almost flat on the surface [34]. The order parameter also revealed that the water molecules rotate as they move away from the surface to make hydrogen bonds with neighbouring H_2O molecules, before they reorientate to be almost parallel to the surface again upon entering the second layer.

Classical MD simulations also revealed that the water density is highest at the surface. This high density affects the next layer by reducing its density in comparison to bulk water. In this way the surface causes an oscillation in water density [9].

The diffusion of water both parallel and perpendicular to the surface has also been considered in theoretical studies. It was found that as the water comes closer to the surface the diffusion coefficient decreases both in respect to diffusion between layers

and across the surface. This analysis also showed that the diffusion constant was correlated with the water layering, in that in areas with a low water density, there was a high diffusion coefficient [34]. The residence time of water in each layer was calculated using atomistic MD simulations. It was found that the residence time increased as the water molecule approached the surface. When the water molecule was in the first layer, it had a residence time of 300ps, compared with 8.8ps when it was in the fourth layer [33].

The water structure is clearly affected by the presence of the surface. Calculation of the oxygen-oxygen radial distribution function (RDF) of water in each layer in a theoretical simulation provides further evidence of this influence[4]. In the first water layer there was a peak at around 4.1Å, corresponding to the Ca-Ca distance in the calcite surface, indicating that the surface structure is dominating the water separation, not hydrogen bonding between molecules. In the second layer the interaction with the surface still exists, but is not strong enough to completely break the hydrogen bonding network of the water [34].

2.2.3 Steps and kinks

While a large number of theoretical studies have focused on the perfect $\{10\bar{1}4\}$ surface, in real calcite crystals (and experimental systems) stepped surfaces would be present. This section looks briefly at the different steps that occur on the surface and goes on to discuss theoretical work investigating how steps interact with water along with the influence of kinks in surface energy and water interaction.

There are two types of steps possible on the $\{10\bar{1}4\}$ surface, the acute and obtuse steps, both are illustrated in Figure 2.8. There are many surfaces that include these steps, but the surfaces on which the steps are closest together are the $\{31\bar{4}8\}$ and $\{3\,\bar{1}\,\bar{2}\,16\}$ surfaces, describing a plane with acute and obtuse steps respectively.

On the acute $\{31\bar{4}8\}$ surface the carbonate groups on the step edge overhang the plane below, forming an angle of 80^o with the lower surface. The surface consists of $\{10\bar{1}4\}$ planes and a monatomic step, which is also a $\{10\bar{1}4\}$ plane. On the obtuse $\{3\,\bar{1}\,\bar{2}\,16\}$ the carbonate groups on the step edge lean backwards with respect to the

[4] An RDF describes the surrounding density as a function of the distance from a specified point.

plane below, forming an angle of 105^o with the lower plane. This plane also consists of $\{10\bar{1}4\}$ planes with a monatomic step of a $\{10\bar{1}4\}$ plane [9].

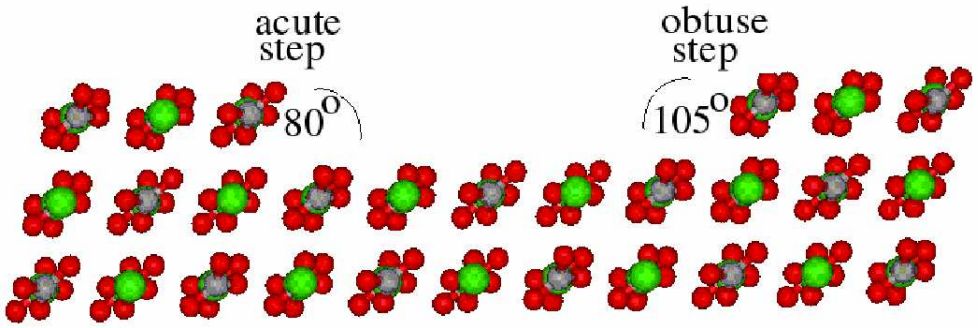

Figure 2.8: A slab of calcite showing an acute step on the left and an obtuse step on the right.

Classical calculations have been performed evaluating the energy cost of making a step on the $\{10\bar{1}4\}$ surface. These found that the obtuse step was energetically favourable compared to the acute step, and therefore we would expect to find more obtuse steps on real crystals [8, 37].

Calcite surfaces readily adsorb water from the atmosphere, therefore simulations must consider the surface in contact with water. A classical relaxation of a water molecule on the $\{10\bar{1}3\}$ surface (a stepped surface, with a crenellated step edge, consisting of $\{10\bar{1}4\}$ planes offset from each other by one layer down the $\{10\bar{1}1\}$ cleavage plane) found that the lowest energy site for a water molecule was with the O_{water} coordinated to an edge Ca ion at a distance of 2.47Å. One of the H atoms was directed towards the step, while the other pointed directly away. The adsorption energy of the water molecule was -1.16eV. The $\{10\bar{1}5\}$ surface (another surface containing crenellated step edges, consisting of $\{10\bar{1}4\}$ planes offset by one layer down the $\{0001\}$ surface) was also investigated using a classical relaxation and found to have an adsorption energy of 0.80eV. The water molecule was found to adsorb in two different ways - one in which the H_2O sat on top of the step and one in which the H_2O was coordinated with the step edge and the plane below. The Ca-O_{water} distances were 2.39Å and 2.52Å respectively [8].

Classical MD simulations with a monolayer of water on the $\{31\bar{4}8\}$ and $\{3\,\bar{1}\,\bar{2}\,16\}$

surfaces have been reported [41]. These found that, as on the flat surface, adding water reduced the surface energy, indicating the presence of water has a stabilising effect. Unlike the flat surface, the water was found to adsorb to the surface in an irregular pattern. Another classical MD simulation, in which significantly more water was studied on the stepped surface (a water layer of ∼18Å was used) found that when water was on stepped surfaces the presence of a step did not greatly affect the regular arrangement of H_2O molecules in the hydration layer that was in direct contact with the surface. However, it was found that the arrangement was disrupted in H_2O molecules right next to the step. At the acute step the second H_2O initially coordinated with a particular Ca ion delocalised between two possible adsorption sites, implying the H_2O was less strongly bound to the stepped surface than a flat surface. At the obtuse step, because the step created more room, two new adsorption sites appeared on the surface, making the water density much greater at the obtuse step than at the acute step [42].

It is possible to form a 'kink' on a step by either removing or adding some material. A classical study considered the energy cost of forming kinks by adding one $CaCO_3$ unit onto the step edge of the two steps. Adding a kink to the acute step was found to be ∼0.5eV more energetically favourable than forming one on an obtuse step [37]. The removal of a $CaCO_3$ unit from an obtuse step was found to need 0.16eV more energy compared with the acute step [9]. This would lead us to predict that the obtuse step would be the slowest dissolving in water, however experimentally it is seen to be the fastest dissolving [43].

It is also possible to form a kink by removing either a single calcium or single carbonate ion from a step edge. It is anticipated that in any real reaction a CO_3^{2-} ion would leave the step first. The cost of removing this ion from a hydrated step has been found from classical simulations to be 1.45eV from the acute step and 0.93eV from the obtuse step [9]. Classical simulations in which a kink was created in the $\{31\bar{4}8\}$ surface (acute steps) showed that when a calcium was removed an H_2O molecule was adsorbed in the vacancy created, although there was little affect on the overall water density. However, when a carbonate ion was removed, two new adsorption sites appeared. The overall water density was disrupted by the kink and a higher density was seen in the step area. When the same process was applied to the $\{3\,\bar{1}\,\bar{2}\,16\}$ surface (obtuse steps) there was much larger disruption to the water density when a Ca ion was removed. The angle of the step allowed two

new H_2O adsorption sites to appear, leading to a much higher water density at the step. When a CO_3 ion was removed the effect on the overall water density was very similar, although only one new adsorption site at the step appeared [42].

2.2.4 Dissociation

Whether or not water dissociates into H^+ and OH^- on the calcite surface has been the subject of some investigation, and is the main subject of this thesis. Experimental evidence suggests water does dissociate on the surface. However, existing theoretical evidence suggests this is not favourable on the $\{10\bar{1}4\}$ calcite surface. The experimental evidence supporting the hypothesis that water dissociates is discussed in the following section followed by a discussion of the theoretical evidence contradicting it.

Experimental studies

The main experimental evidence for the dissociation of water on calcite comes from an XPS study performed by Stipp et al [11]. A detailed XPS[5] study of more than sixty calcite samples, subjected to six different conditions was performed. The Ca_{2p}, C_{1s} and O_{1s} levels of the samples were analysed and all the samples fitted one of six categories, based on the inital conditions [11][6]. The Ca_{2p} data showed peaks relating to near-surface and surface Ca, which would be expected. The C_{1s} data revealed a peak in all cateogories, which varied in intensity depending on how the sample was prepared, corresponding to the energy of CO_3H. The peak was strongest on dissolving or precipitating surfaces and was least prevalent in samples that were fractured in vacuum, although it was still identifiable. The O_{1s} data showed peaks

[5]XPS is carried out in an ultra-high vacuum (UHV) and uses X-rays to eject electrons from the surface layers of a solid. Electrons from the core and valence levels of an atom can be ejected and it is possible to obtain information from the first several tens of angstroms. 95% of electrons ejected from calcite during XPS are from the top 90Å of the solid [44].

[6]The six cateogories of sample were: 1) Baked twice, fractured in vacuum and analysed within 26 minutes. 2) Baked twice, fractured in vacuum and analysed within 2 hours. 3) Baked twice, fractured in vacuum and analysed after 2 weeks in vacuum. 4) Cleaved in air and analysed immediately. 5) Cleaved in air, exposed to distilled water for 12 hours at 50^0C with N_2 bubbling - dissolution occurred. 6) Cleaved in air, immersed in solution initially saturated with 100% CO_2 and Iceland spar and left for 4 months - precipitation occurred.

relating to CaOH on the surface in samples that had been exposed to water, but was not seen on samples cleaved in vacuum. The intensity of this peak was highest in the sample where precipitation had occurred. A selection of these spectra are shown in figure 2.9.

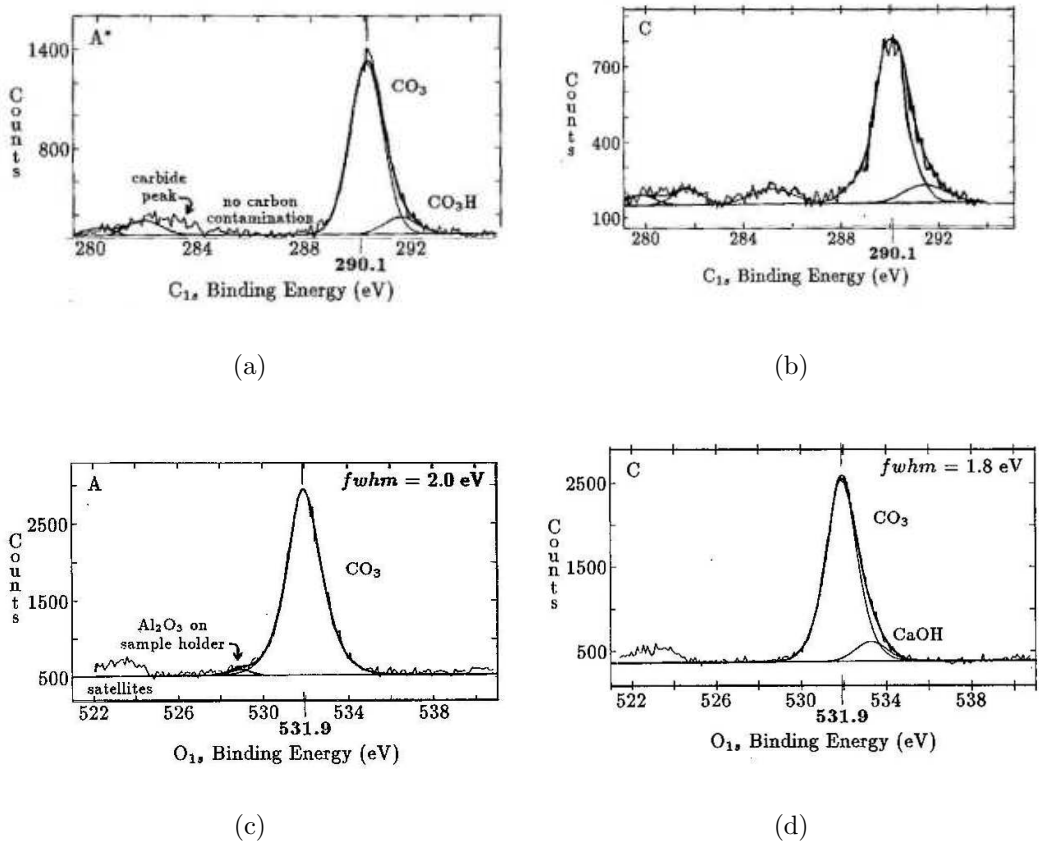

Figure 2.9: XPS data of the calcite surface prepared in different conditions. (a) C_{1s} spectra of sample baked and fractured in vacuum and analysed within 26 minutes. (b) C_{1s} spectra of sample cleaved in air and analysed immediately. (c) O_{1s} spectra of sample baked and fractured in vacuum and analysed within 26 minutes. (d) O_{1s} spectra of sample cleaved in air and analysed immediately. [11]

It is not possible to detect the presence H directly with XPS, however the atoms are small enough to pass through the chamber walls into the system and its presence, as H_2, during the experiments was confirmed. The XPS analysis leaves the calcite surface with a positive charge due to the ejection of electrons, and the H_2 interacts with this charge. It dissociates and the H is then free to join a CO_3 group forming CO_3H [11]. This may be the source of the of CO_3H evident in the spectra of surfaces

cleaved in vacuum.

At the energies where H_2O would be expected, no peak was observed, implying that it was not present in the spectra of calcite samples cleaved in air and then subject to XPS in vacuum. Stipp suggests that the layer of water in contact with the surface is dissociated and that any associated water has evaporated from the surface in the vacuum, as it is less strongly bound than the dissociated water [10].

Other experimental evidence that favours the conclusion that water dissociates include AFM images. These images, taken in 'contact' mode, of the calcite surface in solution found there appeared to be a slight 'pairing' between rows. Rows were expected to be evenly spaced, but appeared to pair-up, so that two rows were close together and then there was a significant gap before the next row [45]. In this pair one row is higher than the other. These effects are conserved when the sample is rotated and imaged at a different angle, indicating they are an effect of the surface and not an artefact of the tip shape or of the scanning.

Stipp has hypothesised that the higher rows are hydroxide ions sitting above a surface Ca ion, as these ions would sit considerably higher on the surface than the surface carbonate groups and would therefore be more likely to be imaged [12]. If OH ions were on the surface they would have considerable freedom of movement, and so are likely to be pushed away from their usual positions by the force of the approaching AFM tip. Stipp suggests that as the tip moves across the surface half of the OH groups are pushed away from their bonding direction and towards the surface. The other half are pushed towards the Ca atom, but are held back by repulsive forces. This would lead to the pairing and height alternation of rows seen in the AFM images. This idea is illustrated in Figure 2.10.

However, it is thought by some that even if OH^- exists on the surface it is simply pushed aside by the tip and not observed in the AFM image at all [30]. Liang et al tested whether the AFM images were influenced by hydroxyl species on the surface by imaging the surface at different pHs. In an acidic solution it would be expected that HCO_3^- is most abundant, but in a basic solution $CaOH^+$ would be more abundant. This would mean that as the pH changes the AFM images would change in accordance with the different surface species. However, no change was observed as the pH was altered and the group concluded that the AFM images are

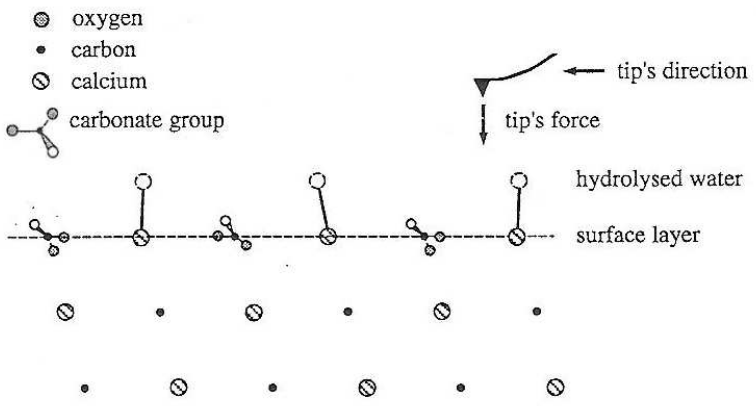

Figure 2.10: An illustration of a cross section of calcite with hydroxyl ions on the surface being imaged by an AFM tip [12].

derived from the calcite surface itself, and do not include the water adsorbed on the surface.

Another study by Kuriyavar et al used synthesised calcite crystals in an FTIR experiment [13]. Two different synthesis methods were used. The first method, carbonation, involved bubbling CO_2 gas through an 'aqueous slurry' of $Ca(OH)_2$ and produced samples containing both calcite and aragonite. The second method, in which crystals were grown from solution, allowed preparation of pure calcite and aragonite crystals. Temperature dependent FTIR studies of the samples showed that the sample created through carbonation had high levels of hydroxyls present both on the surface and inside the crystal. The 'interstitial' hydroxides were left over from the synthesis process when CO_2 was bubbled through the $Ca(OH)_2$ slurry. The surface $Ca(OH)_2$ seen on these samples is not present on those samples synthesised from solution. Neither the pure calcite or pure aragonite samples showed any hydroxyls present on the surface at 100, 200, 300 or 400^{o}C. It is therefore possible to suggest that the presence of hydroxyls was dependent upon how the $CaCO_3$ crystal was formed and whether the crystal was pure calcite or aragonite.

In summary, the main evidence for dissociated species on the calcite surface comes from XPS data in which CaOH are visible in the spectra of samples cleaved in air. Other experiments that have been interpreted as supporting the hypothesis that water dissociates are not necessarily capable of identifying precisely what is being detected by equipment. An FTIR study found OH present on impure calcite

crystals. However, it was not found on pure samples, presenting the possibility that dissociation is triggered by defects or impurities in the crystal structure.

Theoretical studies

A few theoretical studies have attempted to find a mechanism for water dissociation on the calcite surface. Classical simulations cannot directly test for dissociation, as they do not describe chemical reactions, however dissociation of water has been briefly studied with ab-initio techniques. An energy minimisation calculation was carried out in which a monolayer of water on the $\{10\bar{1}4\}$ surface was initially dissociatively adsorbed. A hydroxyl was placed above each Ca ion and the spare hydrogen atoms were placed above surface carbonate oxygens. Upon relaxation, the water ions recombined to form water molecules, indicating dissociation is not energetically favourable [35]. This study also included static relaxations of $\{10\bar{1}4\}$ surfaces in which carbonate groups were removed and replaced with two hydroxl ions, and in which calcium ions were removed and replaced with two hydrogen atoms. The calculations investigated the behaviour of water, at a number of coverages, on these imperfect surfaces. No dissociation was observed at any coverage.

As experimental evidence seems to indicate the presence of dissociated water on the surface further exploration is required. Classical static relaxations have been employed to give an indication of what might prompt water to dissociate. Several, imperfect calcite surfaces (including the $\{10\bar{1}4\}$, $\{10\bar{1}3\}$, $\{10\bar{1}5\}$, $\{3\,\bar{1}\,\bar{2}\,16\}$ and $\{31\bar{4}8\}$ surfaces) with hydroxyl ions were simulated to discover how water dissociation might occur at defects. CO_3^{2-} vacancies were created in each of the surfaces and were replaced by two hydroxyl ions, thus neutralising the charge. Surfaces with an acute step were the most reactive as the hydroxyls were able to form a large number of short bonds with the surface in this configuration, although on all the surfaces the hydroxyls adsorbed so that their O was coordinated to surrounding Ca ions [9]. When these systems were considered with full water coverage a similar structure of the hydroxyls adsorbing coordinated to Ca ions was observed, except on a couple of stepped surfaces. Perhaps a surprising result was that the surface energies did not reduce when the water was introduced, as it had on the un-defective surfaces (see previous Sections 2.2.1 and 2.2.3), but actually increased. Kerisit et al suggest this was due to the stable water pattern observed on the non-defective

surfaces being disrupted by the addition of the hydroxyls.

A classical modelling study performed a series of calculations in which dissociated water molecules were placed in a variety of positions on the $\{10\bar{1}4\}$ surface and allowed to relax [13]. The calculations showed that the formation of a bicarbonate and a hydroxide ion on the surface were exothermic, however the calculations did not consider an associated H_2O on the surface, so it not possible to compare the energies of an associated and dissociated configuration.

Theoretical evidence therefore points towards dissociation of water on the flat surface being energetically unfavourable. However, hydroxyls have been shown to adsorb at steps, implying these structures might be possible sites of dissociation. The work in this thesis will expand on the work previously carried out and explore possible sites of dissociation on the $\{10\bar{1}4\}$ calcite surface.

2.2.5 Dissolution processes

The dissolution of calcite has been the subject of a number of experimental and theoretical studies. An understanding of this process is particularly important in systems where calcite is an unwanted nuisance. A few of the results from both experiments and calculations are discussed here.

The rate of dissolution depends on a number of factors, these include the pH of the dissolving solution. Dissolution rates have been observed to be high in solutions with low pH. The solution pH gradually increases as dissolution occurs [30] leading to slower and slower dissolution.

AFM images, in 'contact' mode, of calcite surfaces in solution showed that on initial contact with water, small etch pits formed within seconds [45]. As the sample continued to be imaged the pits became broad and flat-bottomed. While the initial etch pits had straight sides and it was not possible to distinguish between step types, after a while a difference between the acute and obtuse steps became evident - the acute edges were straight, and met at well defined corners, while the obtuse edges were curved, suggesting they had a higher kink density. AFM images of this process are shown in Figure 2.11.

This process of dissolution, by the creation of pits and retreat of steps, was also observed by another group during AFM imaging [43]. Shallow pits were observed during the initial dissolution stage with a depth of ∼3 or ∼6 Å, the approximate depth of one or two layers of calcite. The pits were typically rhombohedral in shape and surrounded by straight step edges. Deeper pits occurred less frequently during the inital dissolution stage, but eventually came to dominate the surface. Observation of the deep pits clearly indicated the presence of two different types of steps. The two steps retreated at different velocities, with the obtuse step retreating 2.3 times faster than the acute step, at 3.4nm s^{-1} compared to 1.5 nm s^{-1}. The rate of dissolution over the whole surface will therefore be, at least partially, dependent upon the density of each kind of step.

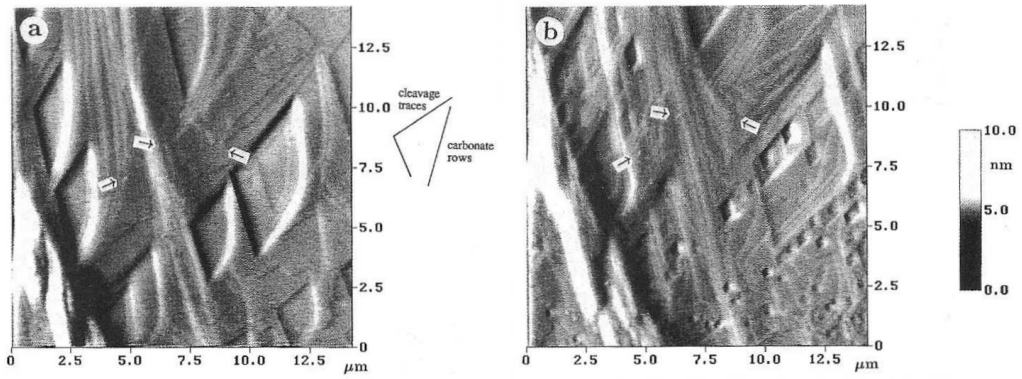

Figure 2.11: AFM images of a dissolving calcite surface. Acute steps are straight and obtuse steps are curved. (a) Surface after 15 minutes in solution. (b) Surface after 19 minutes in solution. [45]

To model dissolution the numerous dissolution pathways must be explored. If we first consider the removal of an ion from the flat surface, it is likely that we would expect to have to overcome a large energy barrier and this has been found to be the case. Classical MD simulations were used to study the removal of a Ca ion from the $\{10\bar{1}4\}$ surface into water. The Ca ion was removed from the surface and a series of MD simulations were performed in which the Ca ions was constrained at different heights above the surface, giving the free energy of dissolution of the Ca ion. The removal of a Ca ion required ∼275 kJmol^{-1} of energy. A similar procedure was followed for the dissolution of a CO_3 ion, and the free energy of dissolution was found to be ∼30 kJmol^{-1} [42]. The same study also considered the removal of

ions sitting on top of the flat surface, 'on-top' ions. These ions had much lower free energy changes upon dissolution, at 16.2 kJmol^{-1} for a Ca ion and 2.44 kJmol^{-1} for a CO_3 ion. We would therefore expect any on-top ions to dissolve first in a dissolution process. A separate investigation, also using classical simulations, found a very similar free energy difference in dissolution processes. Desorption of a Ca ion was found to give an energy difference of 16.3 kJmol^{-1} and dissolution of a CO_3 ion gave an energy difference of 9.3 kJmol^{-1} [7]

Apart from the flat surface, another likely site of dissolution is at a step. Atomistic MD simulations of CO_3 and Ca ions dissolving from the acute and obtuse steps showed that, as might be expected, the energy barrier to dissolution at both steps and for both ions was considerably less than for dissolving the ions directly from a flat surface. Dissolving a Ca ion from a step was found to be more favourable than from a flat surface by over 100 kJmol^{-1}. The difference is significantly less when considering a CO_3 ion, but is still substantial at ∼10 kJmol^{-1} [42].

The overall energy barrier to dissolution is lower for the CO_3 ion compared to the Ca ion, therefore dissolution is most likely to occur initially through the removal of a CO_3 ion from a step. However, simulations also showed that CO_3 ion dissolution is helped by the prior dissolution of a neighbouring Ca ion [42].

Another atomistic MD study also looked at dissolution from the $\{31\bar{4}8\}$ and $\{3\,\bar{1}\,\bar{2}\,16\}$ surfaces. As noted in 2.2.3 when the two steps are unhydrated the acute step has a lower surface energy. Removal of a $CaCO_3$ unit from a step did not change the relative energy between the surfaces greatly [41]. When two $CaCO_3$ units were removed it was found to be preferable that the units were adjacent (rather than dispersed along the step) creating one, not two, kink sites on an unhydrated surface. Classical MD simulations of hydrated stepped surfaces showed that the energy needed to dissolve $CaCO_3$ units from the obtuse step requires less energy than from the acute step. Dissolving the first $CaCO_3$ unit requires the most energy on both steps. The difference in dissolution energies suggests the obtuse step will dissolve significantly faster than the acute step in water, which is confirmed by experiments [43].

It is unlikely that in nature a calcite surface will be in contact with pure water, as many calcite systems are in marine environments. Consequently, the influence of

salt solution on dissolution is important. Classical MD simulations that considered a calcite surface in contact with a salt solution found a build up of negative charge, due to chlorine ions, at 2.7Å above the surface, and a region of positive charge due to sodium ions 4.5Å above the surface. When the solution was looked at as a whole, the Na ions were spread throughout the solution, while the distribution of the Cl ions tended to coincide with the water layers. The free energy profile of dissolving a calcium ion from the $\{10\bar{1}4\}$ surface indicated that as the salt concentration in the solution was increased the energy barrier to dissolving a Ca ion decreased, indicating that dissolution in salt water can be expected to occur more rapidly than in pure water [46].

2.2.6 Growth processes

The growth of calcite is important in the context of biomineralisation, in which organisms produce calcite for strengthening their structures.

Calcite precipitation has been observed in scanning electron microscopy (SEM) experiments [38]. The precipitation was observed with calcite samples in contact with a number of solutions. Before being subjected to a solution, samples were checked and shown to have relatively smooth surfaces with widely spaced terraces. When the calcite sample was placed in solution, small finger-like growths started to form on the surface. HCl and H_2CO_3 were added to the solution, which increased the density of the growths, but also resulted in some etching away of the original surface. NaOH and $Ca(OH)_2$ were later added, which greatly increased the growth population density. When large amounts of $Ca(OH)_2$ were added to the solution rhombohedral crystals started to form on the surface.

When the adsorption of a Ca ion on the flat surface in contact with water was considered in a classical MD simulation, it was observed to adsorb to the surface above a CO_3 group, coordinated with a surface oxygen ion and surrounding water oxygen ions 3.3Å above the surface CO_3. The free energy barrier to adsorption was 13.9kJmol^{-1} with an adsorption rate of around 10^8s^{-1} for all the ions (corresponding to an adsorption every few nanoseconds) [34]. A carbonate ion has also been considered and the free energy barrier to adsorption was found to be 15.1 kJmol^{-1} [7].

2.2.7 Summary

The calcite-water interface has been studied in great detail, both experimentally and theoretically. Experiments have shown that while there is some restructuring on the surface when calcite is hydrated the change is not large [11]. Modelling of the calcite surface has established that the $\{10\bar{1}4\}$ surface is the most stable, with the lowest surface energy [8, 31]. Simulations of this surface in contact with a monolayer of water established a structured pattern of water molecules lying flat on the surface [8].

Experimental results from X-ray scattering data show that when calcite is under bulk water the first two water layers order at the surface [29]. These ordered layers also appear in classical simulations [34] suggesting reasonable agreement between the two methods as to the behaviour of bulk water at the surface

The discussion about the behaviour of water becomes more controversial when a thin layer of water on the calcite surface is considered. Experimentally there is evidence that the water dissociates. In particular the XPS data strongly suggests the presence of dissociated species on the surface [11]. However, theoretical calculations do not support this view and in fact suggest dissociation is not stable on the flat $\{10\bar{1}4\}$ surface [35]. Classical simulations have suggested dissociated species are stable at steps [9], but this has yet to be confirmed.

Dissolution of steps is expected to occur fastest at obtuse steps [41], which again is in agreement with experiment [43]. When growing, calcite was observed to form in finger-like growths [38].

Chapter 3

Computational Methods

3.1 Density Functional Theory

Density functional theory (DFT) starts from first principles and is based on the proposition that any property of a system of many interacting particles can be found from the ground state electron density. Without DFT a many-body wavefunction would have to be employed, which quickly becomes very large and unmanageable in calculations of systems consisting of more than a few atoms. As a result DFT has become the main method for calculating electronic structure in condensed matter. In this section the underlying principles of DFT will be explored, along with some of the practicalities of implementing the theory.

DFT focuses on the ground state of a system, although the fundamental precepts show that in principle all information about a system can be determined from the ground state electron density [47]. The materials studied in this thesis, calcite and water, both have large band gaps between the valence and conduction bands, they are therefore generally in the ground state. Consequently, DFT is an ideal technique for studying these materials and has been the main computational technique employed for the work presented in this thesis.

3.1.1 The many-body wavefunction

When there is more than one particle in a system, the wavefunction describing that system must be a function of the position of all particles: $\Psi((\mathbf{r}_1),(\mathbf{r}_2),...,(\mathbf{r}_N))$. If the particles do not interact with each other then the Hamiltonian that acts on them will be: $\hat{H} = \hat{H}_1 + \hat{H}_2... + \hat{H}_N$, which takes a long time to compute if the system is relatively large. However, if the particles do interact with each other, the calculation becomes even more complex and the computation time becomes extremely large [48].

When an interacting system of N electrons and nuclei charge, Z, at position $\mathbf{R}$ is considered the Hamiltonian is given by [47]:

$$\hat{H} = \sum_{i=1}^{N}(\frac{-\hbar^2}{2m_e}\nabla_i^2 - \sum_R \frac{Ze^2}{|\mathbf{r}_i - \mathbf{R}|} + \frac{1}{2}\sum_{j\neq i}^{N}\frac{e^2}{|\mathbf{r}_i - \mathbf{r}_j|}) \tag{3.1}$$

where h is Planck's constant and $\hbar = h/2\pi$, m_e is the mass of the electron, e is the electron charge, $\mathbf{r}_i$ is the position of the ith electron, and $\mathbf{r}_j$ is the position of the jth electrons. The first term in Equation 3.1 describes the kinetic energy of the system, the second term represents the interactions between the electrons and the ionic nuclei and the third term represents the electron-electron interactions.

It is possible to replace the middle term of this Hamiltonian with a fixed external potential, $V_{ext}(\mathbf{r})$, to represent all the ionic nuclei:

$$\hat{H} = \sum_i \frac{-\hbar^2}{2m_e}\nabla_i^2 + \sum_i V_{ext}(\mathbf{r}_i) + \frac{1}{2}\sum_i\sum_{j\neq i}\frac{e^2}{|\mathbf{r}_i - \mathbf{r}_j|} \tag{3.2}$$

This Hamiltonian forms the basis of DFT, which uses this $\hat{H}$ to find the ground state of a system. However, the many-body wavefunction is not used. Instead the electron density takes a fundamental role in the calculation. How and why this is possible is described in the following sections.

3.1.2 The Hohenberg-Kohn Theorems

The modern version of DFT originates in a paper written by Hohenberg and Kohn in 1964 in which they showed it is possible to determine the properties of any physical system from its ground state density [49]. Hohenberg and Kohn's theory is based on two theorems, outlined below.

Theorem I: For any system of interacting particles the external potential, $V_{ext}(\mathbf{r})$, will give rise to a unique ground state density, $n_0(\mathbf{r})$. It is also true that any given ground state density will be determined by a unique external potential.

Proof: For a collection of electrons in a box under the influence of an external potential, $V_{ext}(\mathbf{r})$, the Hamiltonian has the form:

$$\hat{H} = \hat{T} + \hat{V} + \hat{U} \tag{3.3}$$

where $\hat{T}$ is the kinetic energy contribution given by:

$$\langle \hat{T} \rangle = \frac{1}{2} \int \nabla \Psi^*(\mathbf{r}) \nabla \Psi(\mathbf{r}) d(\mathbf{r}) \tag{3.4}$$

$\hat{V}$ is the energy contribution from the electron interaction with the ionic nuclei and any other external potential given by:

$$\langle \hat{V} \rangle = \int V_{ext}(\mathbf{r}) \Psi^*(\mathbf{r}) \Psi(\mathbf{r}) d(\mathbf{r}) \tag{3.5}$$

and $\hat{U}$ is the energy contribution from the electron-electron interactions given by:

$$\langle \hat{U} \rangle = \frac{1}{2} \int \frac{1}{|\mathbf{r} - \mathbf{r'}|} \Psi^*(\mathbf{r}) \Psi^*(\mathbf{r'}) \Psi(\mathbf{r}) \Psi(\mathbf{r'}) d\mathbf{r} d\mathbf{r'} \tag{3.6}$$

The electron ground state density is given by the following equation:

$$n(\mathbf{r}) = \langle \Psi_0 | \Psi^* \Psi | \Psi_0 \rangle \tag{3.7}$$

where Ψ_0 is the ground state wavefunction. From this equation it can be seen that as the density depends on Ψ_0, and Ψ_0 is a functional of the external potential, $V_{ext}(\mathbf{r})$, the density will be dependent on the external potential.

A second external potential, $V'_{ext}(\mathbf{r})$ with a ground state wavefunction Ψ'_0 is now considered.

Defining the ground state Hamiltonian and ground-state energies for the two states Ψ_0 and Ψ'_0 as $\hat{H}$ and $\hat{H}'$, and E and E' respectively, and taking into account that Ψ'_0 cannot be equal to Ψ_0, as they satisfy different Schrödinger equations, we then consider the minimal property of the ground state:

$$E' = \langle \Psi'_0 | \hat{H}' | \Psi'_0 \rangle < \langle \Psi_0 | \hat{H}' | \Psi_0 \rangle = \langle \Psi_0 | (\hat{H} + \hat{V}' - \hat{V}) | \Psi_0 \rangle \tag{3.8}$$

so that:

$$E' < E + \int [V'_{ext}(\mathbf{r}) - V_{ext}(\mathbf{r})] n(\mathbf{r}) d\mathbf{r} \tag{3.9}$$

If we then swap the dashed and non-dashed quantities we find the following inequality:

$$E < E' + \int [V_{ext}(\mathbf{r}) - V'_{ext}(\mathbf{r})] n(\mathbf{r}) d\mathbf{r} \tag{3.10}$$

If equations 3.9 and 3.10 are added together, an inconsistency occurs:

$$E + E' < E + E' \tag{3.11}$$

Thus we have shown that not only is $n(\mathbf{r})$ a unique functional of $V_{ext}(\mathbf{r})$, but also that $V_{ext}(\mathbf{r})$ is a unique functional of $n(\mathbf{r})$.

Theorem II: The ground state energy can be obtained using the variational principle. The ground state energy is the minimum of the energy functional, and the density that produces this minimisation is the ground state density, $n_0(\mathbf{r})$.

Proof:

As Ψ_0 is a functional of $n(\mathbf{r})$, the kinetic and interaction energies are also functionals. F[n] is defined as a universal functional that contains the electron interaction and kinetic energies:

$$F[n(\mathbf{r})] \equiv \langle \Psi_0 | (\hat{T} + \hat{U}) | \Psi_0 \rangle \tag{3.12}$$

An energy functional can then be defined as:

$$E_{V_{ext}}[n(\mathbf{r})] = F[n(\mathbf{r})] + \int V_{ext}(\mathbf{r}) n(\mathbf{r}) d\mathbf{r} \tag{3.13}$$

Then $n(\mathbf{r})$ equal to the ground state density, will give the $E_{V_{ext}}[n]$ equal to the ground state energy.

The energy functional of Ψ' will have a minimum at the correct ground state wavefunction, Ψ_0. If Ψ' is varied by using different external potentials then the energy becomes:

$$\varepsilon_{V_{ext}}[\Psi'] = \int V_{ext}(\mathbf{r}) n'(\mathbf{r}) d\mathbf{r} + F[n'] > \varepsilon_{V_{ext}}[\Psi_0] = \int V_{ext}(\mathbf{r}) n(\mathbf{r}) d\mathbf{r} + F[n] \tag{3.14}$$

This implies that all densities other than the ground state density will lead to a higher energy than the ground state energy. (If the functions allowed are restricted by the condition $N[n] \equiv \int n(\mathbf{r}) d\mathbf{r} = N$, where N is the total number of electrons in a system.)

If the functional $F[n]$ was known, and was relatively simple, calculations to determine the ground state energy would become reasonably easy, as solving them would only require minimising a functional of the density function. However, determining the functional is not straight forward and many of the difficulties in determining the ground state arise from the functional complexity.

3.1.3 Kohn-Sham

As the functional $F[n]$ is complex, density functional theory was not a useful technique until Kohn and Sham published a paper in 1965 that led to a practical implementation of the theory [50]. Their idea consisted of replacing the ground-state density of an interacting system with an identical ground-state, but for a non-interacting

system in an effective potential. This concept leads to independent-particle equations for the non-interacting system, which are exactly solvable and give the same result as for the interacting system.

There are two main assumptions in Kohn and Sham's proposal:

I. The ground state density of an interacting system can be equal to that of a non-interacting system.

II. The Hamiltonian of the non-interacting system has a kinetic operator and an effective local potential, V_{eff}, which acts on any given electron and is $\hat{H} = -\frac{\hbar}{2m}\nabla^2 + V_{eff}$.

In the Kohn-Sham approach the ground state energy functional can be broken down into four components:

$$E_{KS} = T_S[n] + \int V_{ext}(\mathbf{r})n(\mathbf{r}) + E_{Hartree}[n] + E_{II} + E_{xc}[n] \; d\mathbf{r} \tag{3.15}$$

where $T_S[n]$ is the kinetic energy of the independent, non-interacting, particles, $V_{ext}(\mathbf{r})$ is the external potential (as defined in Section 3.1.2) describing the nuclei and any external fields that are applied to the system, $E_{Hartree}[n]$ is the classical Coulomb energy of the electron density interacting with itself, E_{II} is the interaction energy between the nuclei and $E_{xc}[n]$ is the exchange-correlation functional containing all the many-body effects of the system.

It is possible to write E_{xc}[n] in terms of the Hohenberg-Kohn functional, $F[n(\mathbf{r})]$:

$$E_{xc}[n] = F[n(\mathbf{r})] - (T_S[n] + E_{Hartree}[n]) \tag{3.16}$$

which can also be written:

$$E_{xc}[n] = \langle\hat{T}\rangle - T_S[n] + \langle\hat{V}_{int}\rangle - E_{Hartree}[n] \tag{3.17}$$

where $\langle\hat{T}\rangle$ is the kinetic energy expectation value of the interacting electrons and $\langle\hat{V}_{int}\rangle$ is the potential energy of the interacting electrons.

Equation 3.17 shows that $E_{xc}[n]$ is the difference in the kinetic and internal interaction energies of the true interacting system and those of the non-interacting system,

with the electron-electron interactions replaced with the Hartree energy [47].

The Kohn-Sham equations can be derived from Equation 3.15 and are as follows:

$$(\hat{H}_{KS} - \epsilon_i)\psi_i(r) = 0 \tag{3.18}$$

where ϵ_i are the eignevalues and $\hat{H}_{KS}$ is the effective Hamiltonian given by:

$$\hat{H}_{KS}(\mathbf{r}) = \frac{-\hbar}{2m}\nabla^2 + V_{KS}(\mathbf{r}) \tag{3.19}$$

and $V_{KS}(\mathbf{r})$ is given by

$$V_{KS}(\mathbf{r}) = V_{ext}(\mathbf{r}) + V_{Hartree}(\mathbf{r}) + V_{xc}(\mathbf{r}) \tag{3.20}$$

These equations are independent of any approximation associated with the functional, $E_{xc}[n]$. If this functional was known, it would be possible to solve the equations for the ground state energy and density for the interacting system exactly.

3.1.4 Exchange-correlation functionals

So far we have seen that there is a one-to-one relationship between the ground state density and an external potential, and that the ground state energy can be found by using the variational principle. The interacting electron system has been replaced with a non-interacting system in an effective potential, and the exhange and correlation terms have been separated out of the Hamiltonian into the exchange-correlation functional, $E_{xc}[n]$.

This energy can be expressed as an integral of the density at all points in the system:

$$E_{xc}[n] = \int n(\mathbf{r})\varepsilon_{xc}([n], \mathbf{r}) \; d\mathbf{r} \tag{3.21}$$

where $\varepsilon_{xc}([n], \mathbf{r})$ is the energy per electron at point $\mathbf{r}$, which depends only on the density in the region of $\mathbf{r}$. If the form of $E_{xc}[n]$ was known, the exact ground state energy and density could be found. Unfortunately, $E_{xc}[n]$ is not known exactly and an approximation must be employed. There are two main schemes in use; the local density approximation (LDA) and the generalised gradient approximation (GGA).

These will be discussed below.

Localised Density Approximation (LDA)

The theory of Kohn and Sham was only useful in practice because of the development of exchange-correlation functionals that could be implemented in numerical calculations. Kohn and Sham suggested the first of these functionals, the local density approximation (LDA), in the same paper in which they introduced the idea of the exchange-correlation functional [50].

Kohn and Sham noted that many solids are close to the limit of the homogeneous electron gas, and so the exchange and correlation effects are local. They proposed LDA, in which $E_{xc}[n]$ is assumed to be the same as for a homogeneous electron gas of the same density. LDA is the simplest possible representation of the functional properties [47].

The exchange-correlation functional is given by Equation 3.21. In LDA $\epsilon([n], \mathbf{r})$ depends only on the density at a small region around the point $\mathbf{r}$. When using LDA, one assumes that the exchange and correlation effects in the system are short range in the solid being investigated. LDA works best for materials that are closest to a homogeneous electron gas, such as nearly-free-electron metals.

Generalised Gradient Approximation (GGA)

The use of LDA in practical modelling calculations showed that DFT could produce results that agreed with experiment, providing the support needed for further development. To improve the functional, generalised gradient approximations (GGAs) were developed, which improved on the original LDA. Changing the functional from LDA to any form of GGA reduces the exhange energy and the binding energy, correcting the overbinding in LDA, and leading to better agreement with experiments [47].

In GGA the $\mathrm{E}_{xc}[n]$ depends on the gradient of the density at each point, ∇n, as well

as the density, and becomes:

$$E_{xc}[n] = \int n(\mathbf{r})\epsilon_{xc}([n], \nabla n) \tag{3.22}$$

or

$$E_{xc}[n] = \int n(\mathbf{r})\epsilon_x^{hom}(n)F_{xc}([n], \nabla n) \tag{3.23}$$

where $F_{xc}([n], \nabla n)$ is dimensionless and $\epsilon_x^{hom}(n)$ is the exchange energy of the homogeneous electron gas. The choice of $F_{xc}([n], \nabla n)$ is important and different forms of this factor have been proposed. The difference in these functionals arises because they have been designed to preserve different properties at high density gradients. In this thesis two forms of GGA were used. The first, PW91, was proposed by Perdew and Wang [51], and the second, PBE, was proposed by Perdew, Burke and Enzerhof [52].

LDA and GGA are very good approximations, particularly for describing materials with a wide band gap, such as the group IV semi-conductors and insulators like diamond and NaCl [47]. However, they are not good for describing systems with strongly correlated electrons.

3.1.5 Self-consistency

At this point it is worth considering how a real DFT calculation is performed. Numerical methods are required for solving the Kohn-Sham equations. In order for a calculation to be converged the effective potential, V_{eff}, and the density, $n(\mathbf{r})$, must be consistent with each other. The density depends on the potential, and the potential depends on the density. Therefore a self-consistency loop is employed in a numerical calculation to iterate between the two parameters until a self-consistent solution is reached.

Inside the self-consistency loop the charge density and wavefunctions are independent quantities. The charge density is first used to set up a Hamiltonian, then the wavefunctions are optimised iteratively to get closer to the exact wavefunctions of this Hamiltonian. A new charge density is calculated from the optimised wavefunctions, which is then mixed with the original input density. This process continues

until the energy of the input density and the optimised wavefunctions are the same, or fall within a specified range. This scheme is illustrated in Figure 3.1.

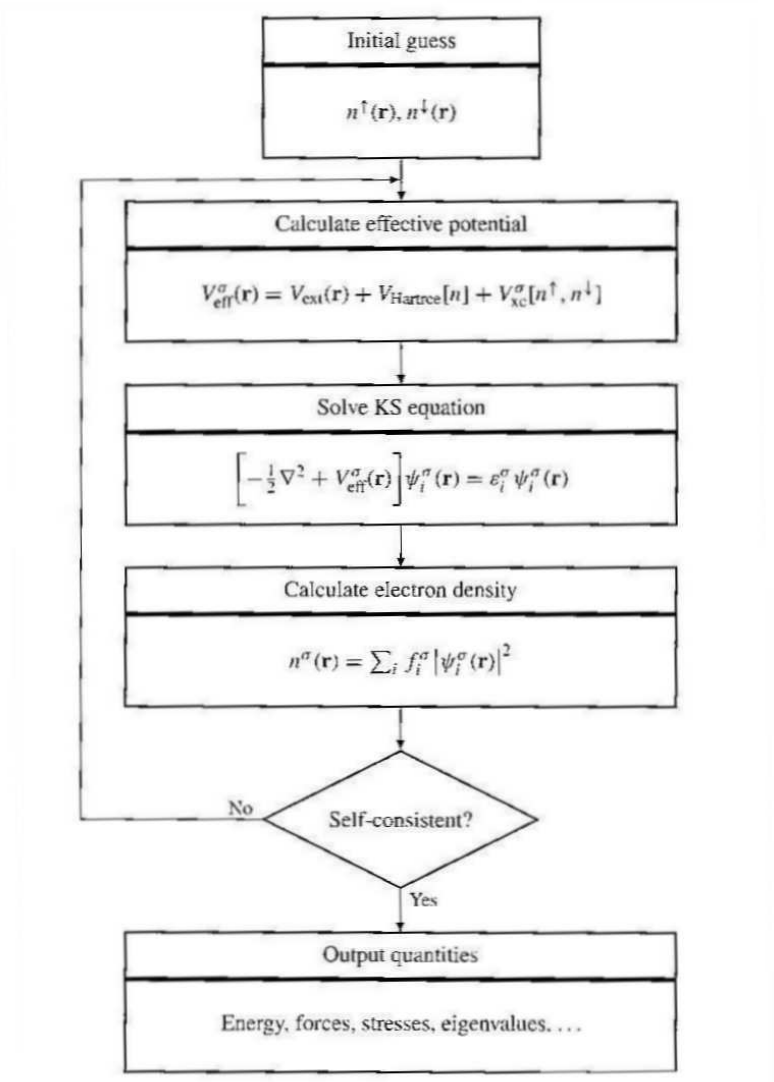

Figure 3.1: Representation of the self-consistency loop used in solving the Kohn-Sham equations in numerical calculations. [47]

When the self-consistency loop is completed, the forces on the ions in the calculation are computed and used to move them to new positions. In a static relaxation the atoms are moved according to the calculated forces, moving the system into an energy minimum. This continues until the forces are less than a specified value, at which point the ions are in their minimum energy positions. There are several methods for reaching the energy minimum [53]. The simplest is known as 'steep-

est descent' (SD) in which the energy function is minimised by moving along the direction of the gradient, directly towards the minimum. Another common method is 'conjugate-gradient' (CG) in which the system is moved towards its minimum by combining information about the current function value and the current gradient. A third method is 'quasi-Newton' in which information about succesive gradients is used to find the minimum. In an MD simulation, ions are initially assigned velocities based on a Maxwell-Boltzman distribution for a particular temperature. The movement of the ions within the simulation is then determined by Newton's laws of motion.

3.1.6 Periodic boundary conditions and plane wave basis sets

When running a real numerical calculation, it is not feasible to explicitly include all the electrons in a real crystal ($\sim 10^{23}$). To overcome this problem periodic boundary conditions are introduced for solid state crystals, allowing calculations on one 'supercell'. This supercell contains a limited number of atoms, but is representative of the entire crystal. Within the calculation the cell is repeated to create an infinite array. This is possible because of Bloch's theorem, which states that the eigenfunctions of the wave equation for a periodic potential are the product of a plane wave ($exp(i\mathbf{k}.\mathbf{r})$) times a function with the periodicity of the crystal lattice ($\mathbf{u_k}(\mathbf{r})$), which can be expressed mathematically as:

$$\Psi_k(\mathbf{r}) = \mathbf{u_k}(\mathbf{r})exp(i\mathbf{k}.\mathbf{r}) \tag{3.24}$$

where $\mathbf{k}$ is the wavevector [54].

The periodic function, $\mathbf{u_k}(\mathbf{r})$, can be expressed as a set of plane waves with wave vectors the same as the crystal's reciprocal lattice vectors:

$$\mathbf{u_k}(\mathbf{r}) = \sum_G c_{k,G} exp[i(\mathbf{k}+\mathbf{G}).\mathbf{r}] \tag{3.25}$$

where $\mathbf{G}$ represents the reciprocal lattice vectors (defined as $\mathbf{G}.\mathbf{l} = 2\pi m$, where $\mathbf{l}$ is the lattice vector of the crystal and m is an integer). This is the wavefunction basis

set [53]. Using the Bloch theorem allows the calculation to be performed only in the first Brillouin zone, simplyfing it and reducing the computational cost.

In principle the plane-wave basis set required is infinite, but this is impractical. Instead the basis set is truncated by including only plane waves with low kinetic energy, as the coefficients for these are larger, and therefore more important, than high kinetic energy coefficients. This truncation will lead to an error in the total energy calculated, but this can be reduced by checking for convergence in the system. In Section 3.1.7 pseudopotentials will be discussed. These potentials provide a practical way of overcoming the requirement to have very large numbers of plane waves in a calculation.

k-point sampling

Using the Bloch theorem changes the problem from one of an infinite number of electronic wavefunctions to one of calculating a finite number of wavefunctions at an infinite number of k-points. The states that are occupied at each k-point contribute to the overall electronic potential in the bulk solid. As the electronic wavefunctions at k-points close together are very similar it is possible to represent the wavefunction over a region of space by considering the contribution at one point in k-space [53].

A number of methods have been developed for obtaining accurate approximations to the electronic potential by sampling specific k-points in the Brillouin zone. One possible method was devised by Monkhorst and Pack, which generates special points in the Brillouin zone for sampling and has been shown to produce accurate results [55].

As previously mentioned, when running a numerical calculation, a 'supercell' is used, which consists of repetitions of a unit cell. As this cell becomes large the number of k-points required becomes lower. This is due to the value of $\mathbf{l}$ becoming longer and the reciprocal lattice vector $\mathbf{G}$ becoming shorter. In large systems the Brillouin zone contracts and fewer k-points are required to gain the desired accuracy.

3.1.7 Pseudopotentials

As the previous section has shown, the wavefunction of an atom can be expressed in terms of plane waves, but to fully describe the wavefunction large numbers of plane waves are needed. This will make any calculation very inefficient and require large amounts of computing time. This is particularly true near the atom core where the wavefunction is rapidly varying. It is for this reason that pseudopotentials are introduced.

Pseudopotentials can be used because the physical properties of a solid are mainly determined by the valence electrons. A pseudopotential is used to replace the strong Coulomb potential of the atom core and the effects of the tightly bound core electrons with an effective potential that matches the real one when it reaches a critical distance from the centre, r_c - the cutoff radius. This type of potential will accurately describe the valence electrons. Figure 3.2 shows a schematic diagram of a pseudopotential.

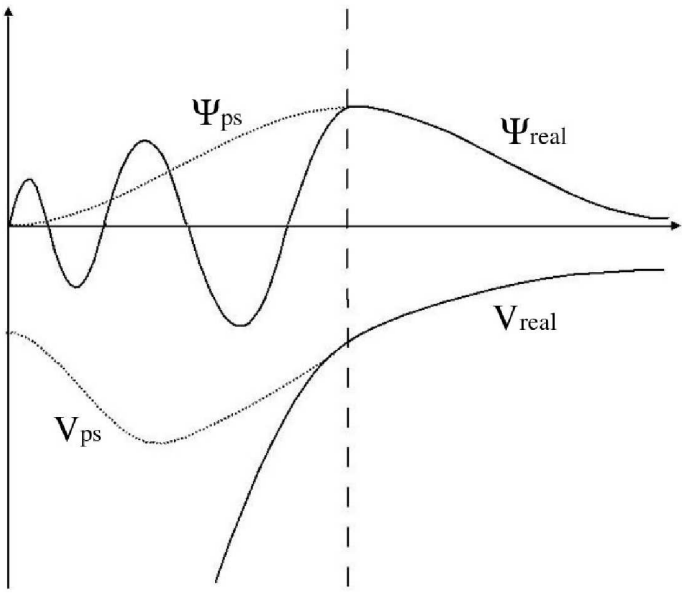

Figure 3.2: Illustration of a real potential, V_{real}, and a pseudopotential, V_{ps}, along with the real and pseudo wavefunctions, Ψ_{real} and Ψ_{ps}.

There are two main, contradictory, properties that are desirable from a pseudopotential. The first is transferability. It is preferable that the pseudopotential is

independent of its environment, which requires a small cutoff radius. However the second property is 'softness' (ie. that the wavefunction is smooth), which will lead to fast converging plane-wave expansions, but requires a large cutoff radius [56].

Making a pseudopotential requires balancing these competing properties. A number of schemes have been introduced for pseudopotentials. They all assume the core electrons are frozen and do not adapt to their surroundings, but other aspects vary. In general there are two types of pseudopotential. The first are total pseudopotentials in which an effective all-electron potential includes the effect of the core and the other valence electrons. The second are potentials that only treat the valence electrons and are used in combination with the Hartree and exchange-correlation potential created by other valence electrons [56].

Ultra-soft pseudopotentials are from the latter group and were used in the work presented in this thesis. They are discussed further below.

Ultra-soft pseudopotentials (US-PP)

Ultrasoft pseudopotentials (US-PP) are designed to improve the accuracy of and reduce the computational time needed for a calculation. They have two parts, the first is a smooth function at the very core of the ion and the second is a more rapidly varying function around the core [47].

The work presented in this thesis used the form of US-PP proposed by Vanderbilt in 1990 [57]. These US-PP allow a reduction in the plane wave cutoff needed as the core part of the potential does not require as large a plane-wave basis set as other pseudopotentials. Figure 3.3 shows the difference between previous pseudopotential wavefunctions and the ultra-soft wavefunction.

3.1.8 Projector Augmented-Waves (PAW)

A different approach to pseudopotentials, initially proposed by Blochl [58] and later worked on by Kresse and Joubert [59], aims to improve upon the pseudopotential method by re-introducing the exact core wave functions. This allows all the electrons in the system to be involved in the calculation (unlike in pseudopotentials where the

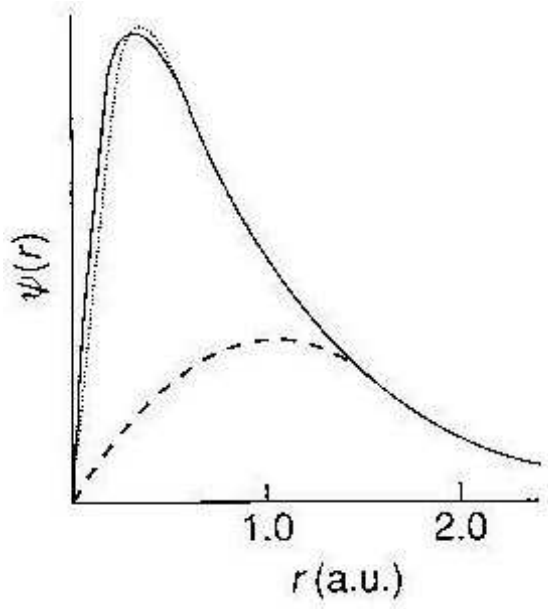

Figure 3.3: Oxygen $2p$ radial wave function for use with LDA. The solid line shows the function where all electrons are treated, the dotted line shows a pseudofunction and the dashed line shows an ultra-soft pseudofunction. [57]

core electrons are treated as a frozen unit unable to change during the calculation). This is achieved through introducing an invertible linear operator that maps between true and pseudo wavefunctions ($\psi = \tau\tilde{\psi}$). The introduction of the translation allows the calculation of the true expectation value, using $\tilde{A} = \tau^{\dagger}A\tau$. This can be done by defining the dynamical variables from the pseudo part of the calculation as [60]:

$$\langle A\rangle = \langle\psi|A|\psi\rangle = \langle\psi|\tau\tau^{\dagger}A\tau\tau^{\dagger}|\psi\rangle = \langle\tilde{\psi}|\tilde{A}|\tilde{\psi}\rangle \tag{3.26}$$

This method is analgous to pseudopotentials in that it introduces projectors acting on smooth valence functions. However, it differs from these functions by keeping all the information about the core states, unlike in US-PP [47].

In PAW the valence wavefunctions are expressed as a sum of smooth functions plus core functions. PAW retains the entire set of all-electron core functions, along with the smooth part of the valence functions. When a real numerical calculation is performed the integrations are split between those of the smooth functions in the whole space and those over the rapidly varying functions inside the spheres around

the atoms [56].

3.2 Molecular Dynamics

The use of molecular dynamics (MD) simulations allows fuller exploration of configuration space compared to static relaxations. This exploration is possible as the ions gain enough potential energy to jump over small energy barriers when a simulation is performed at a non-zero temperature. A simplified version of the steps required of an MD program are shown in Figure 3.4. The main components are the calculation of the forces on all atoms, followed by the integration of Newton's equation of motion, $F = ma$ (where F is the force, m is the mass and a is the acceleration). Of these steps the first takes most of the computing time.

To initialise a simulation all the particles in the system are assigned a velocity using a Maxwell-Boltzman distribution. In thermal equilibrium the following relation between the velocities and temperature should be true:

$$\langle v^2 \rangle = \frac{3k_B T}{m} \tag{3.27}$$

where v is a particle's velocity, T is the temperature, m is the particle's mass and k_B is the Boltzman constant [61].

The velocities of particles are not generally used in the calculation of the atom trajectories. Instead the past and present positions of the particles, along with information about the forces acting on the particles are used to predict the future particle positions [62]. To calculate the new positions an algorithm is required. One of the most commonly used is the Verlet algorithm:

$$r(t + \triangle t) \approx 2r(t) - r(t - \triangle t) + \frac{f(t)}{m} \triangle t^2 \tag{3.28}$$

where t is time, f is the force on the particle, $r(t - \triangle t)$ is the particle's position at the previous time step, $r(t)$ is the particle's position at the current time and $r(t + \triangle t)$ is the particle's position at the next time step. This algorithm computes the new position of the particles based on the forces acting on them at their previous positions, thus predicting the time evolution of a system.

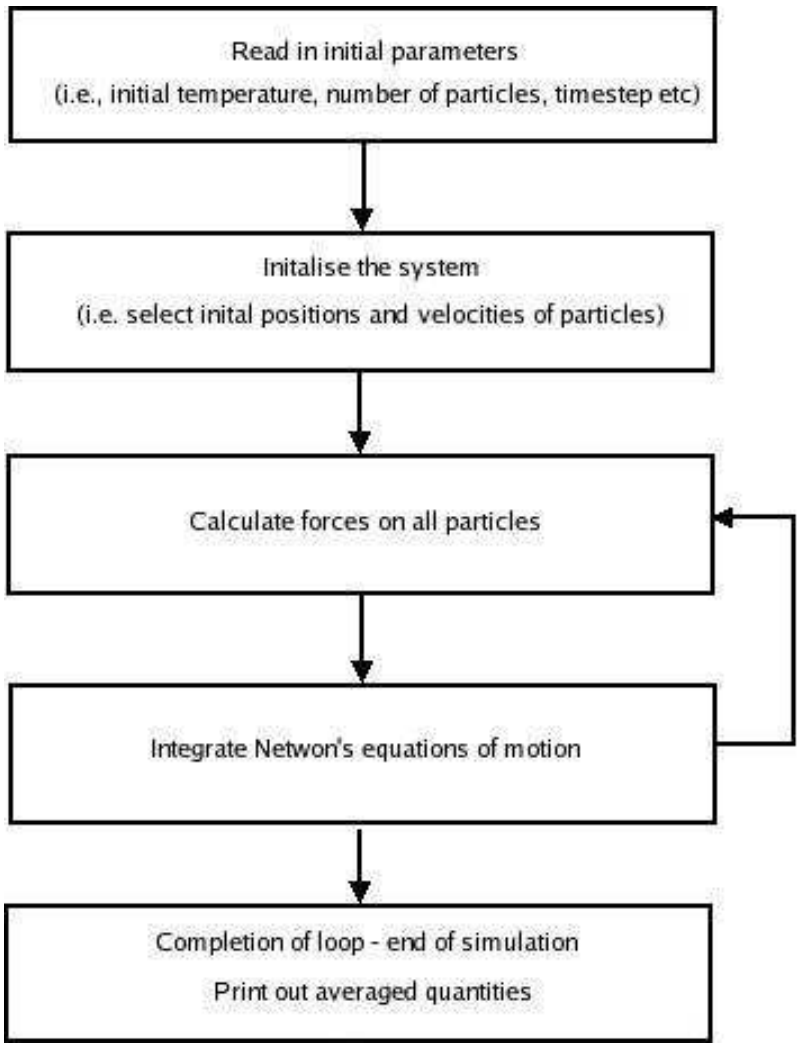

Figure 3.4: The important steps performed in an MD simulation.

MD simulations can be performed in several different ensembles. In the simplest calculations, the number of particles, volume and energy are kept constant using a microcanonical ensemble (NVE). In this ensemble fluctuations in temperature occur, which are described by:

$$\frac{[\langle T^2\rangle - \langle T\rangle^2]}{\langle T\rangle^2} = \frac{2}{3N}(1 - \frac{3k_B}{2C_v}) \tag{3.29}$$

where N is the number of particles and C_v is the heat capacity of the system at constant volume.

The temperature or pressure of a simulation can also be kept constant. The simulations presented in this thesis were performed at constant temperature, in the canonical ensemble (NVT). In these simulations it is not the temperature that fluctuates, but the energy. The equation describing this fluctuation is:

$$\frac{NC_v}{k_B} = (\frac{1}{k_BT})^2(\langle \hat{H}^2\rangle_{NVT} - \langle \hat{H}\rangle^2_{NVT}) \tag{3.30}$$

where $\hat{H}$ is the Hamiltonian of the system.

In order to maintain a constant temperature in a simulation a thermostat is required. The work in this thesis used the Nosé-Hoover thermostat. This thermostat enlarges the system's Lagrangian to include a ficticious mass, Q. Newton's laws of motion are then extended to include a 'friction' term:

$$a_i = F_i/m_i - \zeta v_i \tag{3.31}$$

where i is the specified atom and ζ is the friction coefficient, which fluctuates in time around zero and is given by:

$$\frac{d\zeta}{dt} = \frac{1}{Q}[\sum_{i=1}^{N} m_i v_i^2 - 3Nk_BT] \tag{3.32}$$

where t is time [61].

MD simulations can be performed using both DFT and classical methods. Classical methods do not represent chemical interactions and spontaneous dissociation of molecules cannot occur during a classical simulation. As one of the primary aims

of this work was to investigate the dissociation of water, classical simulations would not provide the information desired. DFT MD was therefore used to explore the question of dissociation. However, some classical MD simulations have been run as part of the development of the consortium's calcite-water potential. Classical MD and forcefields are discussed below.

3.3 Classical MD and Forcefields

While classical simulations are not able to represent chemical reactions, they offer an opportunity to run simulations with more atoms on longer timescales compared to DFT MD simulations. Classical potentials allow large numbers of ions to be simulated (several million) and can be run for nanoseconds compared to DFT simulations where several hundreds of atoms can be simulated, mainly on picosecond timescales.

The motivation behind the development of classical potentials is a desire to represent the chemistry between atoms, without having to explicitly describe the electrons. The interactions are instead represented by simple functional forms that describe the forces between atoms and molecules. Covalent bonds are described using bonded potentials, the simplest form of which is a harmonic potential. Ionic bonds are represented by non-bonded potentials, which include both the Coulomb potential and the long range van der Waals interaction.

3.3.1 Bonded potentials

There are a number of methods for describing covalent bonds in bonded potentials, depending on the level of complexity required. The most straight forward interaction is between two atoms (a 2-body interaction) and depends on the distance between the atoms. If a third atom is introduced a 3-body interaction is created, which includes the angle between the atoms as well as the distances between them. Finally, a 4-body interaction also includes the dihedral angle between the three bonds.

While the simplest bonded potential is the harmonic potential, a number of others are available. One of these is the Morse potential in which the bond lengths are

used to represent the energy, resulting in a very repulsive force field. This potential takes the form:

$$V = E_0[\{1 - exp(-k(r_{ij} - r_0))\}^2 - 1] \tag{3.33}$$

where E_0 is the energy when the bond length is at equilibrium, k is a force constant, r_{ij} is the current bond length between two atoms and r_0 is the equilibrium bond length. The Morse potential is one of the potentials used to simulate calcite in classical calculations. The r_{ij} and r_0 terms are used to represent the covalent bonds between the carbon and oxygen in the carbonate groups when a Morse potential is used.

3.3.2 Non-bonded potentials

Non-bonded potentials describe ionic bonds and contain two terms. The first term describes the overlap of atomic orbitals and ensures that at close range there is strong repulsion between atoms, to mimic the Pauli exclusion principle. The second term describes the long range interactions; the dispersion of the atoms and van der Waals interactions. The second term is designed to describe the dipole-dipole or fluctuating dipole (where a dipole is briefly induced in an otherwise dipole free atom) moments between atoms. Generally either a Lennard-Jones or Buckingham potential are used for non-bonded potentials.

However, the Born potential is simpler than these potentials, it neglects the dispersive term and takes the form:

$$V = Aexp(-\frac{r_{ij}}{\rho}) + \frac{z_i z_j e^2}{r_{ij}} \tag{3.34}$$

The first term is the overlap term that ensures repulsion at close range and the second term in the Coulomb potential.

The Lennard-Jones potential has the form:

$$V = 4\epsilon[(\sigma/r_{ij})^{12} - (\sigma/r_{ij})^6] \tag{3.35}$$

where ϵ is a parameter with dimensions of energy and σ is a parameter with dimensions of length. The first term provides the repulsive overlap, to ensure atoms do

not get too close together, and the second term is the dispersive term that describes the long range interactions.

The Buckingham potential is another common non-bonded potential and is also used to simulate the interaction between Ca and O ions in calcite. This potential takes the form:

$$V = Aexp(-\frac{r_{ij}}{\rho}) - \frac{c}{r_{ij}^6} \tag{3.36}$$

where A, ρ and c are fitting parameters. These parameters are fitted to experimental data such as the lattice parameter and elastic constant. In the Buckingham potential, the repulsive term is provided by the exponential and the long-range attraction is given by the $1/r^6$ term.

3.3.3 Calcite potentials

Potentials for specific materials are often developed to include elements from different potentials in order to represent material properties accurately. The Pavese potential has been developed to simulate calcite more accurately by combining the Morse, Buckingham and Coulomb potentials [63, 64]. It was fitted to structural properties, elastic constants and vibrational frequencies found from experiment. The potential was based on a Born-type potential describing the Ca-O and O-O bonds in the crystal. While the C-O bonds in the carbonate ions are described by the Morse potential. The oxygen is described by a shell model, which makes it polarizable.

3.3.4 Combining organic and mineral forcefields

When an interaction between two materials is being investigated it is necessary to find a way of combining the force fields of both materials. One way of doing this is to use Lorentz Berthelot mixing rules. These use Lennard-Jones type potentials and define the new value of ϵ (a parameter with dimensions of energy as in Equation 3.35) as $\epsilon_{ab} = \sqrt{\epsilon_a \epsilon_b}$ (where $\epsilon_a = \epsilon$ of material 'a', $\epsilon_b = \epsilon$ of material 'b' and $\epsilon_{ab} = \epsilon$ when the two materials are combined), and the new value of σ (a parameter with dimensions of length as in Equation 3.35) as $\sigma_{ab} = \frac{1}{2}(\sigma_a + \sigma_b)$ (where $\sigma_a = \sigma$ of material 'a', $\sigma_b = \sigma$ of material 'b' and $\sigma_{ab} = \sigma$ when the two materials are

combined). However, these mixing rules can be problematic if the two materials involved use different types of forcefield.

For example, organics and minerals are described by different types of forcefields in simulations. Minerals have a formal charge and are described by Born model potentials, while potentials for organic materials have a partial charge and include van der Waals interactions represented by Lennard-Jones potentials. Consequently, the mixing rules are found to work well for interactions between organic molecules, but fail when describing interactions between organic molecules and inorganic mineral crystals [15].

As has been previously noted, it is difficult to combine materials that are described by different types of charges. In the case of organics and minerals, minerals are generally modelled using formal charges, when an atom is assigned a specific charge denoted by its position in the periodic table. For example oxygen will have a charge of -2 and silicon will have a charge of +4. However, organic materials, and water, are modelled using partial charges, when atoms are assigned non-integer charges. These charges arise in real atoms from the asymmetric distribution of electrons and the use of partial charges in classical simulations is designed to replicate this situation.

When a mineral is modelled in contact with an organic material, or water, the two types of potential need to be integrated. Left unchanged the attraction between the materials would be too strong. The modification is done through altering the repulsive term.

An example is a zeolite modelled by Schröder et al. A potential with charges of $Al^{3+}O^{2-}$ was simulated interacting with a hydroxyl potential with charges of $O^{1.4-}H^{0.4+}$ [65]. The charge on the zeolite oxygen was changed so that the new charges would be $Al^{3+}O^{1.4-}$. However, the aluminium charge also had to be modified to ensure charge neutrality. The new charges were found by combing the equations $q_O = -2/3q_{Al}$ and $-3 \times 1.426 = q_O q_{Al}$. The potential was then refitted to obtain the potential parameters (for example A, ρ and c in the Buckingham potential) with the new partial charges and used for the cross-interaction.

De Leeuw and Parker introduced a procedure that involves scaling the repulsive

term, avoiding the lengthy process of refitting the potential [8]:

$$A_{new} = A_{mineral}(q_{O(organic)}/q_{O(mineral)}) \tag{3.37}$$

This method provided results in good agreement with a potential that had been refitted to experimental data. This method therefore speeds up the process of devising new potentials.

One of the main aims of the consortium, of which this work is a part, has been to devise a new methodology for generating force fields at the interface between materials, in particular between minerals and organics. Consortium members in Sheffield have generalised the Schröder procedure to apply to the interaction between minerals and organic materials [14]. While the work presented in this thesis does not involve organic materials in contact with a mineral, this method has also been applied to the water-calcite interaction and will therefore be tested in this thesis.

Chapter 4

Investigation of percentage water coverage on the calcite $\{10\bar{1}4\}$ surface

4.1 Methods

VASP

The density functional theory (DFT) simulation package VASP (Vienna Ab-initio Simulation Package) [66, 67, 68, 69] was used for a series of static relaxations and molecular dynamics (MD) simulations, which are presented in this Chapter and Chapter 5. Details of DFT were given in Chapter 3.

Four input files are required for VASP, one containing information about the pseudopotentials of the ions in the calculation (*POTCAR*), one containing the lattice vectors and ion positions (*POSCAR*), one containing directions about the k-point mesh to be used during a calculation (*KPOINTS*) and one containing a variety of convergence critieria and other calculation control functions (*INCAR*).

Information about the simulation periodic cell is contained in *POSCAR*. During a calculation VASP creates an infinite array in the x, y and z directions of this periodic 'supercell', meaning calculations are essentially being performed on an infinite

surface. The 'vacuum gap' at the top of a periodic cell (the gap left between the top of the surface in one cell and the bottom of the surface in the next) must be large enough that interaction between the bottom of one surface and the top of the next is kept to a minimum, which must be tested for during convergence calculations. *POSCAR* can also be used to control whether atoms are allowed to move or not. It is possible to constrain an atom in any or all directions.

The importance of k-points in DFT calculations was explained in Section 3.1.6. The *KPOINTS* file allows specification of the number of k-points to be used in each direction during a VASP calculation. Again, the number of k-points in a calculation must be considered in any convergence testing and were investigated fully in this work. Convergence tests for the work presented here are discussed in Section 4.2.

A number of criteria can be controlled in *INCAR*, of particular importance is the plane wave cutoff energy, which can be set to high, medium or low. As discussed in Section 3.1.6 it is important to include a high number of plane waves to increase the accuracy of the wavefunction representation, but a compromise must be made to take into account computation time. In the *POTCAR* file minimum and maximum energy cutoffs are defined for each ion type. At a low energy cutoff setting in *INCAR* the highest minimum value from *POTCAR* will be used, at a medium setting the highest maximum value will be used and at a high setting the highest maximum value plus 30% are used in a calculation. For calculations of calcite crystal, a high setting corresponds to a plane wave cutoff of 515eV, a medium setting corresponds to a plane wave cutoff of 396eV and a low setting corresponds to a plane wave cutoff of 297eV.

Several algorithms are available for use in VASP, both quasi-Newton and conjugate-gradient (CG) algorithms were used during the calculations presented here to find the minimum in the energy function. In the CG alogorithm the system is moved towards its minimum by combining information about the current function value and the current gradient [53]. Generally quasi-Newton, in which information about succesive gradients is used to find the minimum, is more efficient, but sometimes appeared to get caught between two energy minima - hopping between the two without converging. The CG algorithm proved useful in this context as it was often able to overcome this problem and converge on one energy minima.

4.2 Convergence tests

Convergence of bulk calcite

While the ultimate aim of this work was to simulate the calcite-water interface, it was necessary to approach the problem in several stages. The first of these was to perform a series of convergence calculations to ensure accuracy in future calculations. Static relaxations on bulk calcite using VASP provided the bulk energy, which was needed for future surface energy calculations, and allowed an investigation into the input parameters available in VASP.

A series of single point calculations were performed using a calcite primitive unit cell as the VASP supercell (shown in Figure 4.1(a)). The cell is monoclinic ($a \neq b \neq c$, $\alpha \neq \gamma \neq 90^o = \beta$ [70]) and the lattice vectors defining the unit cell were (given in Å):
a_1 = 4.9896000000y
a_2 = 8.0954789778z
a_3 = 3.0355475599x + -2.4948000000y + -3.0753100871z
These cell dimensions were used during all calculations presented in this thesis. Larger or smaller cells were scaled according to these original cell dimensions.

Due to the differing orientation of CO_3 groups in alternate rows, the unit cell contains two Ca atoms and two CO_3 groups . An array of several unit cells is shown in Figure 4.1(b), which illustrates the different CO_3 orientations.

A series of calculations using both the generalised gradient approximation (GGA) and the local density approximation (LDA) with Vanderbilt US-PS were performed, along with a series of PAW calculations, which also used PW91. (Details of these techniques can be found in Chapter 3.) For each method the number of k-points was varied from a $3 \times 3 \times 3$ grid to a $7 \times 7 \times 7$ grid in order to determine the lowest number needed to obtain reasonable convergence of the energy. This would reduce computing time as the more k-points a calculation has, the more processor hours it requires.

For a $4 \times 4 \times 4$ k-point grid, the energy cutoff in *INCAR* was set to both medium and high to test how this affected convergence. In the bulk static calculations presented

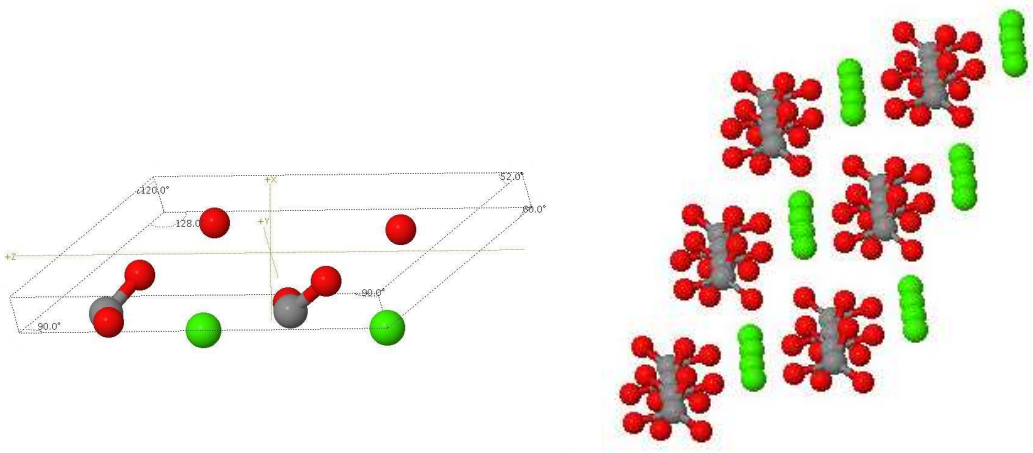

(a) (b)

Figure 4.1: (a) Calcite primitive unit cell used in bulk simulations. (b) Several unit cells. (Ca ions are green, O ions are red and C ions are grey.)

k-points	Energy cutoff	Total energy (eV)
$3 \times 3 \times 3$	high	-75.524213
$4 \times 4 \times 4$	medium	-75.531128
$4 \times 4 \times 4$	high	-75.528791
$5 \times 5 \times 5$	high	-75.528891
$6 \times 6 \times 6$	high	-75.528991
$7 \times 7 \times 7$	high	-75.529038

Table 4.1: US-PP GGA bulk calcite convergence

here, all the ions were allowed to move freely. The energies obtained from all bulk calculations are shown in Tables 4.1, 4.2 and 4.3.

From the tables it can be seen that in all three cases a k-point mesh of $4 \times 4 \times 4$ with a high energy cutoff was sufficient to reach a convergence of 3 decimal places. In future calculations presented in this thesis the bulk energy has been taken from the $6 \times 6 \times 6$, high cutoff calculations.

k-points	Energy cutoff	Total energy (eV)
$3 \times 3 \times 3$	high	-82.714259
$4 \times 4 \times 4$	medium	-82.718323
$4 \times 4 \times 4$	high	-82.718895
$5 \times 5 \times 5$	high	-82.719016
$6 \times 6 \times 6$	high	-82.719141
$7 \times 7 \times 7$	high	-82.719146

Table 4.2: US-PP LDA bulk calcite convergence

k-points	Energy cutoff	Total energy (eV)
$3 \times 3 \times 3$	high	-75.274699
$4 \times 4 \times 4$	medium	-75.28052
$4 \times 4 \times 4$	high	-75.279099
$5 \times 5 \times 5$	high	-75.279240
$6 \times 6 \times 6$	high	-75.279411
$7 \times 7 \times 7$	high	-75.279472

Table 4.3: PAW GGA bulk calcite convergence

Convergence of an isolated water molecule

The free energy of an isolated water molecule in vacuum was calculated. To calculate this energy all the atoms were allowed to move freely and the periodic cell size was set to $12 \times 12 \times 12$Å. This large cell size was chosen to ensure that there was no interaction between the molecules across the periodic boundary. The number of k-points was reduced to $1 \times 1 \times 1$, which also minimised interaction between molecules in neighbouring periodic cells. The energy of a water molecule was found to be -14.259952eV.

Convergence of a dry calcite surface

After minimum convergence criteria for bulk calcite had been established a dry, flat $\{10\bar{1}4\}$ calcite surface slab could be considered. As in the case of the bulk three types of calculation were performed; GGA US-PP, LDA US-PP and PAW GGA. The periodic cell used in the calculations is shown in Figure 4.2. This cell had lattice vectors (given in Å):
$a_1 = 18.0\hat{x}$

$a_2 = 9.9792\hat{y}$
$a_3 = 8.0954789778\hat{z}$
and contained 12 $CaCO_3$ units in three layers, corresponding to a cell with four surface Ca and four surface CO_3 ions. This will be refered to as cell A. When four layers were simulated, a_1 was increased to $a_1 = 21.0335$Å and the cell contained 16 $CaCO_3$ units (the surface layer still consisted of four surface Ca and four surface CO_3 ions). This will be refered to as cell A_b. Note that the surface direction is along the x-axis.

As in the case of the bulk, the number of k-points and the energy cutoff were altered when investigating convergence. In addition, the number of calcite layers in the surface slab were also altered to determine how many would be required to achieve accurate results. The termination of the bulk crystal at the surface will have an effect on the layers immediately below, how far into the bulk crystal this effect perpetuates depends on the mineral. Convergence tests on the number of calcite layers in the periodic cell are therefore necessary to ensure a reasonable representation of the surface is used in future calculations. All the ions in the calcite slab were allowed to move. The results of the convergence tests are shown in Tables 4.4 and 4.5.

When considering the surface cell a new parameter can be introduced to measure convergence, namely the surface energy. This is the energy (per unit area) required to create a surface by cleaving a bulk crystal. It can therefore be calculated using the following equation:

$$\gamma_{dry} = \frac{U_S - U_B}{A} \tag{4.1}$$

where γ_{dry} = dry surface energy, U_S = energy of dry surface slab, U_B = energy of the bulk crystal (with the same number of unit cells as used to model the surface) and A = surface area.

The size of the vacuum slab was 10.4Å during all the convergence tests. To check this was sufficient two calculations were run with GGA US-PP with k-points of $1 \times 2 \times 2$ and a high energy cutoff in which the size of the vacuum was increased. The surface energies for calculations run with a vacuum slab of 12.4Å and 14.4Å were 0.449841Jm^{-2} and 0.449774Jm^{-2} respectively (the surface energy was 0.453494Jm^{-2} at 10.4Å). This indicates that the surface energy at 10.4Å was converged to two decimal places and therefore sufficient for future calculations.

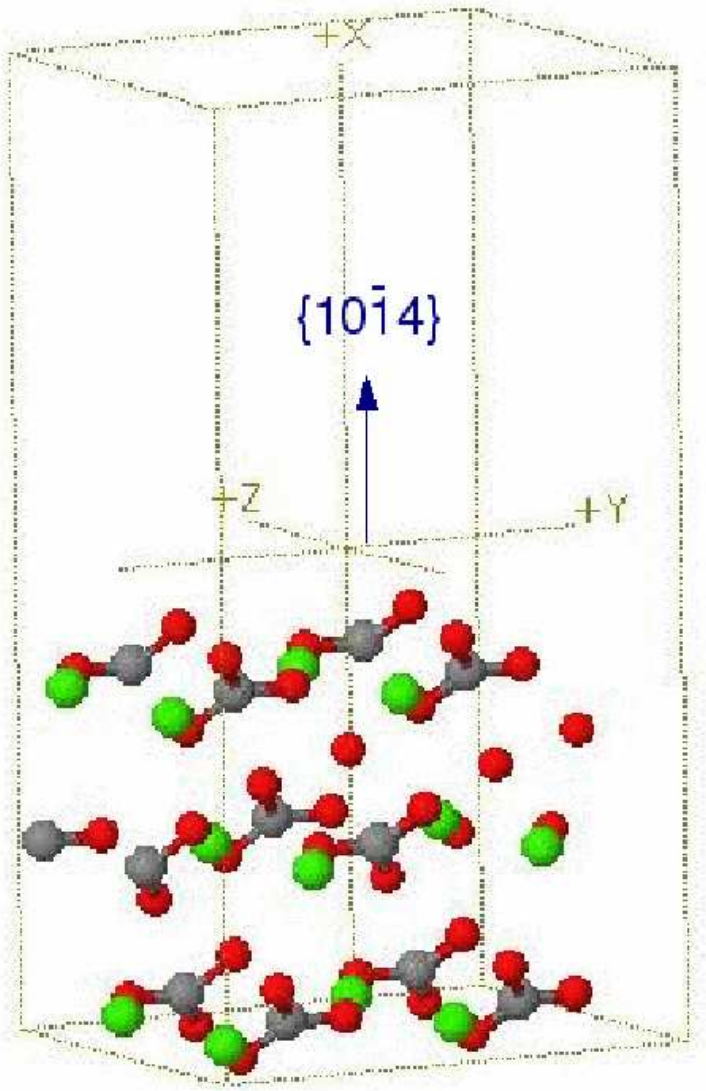

Figure 4.2: Periodic cell with 3 layers of calcite. The direction of the $\{10\bar{1}4\}$ surface is indicated by the blue arrow. Note that the surface direction is along the x-axis.

Calculation type	k-points	Energy cutoff	Total energy (eV)	Surface energy (Jm^{-2})
GGA US-PP	$1 \times 2 \times 2$	medium	-448.600427	0.453494
GGA US-PP	$1 \times 3 \times 3$	medium	-448.598855	0.453650
GGA US-PP	$1 \times 4 \times 4$	medium	-448.596597	0.453876
GGA US-PP	$1 \times 2 \times 2$	high	–448.639925	0.453494
GGA US-PP	$1 \times 3 \times 3$	high	-448.641568	0.449415
GGA US-PP	$1 \times 4 \times 4$	high	-448.641766	0.449395
LDA US-PP	$1 \times 2 \times 2$	medium	-490.751284	0.551629
LDA US-PP	$1 \times 3 \times 3$	medium	-490.753131	0.551446
LDA US-PP	$1 \times 4 \times 4$	medium	-490.746983	0.552056
LDA US-PP	$1 \times 2 \times 2$	high	-490.700987	0.556616
LDA US-PP	$1 \times 3 \times 3$	high	-490.718711	0.554859
LDA US-PP	$1 \times 4 \times 4$	high	-490.715724	0.555155
PAW GGA	$1 \times 2 \times 2$	medium	-447.477617	0.416317
PAW GGA	$1 \times 3 \times 3$	medium	-447.480718	0.416004
PAW GGA	$1 \times 4 \times 4$	medium	-447.482548	0.415828
PAW GGA	$1 \times 2 \times 2$	high	-447.474614	0.416615
PAW GGA	$1 \times 3 \times 3$	high	-447.47334	0.416741
PAW GGA	$1 \times 4 \times 4$	high	-447.475481	0.416529

Table 4.4: Convergence tests on a 3 layer calcite surface slab (Cell A).

Calculation type	k-points	Energy cutoff	Total energy (eV)	Surface energy (Jm^{-2})
GGA US-PP	$1 \times 2 \times 2$	medium	-599.745657	0.444853
GGA US-PP	$1 \times 2 \times 2$	high	-599.746811	0.444738
LDA US-PP	$1 \times 2 \times 2$	medium	-656.574466	0.513466
LDA US-PP	$1 \times 2 \times 2$	high	-656.56035	0.514866
PAW GGA	$1 \times 2 \times 2$	medium	-598.108401	0.409182279
PAW GGA	$1 \times 2 \times 2$	high	-598.100585	0.409957238

Table 4.5: Convergence tests on a 4 layer calcite surface slab.

From Table 4.4 it can be seen that in the case of GGA US-PP, convergence of the surface energy to two decimal places (the desired accuracy) occurs with a k-point mesh as low as $1 \times 2 \times 2$, using a high energy cutoff, in the 3 layer cell. LDA US-PP and PAW GGA also present good convergence with a $1 \times 2 \times 2$ k-point mesh. A lower energy cutoff is also sufficient as there is virtually no difference between high and low cutoffs with these techniques. However, when these results are compared with those found using 4 calcite layers it can be seen that they do not agree quite so closely. The addition of a fourth layers appears to increase the accuracy of calculations, particularly those using LDA.

From the tables it can be noted that the number of k-points necessary for these calculations was less than in the case of bulk calcite. This was to be expected because, as explained in Section 3.1.6, when the supercell becomes larger, the size of the Brillouin zone shrinks and fewer k-points need to be sampled to build an accurate picture of the electronic states.

Experimental values for the surface energy of calcite range from 0.3Jm^{-2} [71] to 0.7Jm^{-2} [72]. The values calculated using VASP fall within this experimental range, indicating they are reasonable. Previous theoretical values for the surface energy also correspond with the value obtained by these VASP calculations. A value of 0.59Jm^{-2} [6] was found using classical calculations and 0.43Jm^{-2} [9] was obtained with ab-initio calculations. If the different types of calculation are compared, it is clear that LDA produces a higher surface energy than either GGA or PAW. This is not unusual, and it has previously been suggested that LDA produces better agreement with experimental surface energies [73].

For future calculations it was decided that 3 layers of calcite would be sufficient, as the surface energy with this cell was well converged and while 4 layers would further increase the accuracy, it was decided that the extra computing time involved was not justified when good results could be expected using 3 layers. Similarly, it was decided that a k-point mesh of $1 \times 2 \times 2$ would be sufficient for future calculations as a resonable accuracy could be obtained with this mesh. The plane wave cutoff was set to high, corresponding to a value of 515eV for these calculations. GGA US-PP was chosen for all future calculations as initial investigations into water adsorption energies using LDA US-PP produced large positive values, which were clearly inaccurate. As a result GGA US-PP calculations were employed exclusively

from this point onwards.

4.3 Static relaxations of the calcite-water interface

25% water coverage on the calcite {10$\bar{1}$4} surface

Static relaxations of a single H_2O molecule on a three layer calcite slab were performed. The whole periodic cell contained 12 Ca and 12 CO_3 ions and the surface layer contained 4 Ca and 4 CO_3 ions. The cell measured $18.0 \times 9.98 \times 8.10$Å (cell A). As the cell contained one H_2O, the calculation as a whole had one H_2O per 4 Ca ions or 25% water coverage.

Coverage is defined as the ratio of the number of water molecules to the number of surface Ca ions and the coverage is varied by varying the size of the periodic cell. This imposes additional symmetry for small unit cells, and so it is not strictly equivalent to the experimental definition of coverage, however it gives an efficient method for investigating the interactions between water molecules.

A variety of positions for the H_2O were tested to find the lowest energy configuration. The initial ion positions in the calcite crystal were taken from the relaxed state found during the surface convergence. The ions in the bottom layer of calcite in the cell were not allowed to move to simulate their contact with the bulk in a real crystal. A k-point mesh of $1 \times 2 \times 2$ was used in all calculations.

Three H_2O positions were investigated, the relaxed structures are shown in Figures 4.3, 4.4 and 4.5. In the starting configuration, the O_{water} was always placed above a surface Ca ion, while the hydrogens were orientated so that they pointed towards $O_{carbonate}$ ions.

In the first two calculations the hydrogens were pointed towards CO_3 ions from the same CO_3 row. The difference in the two configurations comes from the different orientation of the CO_3 ions in alternate rows. In the third calculation the hydrogens were orientated towards CO_3 ions in different rows.

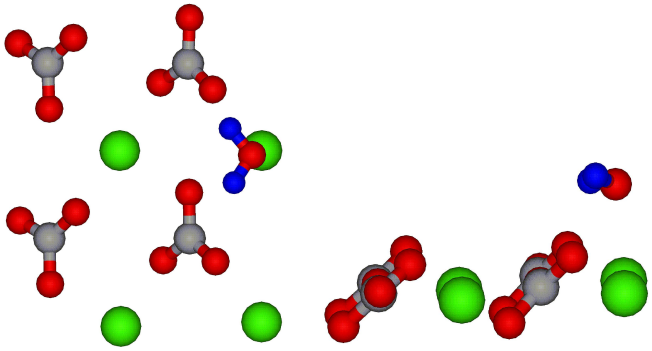

(a) (b)

Figure 4.3: Configuration of *Position 1* after relaxation. (a) Top view. (b) Side view. Only the top layer of the simulation is shown for clarity - this convention will be followed in most images presented in this thesis.

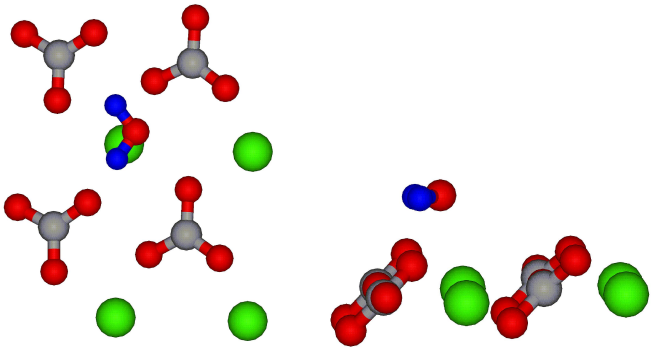

(a) (b)

Figure 4.4: Configuration of *Position 2* after relaxation. (a) Top view. (b) Side view.

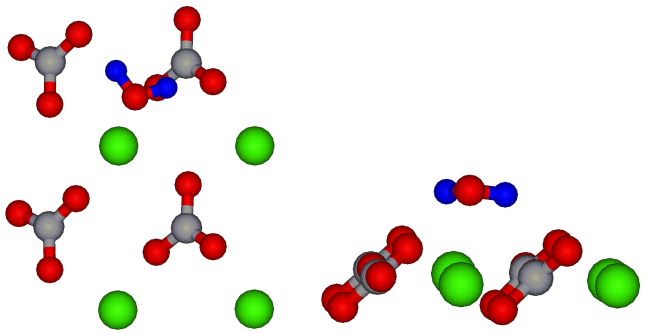

(a) (b)

Figure 4.5: Configuration of *Position 3* after relaxation. (a) Top view. (b) Side view.

In order to establish the most energetically favourable state the water adsorption energy and the wet surface energy were calculated. The water adsorption energy, U_{ad}, was defined as the energy gain per molecule when n isolated molecules are adsorbed on the surface. The water adsorption energies were calculated using the following equation:

$$U_{ad} = (U_{Hyd} - (U_S + nU_{H_2O}))/n \tag{4.2}$$

where U_{ad} = water adsorption energy, U_{Hyd} = energy of hydrated surface slab, U_S = energy of dry surface slab, n = number of water molecules and U_{H_2O} = energy of an isolated water molecule.

Adsorbing water on the surface effectively reduces the energy required to cleave the crystal and therefore a wet surface energy (following Kerisit et al [9]) can be defined as:

$$\gamma_{wet} = \frac{nU_{ad}}{A} + \gamma_{dry} \tag{4.3}$$

which can also be written:

$$\gamma_{wet} = \frac{U_{Hyd} - (U_B + nU_{H_2O})}{A} \tag{4.4}$$

where γ_{dry} is defined as in equation 4.1.

	Position 1	*Position 2*	*Position 3*
Water adsorption energy (eV)	-0.629	-0.636	-0.909
Surface energy (Jm^{-2})	0.387	0.386	0.359
Ca-O_{water} bond length (Å)	2.41	2.43	2.39
H_1-$O_{carbonate}$ bond length (Å)	2.13	2.63	1.97
H_2-$O_{carbonate}$ bond length (Å)	2.99	2.07	2.20

Table 4.6: Adsorption and wet surface energies, Ca-O_{water} bond length and H-$O_{carbonate}$ bond length for the different water positions investigated.

The adsorption and wet surface energies, along with the Ca-O_{water} and H-$O_{carbonate}$ bond lengths, for all three water molecule positions are presented in Table 4.6. By comparing the values for the different positions it can be seen that there is little difference between Position 1 and Position 2 in terms of which is energetically preferred. However, Position 3 gives substantially lower surface energy and adsorption energy, indicating that this is the most favoured position. From these results we can conclude that there is little difference between the two inequivalent CO_3 orientations. The lowest energy configuration was when the H_2O was stradled across two CO_3 rows, rather than pointing directly towards one row.

To ensure the cell used in these calculations was large enough to remove water-water interactions across the periodic boundaries, a calculation was performed with one H_2O in a larger cell, cell B. This cell had dimensions $9.98 \times 16.19 \times 18.0$Å, and when one H_2O was in the cell the coverage was 12.5%. The adsorption energy differed by less than 10^{-2}eV, indicating that the water-water interactions are minimal in the small cell and that these calculations are reliable.

The difference in energy found at the different positions can be explained by the different bonds formed by the H_2O molecule with the surface. The low energy position, *Position 3* has a shorter Ca-O_{water} distance of 2.39Å, compared to 2.41Å for *Position 1* and 2.43Å for *Position 2*. The bonds between the hydrogens and $O_{carbonate}$ atoms were 1.97Å and 2.20Å in the low energy *Position 3*, 2.13Å and 2.99Å in *Position 1* and 2.07Å and 2.63Å in *Position 2*.

As experimental evidence indicates that water dissociates on the calcite surface [10], a static relaxation in which the water molecule was initially dissociated was performed. The simulation was initialised with the OH placed 2.2Å above a surface Ca ion and an H placed 1.5Å away from a surface $O_{carbonate}$, forming a surface HCO_3

ion. The configuration of the water ions at the start and end of the calculation are shown in Figure 4.6. The water ions re-associated during the calculation to form a single molecule, indicating that dissociated water is not stable on the $\{10\bar{1}4\}$ surface at 25% coverage. Kerisit et al found the same effect for higher (100%) coverage [9]. However, this does not give an indication of the energy penalty incurred by dissociating water. In order to calculate this energy penalty a metastable state must be located, with this in mind other percentage water coverages were investigated.

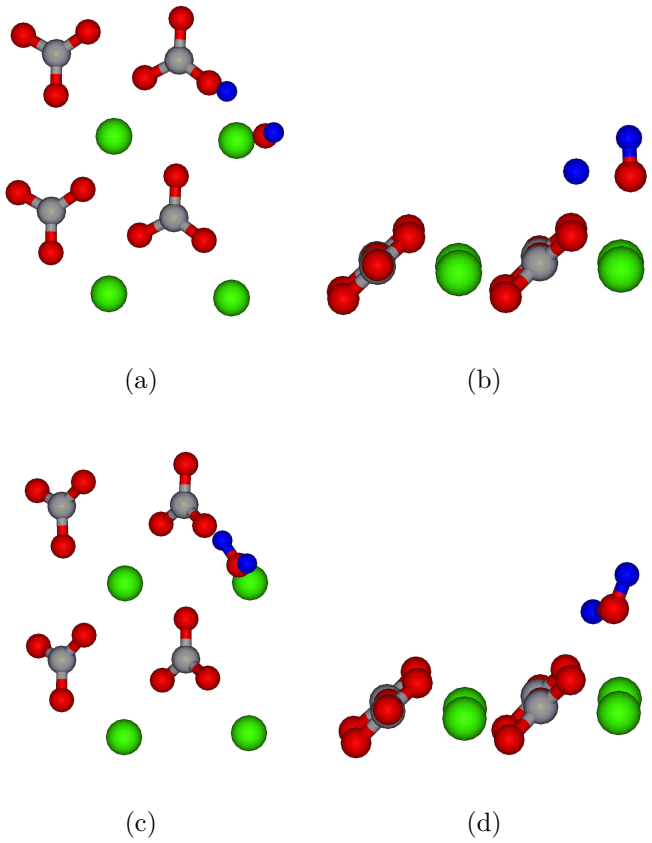

Figure 4.6: (a) + (b) Configuration of water ions at the start of the calculation. (a) Top view. (b) Side view. (c) + (d) Water ions configuration after relaxation. (c) Top view. (d) Side view.

12.5% water coverage on the calcite $\{10\bar{1}4\}$ surface

The first new coverage to be investigated was a lower coverge of 12.5%. This allowed the dissociated water ions to be moved further apart within the periodic cell,

preventing them from reassociating during the relaxation. The periodic unit cell was doubled along the z axis, making the cell twice as long as before, measuring $18.0 \times 9.98 \times 16.2$Å with 8 Ca and 8 CO_3 ions on the surface (cell B). One H_2O was put in this cell, which gave a coverage of 12.5% with one H_2O per 8 Ca ions.

Initially it was very difficult to find positions for the dissociated ions that did not result in a complete failure of the calculation. A local minima was difficult to locate and self-consistency cycles did not converge. The ions in the calculation tended to be rearranged in unnatural patterns and the crystal was often seen to 'fall apart' (the ions moved away from each other to occupy random parts of the periodic cell and no longer represented any crystal structure).

This problem was resolved by performing two individual calculations in the original, smaller, periodic cell (cell A). In one calculation a hydrogen ion was positioned next to a CO_3 ion, and in the other an OH was placed above a surface Ca ion. This allowed the H^+ and OH^- to move to low energy positions within smaller calculations in which the other ion could not influence it, the final configurations of the two calculations were then combined in a larger calculation in cell B. At the beginning of this calculation the dissociated water ions were 7Å apart, the OH was 2.47Å above a surface Ca ion and the H was 1.09Å away from an $O_{carbonate}$ ion.

This configuration did converge and the final configuration can be seen in Figure 4.7. After relaxation the OH-H distance was $\sim$ 6Å and the H-$O_{carbonate}$ distance was 0.98Å. The most significant movement during the relaxation of the ions was of the OH, which moved from almost directly above the Ca towards the HCO_3 ion, ending the calculation between two surface Ca ions at distances of 2.25Å and 2.34Å (distances at the start of the calculation were 2.47Å and 3.97Å).

The energy of this configuration was -910.70eV. In order to establish whether this is energetically favourable, it must be compared with an associated H_2O in the same cell. Therefore a calculation with an associated H_2O in cell B was performed. This configuration gave an energy of -912.47eV, making the dissociated configuration energy 1.77eV higher than associated water. This implies that dissociated water is strongly energetically unfavourable on a $\{10\bar{1}4\}$ calcite surface and that the stable dissociated state found is a metastable state. The relaxed associated configuration is shown in Figure 4.8. The electron charge distribution of both associated and

dissociated configurations is shown in Figure 4.9[1]. Figure 4.9(a) indicates that the electron charge from the hydrogen forming the HCO_3 ion largely transfers to the CO_3 ion when the bicarbonate is formed. The electron charge on the OH^- ion, however, remains more evenly distributed.

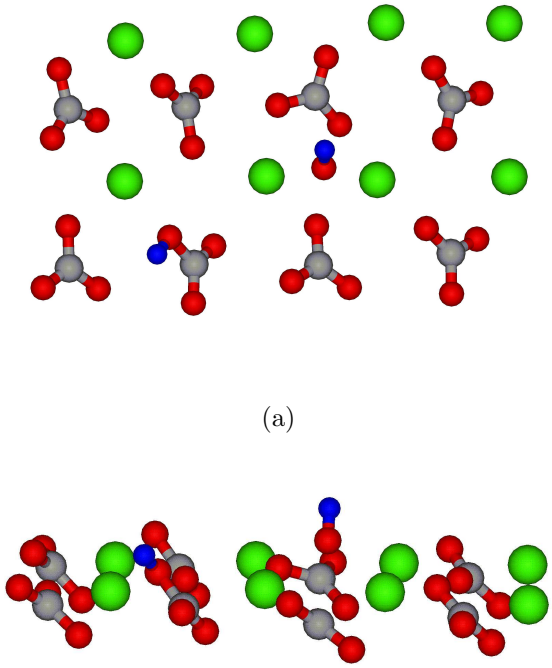

(a)

(b)

Figure 4.7: Metastable dissociated state. (a) Top view. (b) Side view.

A comparison of adsorption and surface energies of the associated and dissociated calculations are shown in Table 4.7. These energies support the conclusion that the dissociated state is energetically unfavourable. The surface energy is higher for the dissociated state than the associated state and the H_2O adsorption energy is above zero for the dissociated state, indicating it is strongly unfavourable.

[1]This distribution was produced using the OpenDX software, with the isosurface value set to 0.4.

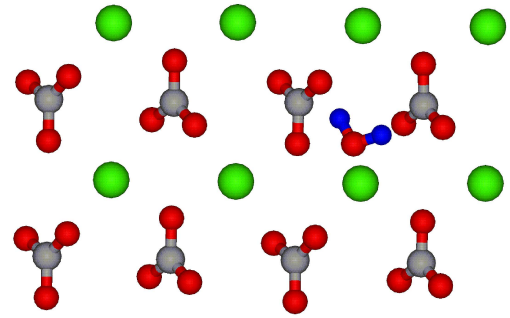

(a)

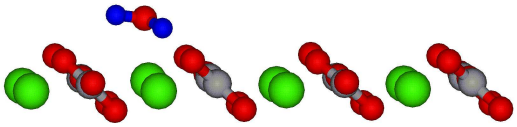

(b)

Figure 4.8: Associated water state in cell B. (a) Top view. (b) Side view.

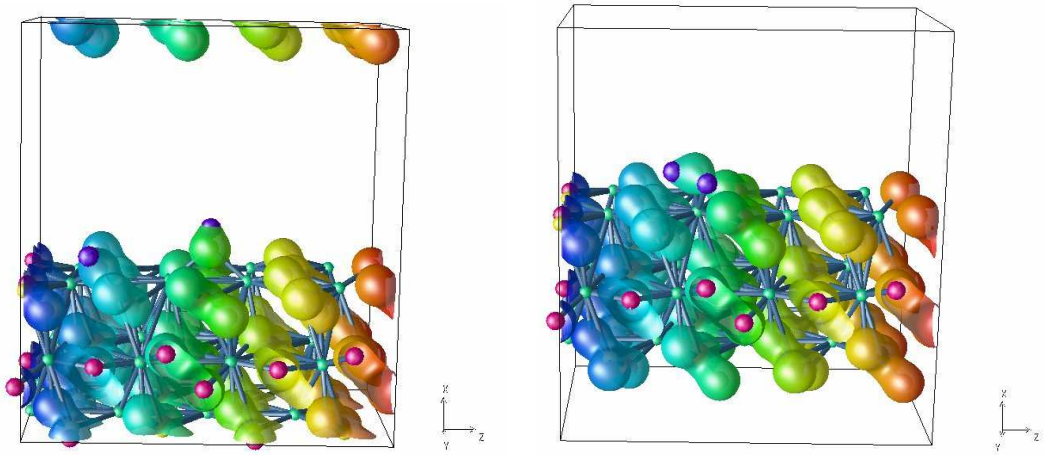

(a) (b)

Figure 4.9: The electron charge density in the final configuration for (a) the metastable dissociated state and (b) the associated state. NB The colouring represents the position of the atoms in respect to the z-axis.

Calculation	Total energy (eV)	H_2O Adsorption energy (eV)	Surface energy (Jm^{-2})
Metastable dissociated	-910.70eV	+0.86	0.49
Low energy associated	-912.47eV	-0.92	0.40

Table 4.7: Comparison of adsorption and surface energies of metastable dissociated and low energy associated states.

33% water coverage on the calcite {10$\bar{1}$4} surface

As the metastable state at 12.5% coverage would not be expected to occur in nature, two H_2O molecules on the surface were considered as it has previously been shown that a second H_2O can stabilise dissociation through H-bonding on MgO surfaces [74]. It is therefore natural to consider whether a mixed state of one dissociated and one associated H_2O can also stabilise dissociation on calcite.

Several positions of H_2O molecules were tested in a periodic cell with 6 Ca and 6 CO_3 ions in the surface, referred to as cell C, and measuring $18.0 \times 9.98 \times 12.14$Å. There were two H_2O molecules in each periodic cell, creating a water coverage of 33%. Three configurations were tested and are shown in Figures 4.10, 4.12 and 4.14. In the first simulation, both molecules were dissociated, in the second, one molecule was dissociated and the other associated and in the third simulation both molecules were associated. The adsorption and surface energies for the three calculations are shown in Table 4.8

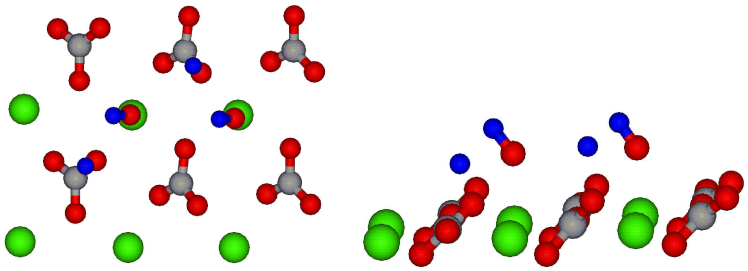

(a) (b)

Figure 4.10: The starting configuration of calculation with two dissociated water molecules. (a) Top view. (b) Side view.

During the first relaxation, in which both water molecules were dissociated, the water

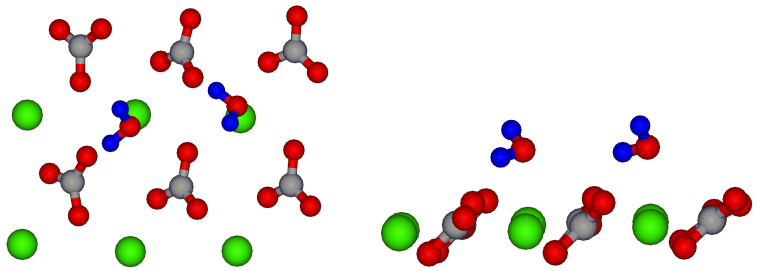

(a) (b)

Figure 4.11: The final configuration of a calculation in which the two water molecules were initially dissociated. The dissociated species recombined during the relaxation. (a) Top view. (b) Side view.

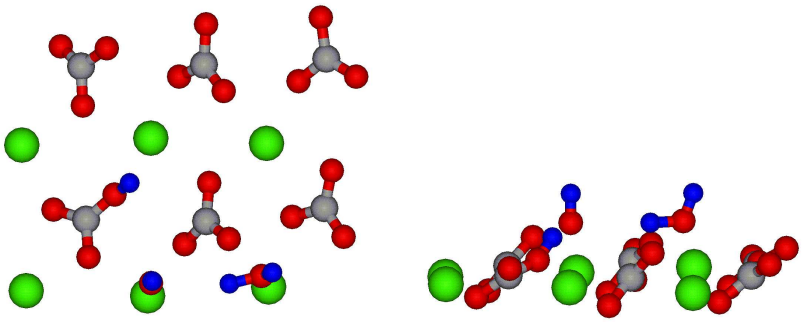

(a) (b)

Figure 4.12: The starting configuration of calculation with one associated and one dissociated water molecule. (a) Top view. (b) Side view.

Calculation	Total energy (eV)	Adsorption energy/H_2O (eV)	Surface energy (Jm^{-2})
Initially two dissociated molecules	-702.116750	-0.6349	0.40747
Initially one associated and one dissociated molecule	-702.255364	-0.7042	0.3983
Initially two associated molecules	-702.611292	-0.8822	0.3748

Table 4.8: Comparison of energies from calculations at 33% coverage.

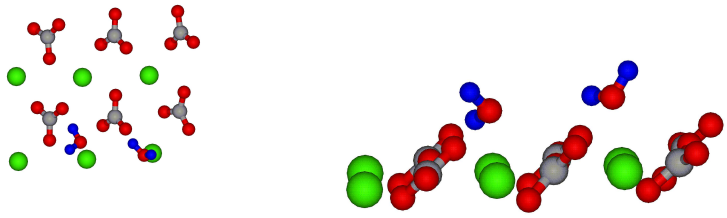

(a) (b)

Figure 4.13: The final configuration of a calculation that was started with one associated and one dissociated water molecule. The dissociated molecule recombined to form an associated molecule during the relaxation. (a) Top view. (b) Side view.

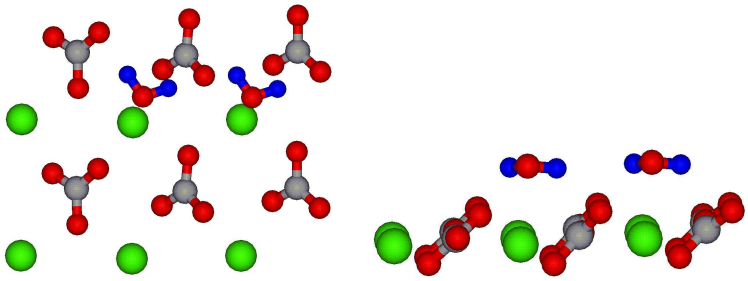

(a) (b)

Figure 4.14: The starting configuration of a calculation with two associated water molecules. (a) Top view. (b) Side view.

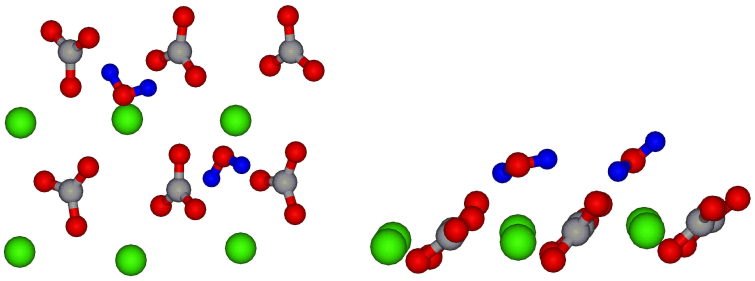

(a) (b)

Figure 4.15: The final configuration of a calculation started from a configuration taken from the end of an MD run with two associated water molecules. (a) Top view. (b) Side view.

recombined to form two associated H_2O molecules. The final configuration is shown in Figure 4.11. Similarly, in the second calculation the dissociated water molecule recombined and the final configuration consisted of two associated water molecules, as pictured in Figure 4.13. This suggests that a second, associated molecule, does not stabilise dissociation on the calcite {10$\bar{1}$4} surface.

Initially, in the calculation with two associated H_2O molecules, the molecules were placed in the low energy position found at 25% coverage, shown in Figure 4.14. However, this caused the crystal to become disorganised and break apart. Therefore a short MD simulation[2] was run to allow the molecules to find a lower energy position from which a static relaxation could be initiated. The MD simulation revealed that the prefered orientation of the molecules was for them to sit 'facing each other'. The final configuration of the MD simulation was used as the starting configurtion for a static relaxation, the results of which are shown in Figure 4.15. Surface and adsorption energies of the simulations are shown in Table 4.8.

These simulations did not find a stable form of dissociated water on calcite and they suggest that a second H_2O does not stabilise the dissociation of water, as it does on some oxide surfaces such as MgO. The most stable configuration found at 33% coverage was that found by MD simulation in which the water molecules lie flat, in alternate directions, on the surface.

100% water coverage on the calcite {10$\bar{1}$4} surface

A full monolayer of water was considered in cell A, with one H_2O per surface Ca - 100% coverage. As Kerisit et al showed that dissociation at this coverage is unfavourable [9] only associated water was considered. To investigate this coverage an MD simulation was first performed, as in the case of the two associated water molecules at 33% coverage. The MD found a zig-zag pattern and the final configuration of this MD simulation was relaxed to obtain adsorption and surface energies. The final relaxed configuration is shown in Figure 4.16. The same pattern was previously observed by de Leeuw and Parker using atomistic simulation techniques [6].

[2]MD simulations in VASP will be discussed in more detail in Chapter 5 and technical details of this MD, and others discussed in this Chapter, can be found there.

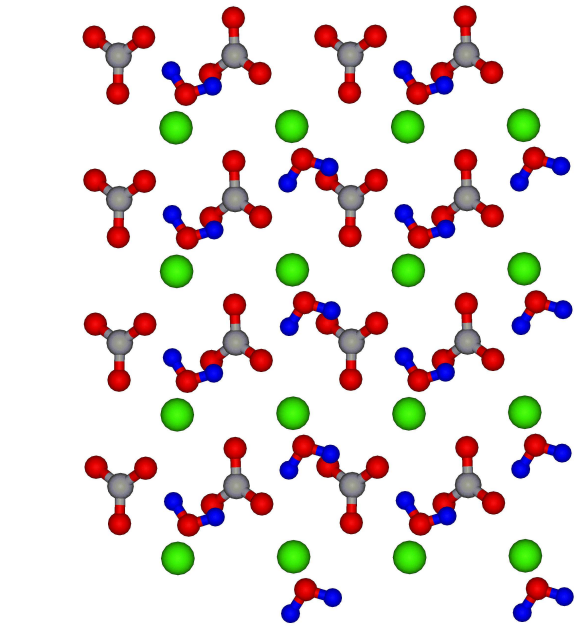

(a)

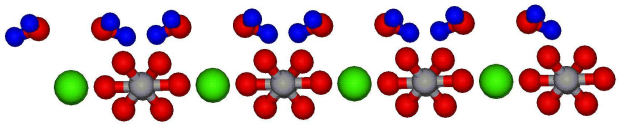

(b)

Figure 4.16: 100% coverage of water on {10$\bar{1}$4} calcite surface. Several unit cells are shown for clarity. (a) Top view. (b) Side view.

The adsorption energy per H_2O of the relaxed structure was -0.914eV and the surface energy was 0.09Jm^{-1}. The adsorption energy is very close to that of previous coverages and the surface energy follows the trend of becoming lower as more water is added.

200% water coverage on the calcite {10$\bar{1}$4} surface

A second layer of water was added above the monolayer, so that there were two H_2O molecules per surface Ca ion, or 200% coverage. An MD simulation was performed before the final configuration from the MD was relaxed. The ion structure after relaxation is shown in Figure 4.17. The introduction of a second water layer disrupted the zig-zag pattern seen at 100% coverage, although the lower layer still lay relatively flat on the surface.

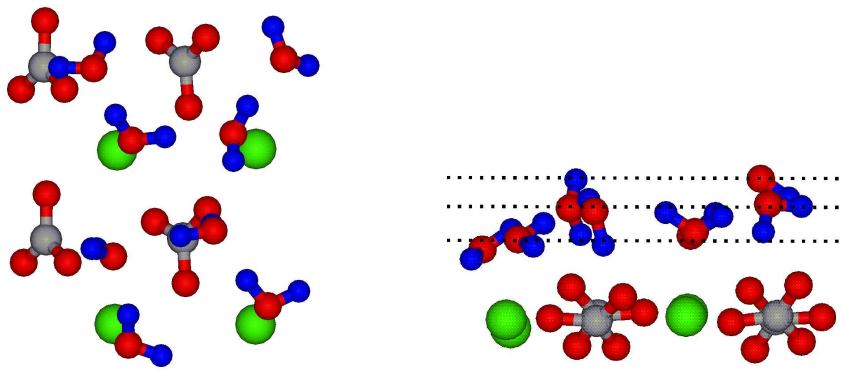

(a) (b)

Figure 4.17: 200% coverage of water on {10$\bar{1}$4} calcite surface. (a) Top view. (b) Side view - the dashed lines indicate O_{water} layers observed during the calculation, more details will be given in Section 5.4.

The magnitude of the adsorption energy per H_2O was lower at this coverage compared to previous calculations at -0.74eV, showing the water was less strongly bound to the surface on average. However the surface energy dropped again to -0.13Jm^{-2}. The negative surface energy implies that more energy is gained from the interaction of the H_2O and the surface than is lost by creating the surface. While the H_2O molecules formed some hydrogen bonds during the simulation, there was no indication this would stabilise dissociation.

4.4 Summary

Calculations at a series of water coverages reveal that water is strongly bound to the calcite $\{10\bar{1}4\}$ surface. All coverages up to 100% had similar H_2O adsorption energies, as shown in Table 4.9. The surface energy was seen to decrease as more water was added to the surface, implying water has a stabilising effect. At 200% coverage the negative surface energy suggests more energy is gained from the interaction of the surface with the H_2O than is lost by creating it.

These findings are largely consistent with previous work. De Leeuw and Parker found that the surface energy decreased as more water was added to the surface, from $0.56 Jm^{-2}$ at 12.5% coverage to $0.3 Jm^{-2}$ at 100% coverage [8, 6] and that the adsorption energy was -79.1kJmol^{-1} (-0.82eV) at both 12.5% and 100%. While the hydrated surface energies presented here are slightly lower, suggesting stronger bonding and a more stable hydrated surface, the general trend is the same. Wright et al. performed classical calculations at 100% coverage, using a different potential from that of de Leeuw and Parker. They found a lower surface energy of $0.23 Jm^{-2}$ and less stongly bound water, with an adsorption energy of -53.9kJmol^{-1} (-0.56eV) per molecule [39]. In the calculations presented here, the Ca-O_{water} distance was found to be 2.37Å (on average) in the monolayer. De Leeuw and Parker found a Ca-O_{water} distance of 2.4Å [8, 6] and Wright et al. found a distance of 2.55Å [39]. A comparison between the classical and ab-initio simulations shows that the latter generally have shorter Ca-O_{water} distances and stronger binding.

A metastable dissociated water state was found at 12.5% coverage, although this state is 1.77eV higher in energy than an equivalent associated water state implying it would not occur in nature. No evidence of stable dissociation was found at any of the other coverages, which points towards the conclusion that water dissociation does not occur on the perfect $\{10\bar{1}4\}$ surface. However, further investigation is necessary as experimental evidence indicates water does dissociate on the surface. Molecular dynamics simulations were therefore employed to explore more configuration space. These will be discussed in Chapter 5.

Coverage (%)	Adsorption energy/H_2O (eV)	Surface energy (Jm^{-2})
12.5	-0.91	0.40
25	-0.91	0.36
33	-0.88	0.37
100	-0.91	0.09
200	-0.74	-0.13

Table 4.9: Adsorption and surface energies for a range of hydration levels.

Chapter 5

Ab-initio molecular dynamics investigation of the calcite-water interface

As seen in Chapter 4, static relaxations failed to show any dissociation of water on the $\{10\bar{1}4\}$ calcite surface, therefore molecular dynamics (MD) simulations were used to explore more configuration space - these simulations will be discussed in this chapter. All the simulations presented here were performed using the smaller unit cell (A), which contains 12 Ca^{2+} ions and 12 CO_3^{2-} ions in 3 layers, with 4 of each ion in the surface layer.

5.1 Methods

Molecular dynamics using VASP

Some aspects of VASP have been considered in the previous chapter (see Section 4.1), however MD simulations require some extra calculation parameters and these are discussed in this section.

All MD simulations were run as gamma point calculations (ie $1\times1\times1$ k-points), with a lower energy cutoff than that used for the static relaxations of 297eV. The lower

cutoff was used in the MD calculations to reduce the computational time required for the simulations. As in the static relaxations, the vacuum between slabs was 10.4Å. The timestep, which defined how often the ion movement was calculated, was set to 1fs. The simulations were run in the constant temperature canonical ensemble, which was defined in Section 3.2. During the MD one ion was kept fixed (an oxygen in the middle of the calcite slab) and all other ions were allowed to move. Fixing one ion was designed to keep the crystal in one part of the cell and stop it wandering around, making visualisation easier.

Hydrogen's very light mass caused some initial problems in the simulations because the frequency of bond oscillation, given by $\sqrt{\frac{k}{m}}$ (where k is the spring constant and m is the mass), is very high. The oscillation of the hydrogen-oxygen bond is ∼1fs, which corresponds to the timestep of the MD and meant ions did not settle into position. To resolve this issue the mass of the hydrogen atoms was artificially increased from 1u to 8u, reducing their oscillation frequency, and increasing the time period of the H-O_{water} bond oscillation to $\sqrt{8}$fs. Taking this action did not affect the final energy or structural results, but the phonon and vibrational modes would be affected. In this work these properties were not required, so the change of mass was permissible. Increasing the mass means that the acceleration, a, of the atoms decreases (as $F = ma$ and the force, F, is fixed), so the speed of the dynamics is decreased, but the energy remains unaffected. Once the hydrogen mass had been increased the simulation ran without further difficulties. The mass remained at this setting for all VASP MD simulations.

5.1.1 DL_POLY

DL_POLY [75] is a classical simulation package capable of performing both static relaxations and molecular dynamics. There are two versions,
DL_POLY_2 and DL_POLY_3. For the work presented in this thesis
DL_POLY_2.16 was used, which is more efficient for simulating smaller numbers of atoms (<30,000 atoms). Three input files are required for DL_POLY, there are also three other optional input files. The first input file contains parameters such as the temperature and pressure (*CONTROL*), the second (*CONFIG*) contains the initial atom coordinates and lattice parameters and the third (*FIELD*) contains

information about the forcefield used in the calculation.

5.2 MD simulations at 25% water coverage

The static relaxations of water at 25% water coverage described in Section 4.3 indicated that the lowest energy position of a water molecule at this coverage was likely to be when it lay flat on the surface stradling two different CO_3 rows. MD simulations of this coverage allowed this to be tested, as the H_2O could explore more configuration space. Five simulations were run at 300K, 600K, 900K, 1200K and 1500K for 2.5ps each.

The simulations were all initiated with the H_2O placed in the lowest energy position found using static relaxations (*Position 3* in Section 4.3) and it remained at this orientation for the remainder of the simulation.

The H_2O did not diffuse or desorb at 300K, 600K or 900K. However, at 1200K and 1500K the H_2O was observed to diffuse across the surface to form a bond with a different surface Ca ion before desorbing after 1.28ps at 1200K and at 1.79ps at 1500K. Desorption was taken to have occurred when the O_{water} height above the surface had reached a point at which the H_2O would not return to the surface, this was at 4.4Å for 1200K and 4.6Å for 1500K (the surface was defined as the position of the Ca ions at the start of the simulation). The different height criteria for desorption at the two temperatures was due to the H_2O sitting higher on the surface as the temperature increased.

The simulation at 900K was extended to 8ps to investigate whether the H_2O would desorb from the surface during a longer time frame at this temperature. However, it remained on the surface and did not desorb or diffuse during the 8ps simulation. This can be evaluated in light of the desorption equation, $rate_{desorption} = -fexp(-\Delta E/k_B T)$, where f is a constant, ΔE is the energy required to desorb an H_2O molecule, k_B is Boltzmann's constant and T is the temperature. It is has been suggested that a reasonable value for f is 10^{-15} [76]. This equation leads to a desorption rate of $8.0\times10^{9}s^{-1}$ at 900K, or an expected desorption event every 125ps when using an adsorption energy of 0.91eV for ΔE (taken from that of *Position 3* in Section 4.3), longer than the time of the 8ps simulation, implying a desorption

event would not be expected during the simulation. At 1200K, the desorption rate rises to $1.5\times10^{11}\mathrm{s}^{-1}$, and a desorption event is expected, on average, every 6.7ps, so it is not unexpected that an H_2O would desorb during a 2.5ps simulation.

The H-O_{water} bond lengths of the H_2O were calculated at each timestep. The bond length fluctuated about a mean value of 0.99Å at 25% coverage at 300K over 2.5ps (in a static relaxation an H_2O in complete isolation has a bond length of 0.97Å). The standard deviation was calculated to give a measure of the bond fluctuations. It was found to be 0.04Å for the 300K simulation. At 600K and 900K the mean bond length was also found to be 0.99Å. However the standard deviation at 600K was 0.03Å and at 900K was 0.06Å, indicating the variation in bond length was greatest at the elevated temperature of 900K.

In Figure 5.1 the variation over time of the H-O_{water} bond closest to an $O_{carbonate}$ during the 300K, 600K and 900K simulations is shown. These graphs reveal that this bond fluctuates significantly during the simulations. From visualisation of the simulations it can be determined that this bond elongation was especially strong when the H was pointing directly towards a surface $O_{carbonate}$. Figure 5.2 shows the point at which the bond is longest during the 900K simulation. Note that in the visualisation an H is shown not bonded to either the O_{water} or $O_{carbonate}$. At this point the H-O_{water} distance was 1.30Å and the H-$O_{carbonate}$ distance was 1.36Å, thus the H atom is effectively shared between the H_2O and CO_3.

The distribution of H-$O_{carbonate}$ bond lengths was also calculated at each temperature. These graphs, shown in Figure 5.3 have been calculated by measuring the distance between each H-atom and every $O_{carbonate}$ atom in the simulation at each time step. The distribution has then been normalised. From the graph at 300K it is possible to see three peaks, corresponding to the three layers of the crystal. As the temperature increases, the distribution becomes less pronounced and the peaks start to merge. This indicates that the H_2O is moving up and down on the surface more at higher temperatures - producing a wider range of bond lengths. At 1200K and 1500K, there are separations larger than 10Å due to the desorption of the H_2O.

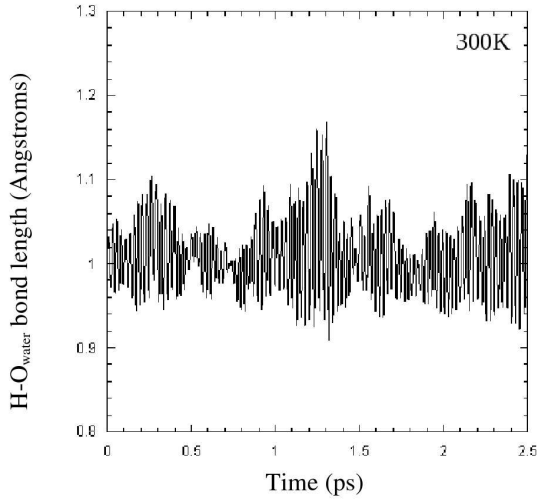

(a)

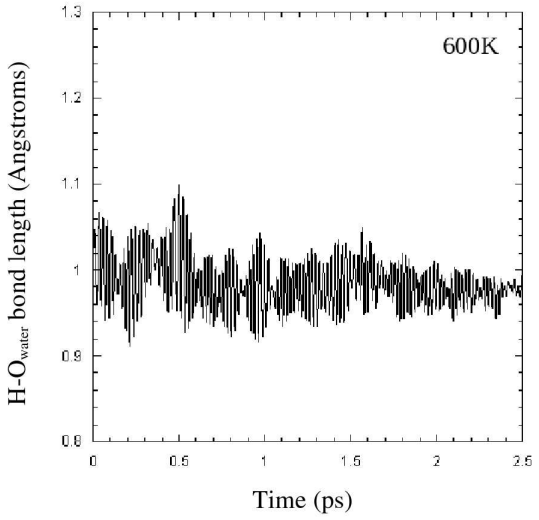

(b)

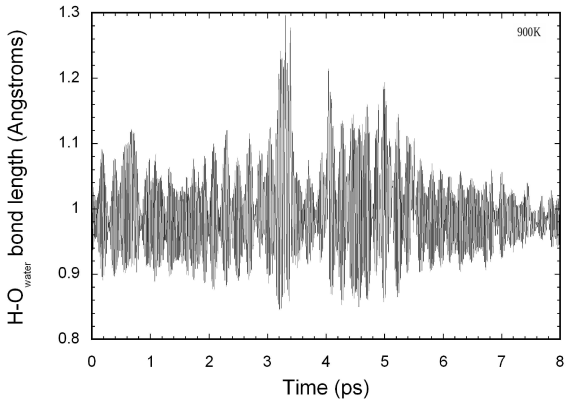

(c)

Figure 5.1: Graphs showing variation over time of the H-O$_{water}$ bond during MD simulations at (a) 300K (b) 600K and (c) 900K.

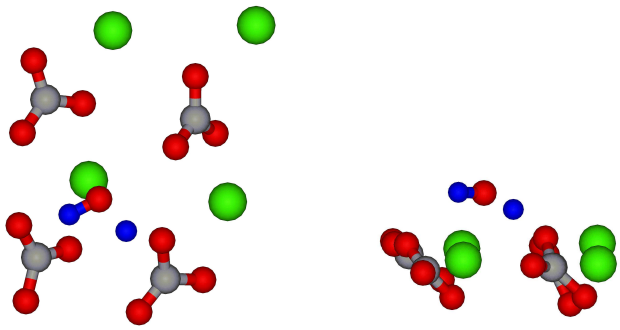

(a) (b)

Figure 5.2: Visualisation of the point at which the H-O_{water} bond is longest during the MD simulation at 900K. (a) Top view. (b) Side view.

Comparison between ab-initio and classical simulations

As explained in the Introduction (Chapter 1), the work in this thesis was undertaken as part of a collaboration. One of the primary aims of the collaboration is to develop new potential models for mineral-organic interfaces. The results of the ab-initio simulations presented here helped fulfill this aim by serving as a base point against which a new potential could be tested. To allow a comparison between the ab-inito results and those produced by classical potentials, the Ca-O_{water} separation was investigated in both types of calculation. The atomistic MD simulations were performed using the DL_POLY_2.16 code, three potentials were used, the Consortium potential (CP) [14], Lorentz-Berthelot mixing rules (LB) and the Kerisit-Parker (KP) potential [34] (more details about these potentials can be found in Section 3.3). A surface supercell, 2×3 times larger than cell A (used in the VASP simulations) was used for the atomistic MD, making the surface area six times as large. The same atomic positions and water coverage were used and the calcite slab thickness and vacuum size were kept the same as in the VASP simulations. The classical simulations were also run for 2.5ps with a 1fs timestep and snapshots of the configurations were taken every 0.1ps to enable statistical analysis.

To compare the different types of calculation, and the different potentials, the mean Ca-O_{water} separation was calculated for all the simulations. The final 1.8ps of the simulations were used to calculate the mean and only separations less than 3Å were

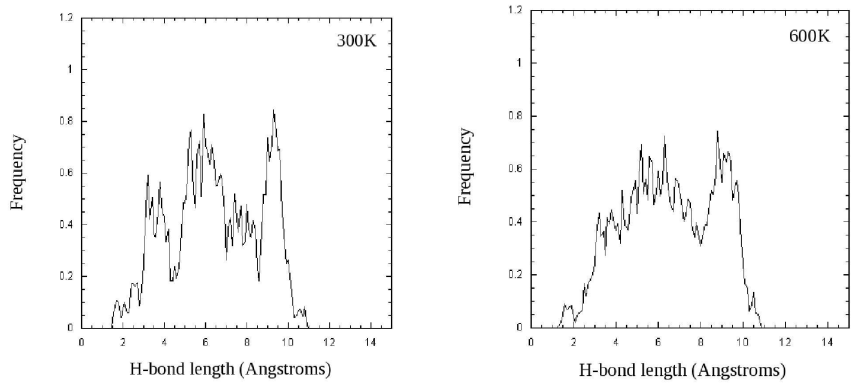

(a)

(b)

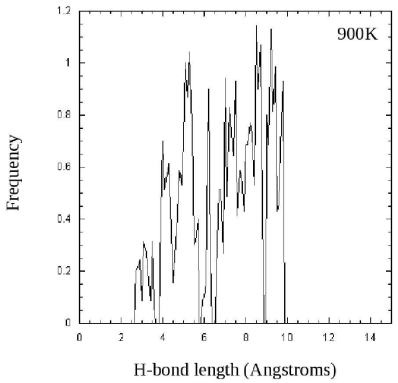

(c)

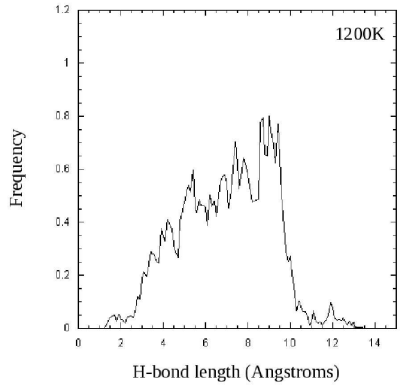

(d)

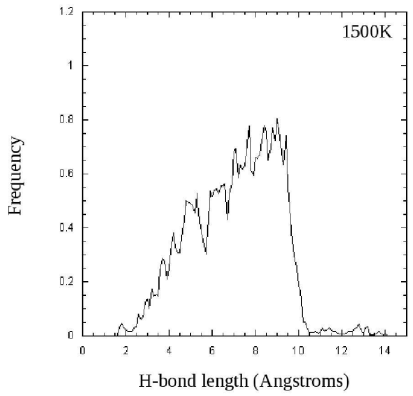

(e)

Figure 5.3: H-bond distribution at (a) 300K (b) 600K and (c) 900K (d) 1200K and (e) 1500K.

Temperature (K)	Separation (Å)				Fraction			
	VASP	CP	LB	KP	VASP	CP	LB	KP
300	2.41	2.49	2.23	2.34	1.0	0.99	1.0	1.0
600	2.43	2.54	2.27	2.40	1.0	0.65	1.0	0.99
900	2.46	2.58	2.29	2.51	1.0	0.39	0.87	0.39

Table 5.1: Mean Ca-O_{Water} separations for the final 1.8ps of classical and ab-initio simulations. CP=consortium potential, LB=Lorentz-Berthelot and KP=Kerisit and Parker potential. 'Fraction' represents the fraction of H_2O molecules within 3Å of the surface Ca ion. Larger separations are excluded from the calculation of the mean.

included to take account of the desorption observed in the atomistic simulations. The results of these calculations are shown in Table 5.1. The average separation was only calculated for the lower three temperatures investigated, as the higher temperatures could not be calculated reliably due to the H_2O desorbing within a short time span. The table shows the mean separations were slightly larger in the classical simulations using the CP potential compared with those found using VASP. The separations using the KP potential were smaller than VASP at 300K, but were very similar at 600K and 900K, while the LB potential gave much smaller separations at all temperatures.

The 'fraction' column in Table 5.1 represents the average fraction of H_2O molecules less than 3Å from the surface Ca ion. From this it is clear that at the higher temperatures a significant number of molecules have desorbed during the classical simulations, in contrast to the VASP simulations where desorption is not seen until 1200K. This suggests that in all of the classical potentials the binding is less strong than in the ab-initio simulations.

5.3 MD simulation at 100% water coverage

The MD simulations at 25% coverage showed the H_2O strongly bound to the surface at temperatures up to 900K and, while there was some elongation of the H-O_{water} bond during the simulations, no dissociation of the H_2O was observed. As it is known a H-bonding network can cause stablisation of dissociated species [74], MD simulations were extended to include 100% water coverage (one H_2O per surface Ca

ion).

The MD simulation at 100% coverage was performed at 300K for 3.5ps. The H_2O molecules were all initiated in the low energy position found using static relaxations (*Position 3* in Section 4.3), as shown in Figure 5.4, but within 1.9ps they had re-orientated themselves to form a very stable zig-zag pattern, shown in Figure 5.5. This pattern has previously been observed in classical MD simulations by de Leeuw and Parker [6]. GIXRD (grazing incidence x-ray diffraction) data taken by Magdans et al was later fitted to the surface model found by de Leeuw and Parker and found to be consistent with this surface water pattern [77]. The zig-zag stucture was relaxed in a static calculation. The final configuration was shown Chapter 4 in Figure 4.16.

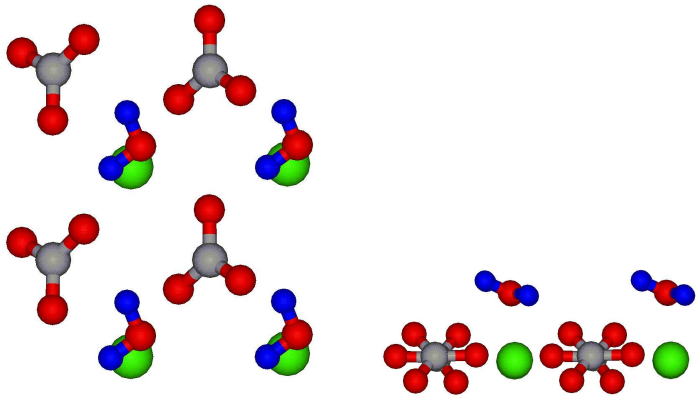

(a) (b)

Figure 5.4: Ion arrangement at the start of the 100% coverage simulation. (a) Top view. (b) Side view.

Analysis of the H-O_{water} bonds found they fluctuated about a mean value of 0.99Å (as at 25% coverage) with a standard deviation of 0.03Å over 2.5ps. This indicates the bond fluctuations were lower for 100% coverage than at 25% coverage at the same temperature.

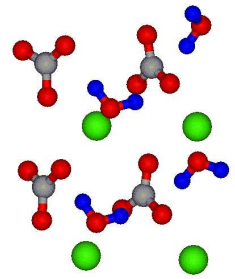

(a)

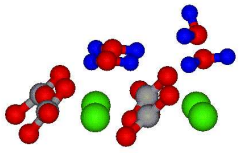

(b)

Figure 5.5: Final ion arrangement of MD simulation after 3.5ps at 100% water coverage. (a) Top view. (b) Side view.

5.4 MD simulations at 200% water coverage

Simulations were further extended to a water coverage of 200% (two H_2O molecules per surface Ca ion) in order to investigate what effect adding a second layer of water would have on the water structure at the surface.

The H_2O molecules were initialised so that a lower layer of four H_2O molecules lay flat on the surface. All these H_2O molecules were placed in the low energy position found at 25% coverage (see Section 4.3). A further four molecules were placed 4.6Å above the surface perpendicular to it with one H pointing down towards the surface, which allowed them to 'drop into' the lower water layer and allowed the water to easily rearrange itself. This inital arrangement is shown in Figure 5.6. (Simulations that were started with the upper four molecules nearer the surface gained too much energy and did not settle as the initial starting position was too far from a minima.) The simulation was then run at 300K for 5.7ps. The zig-zag pattern seen at 100% coverage did not reappear, the lower molecules generally lay flat on the surface, but no particular orientation was favoured by all four lower molecules. The upper four molecules moved towards the surface and remained generally perpendicular to it. The final configuration is shown in Figure 5.7.

A second MD simulation was run that was initialised with the lower four H_2O molecules lying flat on the surface in the low energy position found during the 100% MD simulation and subsequent static relaxation (see Sections 4.3 and 5.3). As with the first 200% MD simulation, the four upper H_2O molecules were initially placed 4.6Å above the surface and allowed to 'drop into' the established pattern. The zig-zag pattern found at 100% coverage was disrupted during the MD simulation and disappeared. The molecules showed no tendency towards establishing a new pattern and behaved in a very similar manner to the first simulation.

Further analysis of the first MD simulation was performed. The heights of the O_{water} ions were calculated at each time step and a histogram of the their height above the surface during the simulation is shown in Figure 5.8(a). The height was calculated by taking a fixed plane on the surface (chosen as the initial height of one surface Ca ion) and calculating the perpendicular distance of the O_{water} ions above this plane. The height was calculated at each timestep and the histogram represents the occurrence of the perpendicular O_{water} distances during the simulation. Figure

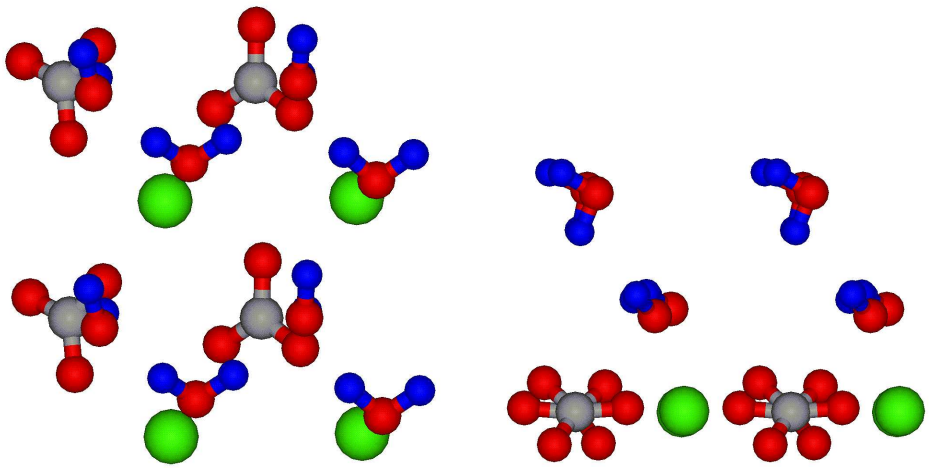

(a) (b)

Figure 5.6: Ion arrangement at the start of the 200% coverage simulation. (a) Top view. (b) Side view.

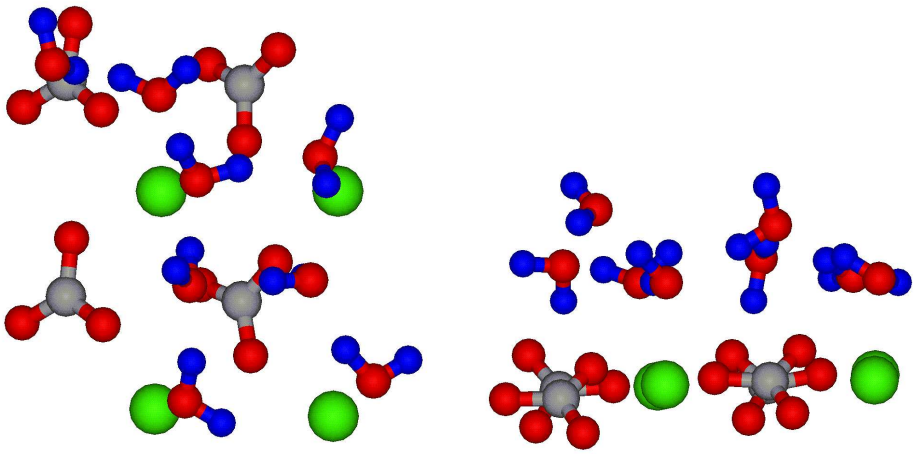

(a) (b)

Figure 5.7: Ion arrangement at the end of the 200% coverage simulation. (a) Top view. (b) Side view.

5.8(a) indicates that the presence of the second layer weakens binding to the surface of the first layer and increases separation. The second layer appears to have two peaks at 3.3Å and 4.5Å. One corresponds to H_2O bonded to surface ions and the other to H_2O bonded to the first layer of water. In the relaxed configuration shown in Figure 5.7 it is possible to see the lower layer of H_2O, at 2.7Å above the surface, and to see a splitting of the O_{water} positions in the upper layer, giving rise to the two higher peaks in the histogram. (An identical analysis was performed for the second MD simulation at 200% coverage. This produced a very similar histogram, indicating that the starting configuration did not have a large impact on the overall simulation.)

The histogram also shows the same data taken at 100% coverage. This shows a steep peak in O_{water}-surface distances at 2.2Å, and a small shoulder at higher bond lengths. This supports the view that the zig-zag pattern at 100% coverage is very stable as there is little O_{water} movement in the surface direction. However, the molecules occasionally orientate themselves so that one hydrogen is pointing away from the surface, perpendicular to it. At this point the O_{water} sits higher above the surface, giving rise to the shoulder on the histogram. Comparing the 100% and 200% coverage data reveals that the lower H_2O molecules in the 200% simulation sat higher on the surface than those at 100% when no upper water layer was present.

As at other percentage coverages, the H-O_{water} bond lengths were calculated. The simulation had a mean bond length of 0.99Å with a standard deviation of 0.02Å for the lower 4 H_2O molecules and 0.98Å with a standard deviation of 0.02Å for the upper 4 molecules. This again suggests that bond fluctuations become less as more H_2O is added to the system. As the bond length of an isolated H_2O is 0.97Å, comparing this to the average bond lengths at all coverages it suggests that the presence of the surface leads to increased bond lengths. This is further supported by the upper H_2O molecules having a smaller average bond length than the lower molecules.

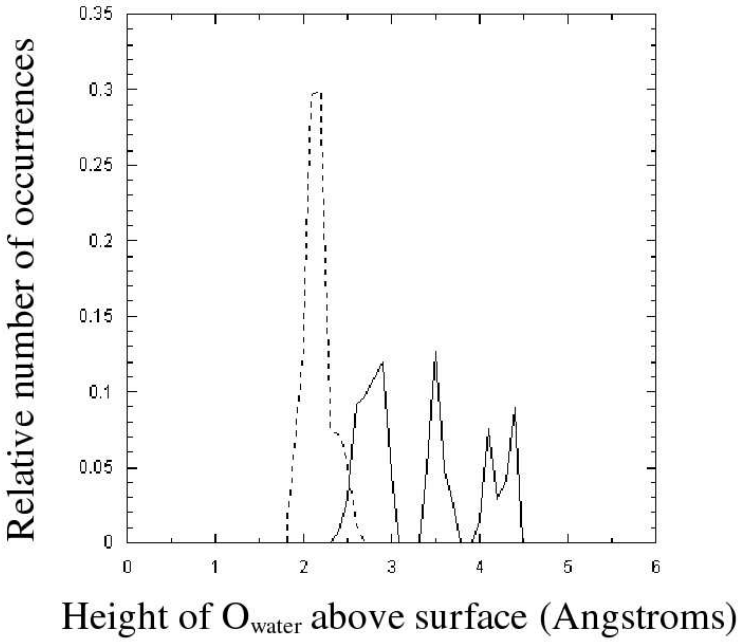

(a)

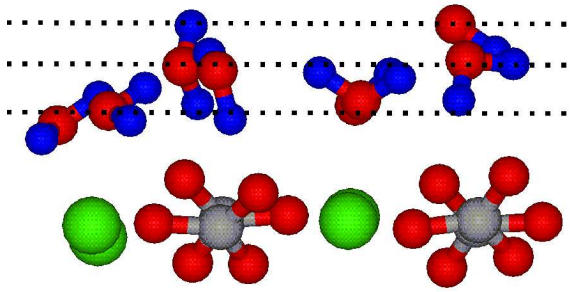

(b)

Figure 5.8: (a) Histogram of height of O_{water} ions above a fixed plane on the calcite surface during a 200% coverage simulation (solid line) and a 100% coverage simulation (dashed line). The simulations were conducted at 300K and data from the final 2ps of the simulations was used to construct the histogram. (The total length of the 100% and 200% coverage simulations were 3.5ps and 5.7ps respectively.) (b) Side view of 200% coverage simulation after relaxation. The dashed lines indicate the O_{water} layers observed during the simulation.

% water coverage	Temperature (K)	Mean H-O_{water} bond length (Å)	Standard deviation (Å)
25%	300	0.99	0.04
25%	600	0.99	0.03
25%	900	0.99	0.06
100%	300	0.99	0.03
200% (lower layer)	300	0.99	0.02
200% (upper layer)	300	0.98	0.02

Table 5.2: Mean H-O_{water} bond lengths and standard deviation at all % water coverages.

5.5 Summary

The MD simulations demonstrated that higher coverages do not stabilise dissociation on the $\{10\bar{1}4\}$ surface. The absence of diffusion or desorption during the 8ps 900K simulation at 25% coverage confirms the strong binding of water to the surface seen in the static relaxations. The observation of elongation of the H-O_{water} bond when the water was orientated towards surface CO_3 ions indicates the H could be shared between the H_2O and CO_3 at these points. As seen in Table 5.2 this fluctuation becomes smaller as more H_2O molecules are added to the surface.

Comparison of the ab-initio simulations with those using classical potentials indicate that the classical simulations have a lower water binding energy. The mean Ca-O_{water} distances showed generally good comparison between the techniques, although some potentials produced closer results than others.

At 100% coverage a zig-zag pattern of water formed. This pattern had previously been obtained using classical simulations [6] and X-ray experiments are consistent with the view that water forms this pattern on the $\{10\bar{1}4\}$ calcite surface [77].

At 200% coverage the zig-zag pattern is lost and no new pattern is established in its place. Analysis of the height of the O_{water} ions above the calcite surface showed that they sit at three distinct heights above the surface. The layering occurs due to H_2O molecules forming hydrogen bonds not only with the surface, but also with other H_2O molecules.

Chapter 6

Molecular dynamics investigation of the calcite-water interface using Quickstep

The previous chapters investigated water on flat, defect-free $\{10\bar{1}4\}$ calcite surfaces. However, real surfaces contain defects such as vacancies and steps. For us to gain a better understanding of the behaviour of water on real calcite surfaces these defects must be included in simulations.

While VASP is a reliable DFT package that has been tested on a wide range of systems, it is limited in how large a calculation can be performed and how long an MD simulation can run. To investigate defective surfaces a large number of atoms is required and it became clear that simulating these systems in VASP was not viable. A static relaxation of an obtuse step was attempted in VASP, but the system remained unconverged after running on four processors for over ten weeks. A new program was therefore sought that would be able to handle larger systems. The ab-initio CP2K code, also known as Quickstep, [78, 79] was found to be capable of performing these calculations. The CP2K code increases the speed of calculation in comparison to VASP and allows systems of up to 1000 atoms to be modelled. Details of the code and the simulations run with water on defective calcite surfaces are presented in this chapter.

6.1 Methods

6.1.1 Quickstep (CP2K)

The efficiency of Quickstep derives mainly from its use of a combination of Gaussian and plane waves in calculations. Atom-centered Gaussian-type basis sets are used to describe the wavefunctions and an auxillary plane wave basis set is used to describe the electron density [79].

The description of the density with plane waves is exploited by the code to obtain the Hartree energy in a time that scales linearly with the number of atoms. Similarly, the use of Gaussian functions, which are localised, allows the Kohn-Sham overlap and density matrix in the basis to become sparse. The matrix becomes more sparse as the system size increases. Eventually, this allows the Kohn-Sham equations to be solved using computing resources that scale linearly with the number of atoms.

All Quickstep calculations are run as gamma point calculations (a k-point mesh of 1 $\times$ 1 $\times$ 1), which means the overall system size must be relatively large (when compared with the size of a calculation in VASP) to obtain accurate results (as discussed in Section 3.1.6). The system size was investigated in convergence calculations that will be described in Section 6.2.2.

In Quickstep, all the information for the calculation is contained in one input file, including the lattice vectors and atom coordinates. All the simulations presented here use GGA with PBE pseudopotentials.

6.2 Convergence tests

Before calculations on defective $\{10\bar{1}4\}$ surfaces could be performed it was desirable to compare the results obtained in Quickstep with those already found using VASP. VASP has been widely used and has been subject to much greater testing than Quickstep, which is a relatively new code. A favourable comparison between the VASP and Quickstep results would create confidence in the results from the new code.

6.2.1 Basis sets

The first parameter to be investigated was the plane wave basis set. As discussed in Section 3.1.6, this is of fundamental importance in a calculation and it was found that the basis set used had a large impact on the quality of results obtained in Quickstep.

Gaussian basis functions are used by Quickstep to describe the wavefunctions. The gaussians take the form $Ne^{-\alpha r^2}$ for 1s, $Ne^{-\alpha r^2}x$ for $2p_x$ etc. When an atom is in a molecule or crystal the orbitals will be affected by other, nearby atoms. To account for this distortion to the orbital a linear combination of gaussians (known as a 'contraction') is used to form a new basis function. Several linear combinations can be combined to form a better basis function if necessary.

As the valence orbitals are often more affected by atomic bonding than the core orbitals, more contractions are sometimes used to describe the valence orbitals. In this case the core orbitals will be described by many primitive gaussians to accurately describe the inner electrons. Polarization functions can also be included, which have a higher 'L' value than in occupied orbitals of the atom. This is mainly for practical reasons, to achieve more accurate results.

Any particular basis set may include any of these complexities. A terminology has therefore been developed that allows us to know what is included in any given basis function. For example a contraction is represented by 'zeta' or 'Z' for short, an 'SZ' basis function is therefore a 'single zeta' function with one contraction, a 'DZ' a 'double zeta' function, 'TZ' is a 'triple zeta' function etc. The letter 'V' in a basis set name refers to a basis with only one contraction for core orbitals, but two contractions for the valence orbitals. The presence of polarization functions is denoted by a 'P' in the basis name.

Initially the 'DZVP' (ie. double zeta, one contraction for inner orbital and two contractions for valence orbitals, plus polarization) basis set was used for all atoms in the calculation performed on the calcite-water interface. This resulted in some rather poor results when compared with previous VASP results. The basis sets for carbon, oxygen and hydrogen were therefore changed to TZV2P bases for the simulations. Unfortunately a calcium TZV2P basis set does not exist. A special

calcium basis set was therefore established for use in the $CaCO_3$ crystal based on the DZVP basis set. The original DZVP basis set for calcium had a relatively flat gaussian that spread out over a large distance. This gaussian was not practical in the calcite crystal as its large spread meant it overlapped too much with surrounding atoms. To remedy this, the gaussian was altered to be taller and less diffuse [80].

The change of basis set was found to make a large improvement in the calculations produced in Quickstep and the results presented in this thesis make use of the TZV2P basis sets for carbon, oxygen and hydrogen and the '$CaCO_3$ special' basis set for calcium.

6.2.2 Adsorption energy on the perfect $\{10\bar{1}4\}$ calcite surface

In order to ensure Quickstep reliability, results obtained in Quickstep were compared with those found in VASP. This was necessary as Quickstep is a relatively new code that has not been subjected to the same amount of testing as VASP. VASP is an established code and therefore a favourable comparison between the results obtained in Quickstep and those obtained in VASP would build confidence in the Quickstep output. The adsorption energy of water on the perfect $\{10\bar{1}4\}$ calcite surface was calculated in Quickstep as a test for accuracy.

As Quickstep uses only gamma point calculations, periodic cells larger than those used in VASP are generally required. However, the original size used in VASP was also tested (cell A in Section 4.2, shown in Figure 4.2) for completeness and to provide a direct comparison. This provided a test of how large an effect the cell dimensions had on the final adsorption energies. Quickstep is designed to deal with larger numbers of atoms than VASP. Therefore calculations with a fourth layer of calcite were performed to test for the number of atoms required for good results.

The three sizes of periodic cell used in the adsorption energy calculations were cell A, containing 12 $CaCO_3$ units, with 2 units in the top layer and measuring $18.00\times9.98\times8.10$Å, Cell B, containing 24 $CaCO_3$ units, with 4 units in the top layer and measuring $18.00\times9.98\times16.2$Å and Cell D, containing 48 $CaCO_3$ units, with 8 in the top layer and measuring $18.00\times19.96\times16.2$Å(the surface direction was along

Calculation type	*Position 1* U_{ad} (eV)	*Position 2* U_{ad} (eV)	*Position 3* U_{ad} (eV)
3 layers, cell A no fixed atoms	-0.6977	-1.3355	-1.3455
3 layers, cell B no fixed atoms	-0.6777	-1.2292	-0.9966
3 layers, cell D no fixed atoms	-1.2624	-1.2624	-1.4219
3 layers, cell A base layer fixed	-0.7109	-1.0996	-0.9269
3 layers, cell B base layer fixed	-0.6910	-1.1362	-0.9435
3 layers, cell D base layer fixed	-0.7574	-0.7442	-0.9435
4 layers, cell A_b base layer fixed	-0.6844	-1.0930	-0.9435
4 layers, cell B_b base layer fixed	-0.6977	-0.8505	-0.9368
4 layers, cell D_b base layer fixed	-0.6910	-0.8770	-0.9435
VASP 3 layers, cell A base layer fixed	-0.629	-0.636	-0.909

Table 6.1: Adsorption energies (U_{ad}) for an isolated H_2O on the calcite $\{10\bar{1}4\}$ surface in different sized cells and with differing numbers of calcite layers in Quickstep. The adsorption energies calculated in VASP are also shown for comparison.

the x-axis). When a fourth layer of calcite was added to the periodic cell the length of the x-vector was increased from 18.00Å to 21.5Å. The three cells to which this applied will be referred to as Cell A_b, Cell B_b and Cell D_b

A water molecule was initally placed in the periodic cells in the same three orientations chosen for the VASP calculations (see Section 4.3 and Figures 4.3, 4.4 and 4.5) to allow direct comparison between the two simulation codes. Other than the variation in size and the number of layers, an additional variable was added to the calculations - in some the base layer of the calcite was kept fixed, but in others it was allowed to move. The results of the adsorption calculations are shown in Table 6.1.

Table 6.1 reveals that there is good comparison between the adsorption energies

found in Quickstep and VASP in the low energy configuration (*Position 3*) in almost all types of cell. The exception to this is in cells that have three calcite layers and no fixed base. In these cells the adsorption energy is lower than expected. Similarly, when *Position 1* and *Position 2* are considered the results are much more varied (especially for *Position 2*). The reason for the very low numbers found for the adsorption energy in some cases becomes clear when the final configurations are examined. Figure 6.1 shows two final configurations for *Position 2*, the first is taken from the calculation in cell A_b (adsorption energy of -1.0930eV) and the second from the calculation in cell D_b (adsorption energy of -0.8770eV). The figures reveal that in the relaxation that produced a very low adsorption energy the surface became disordered, with the CO_3 ions rotating in the surface. However, in the relaxation that produced an adsorption energy comparable to that found for VASP, the surface did not become disordered and retained the usual CO_3 ion orientations.

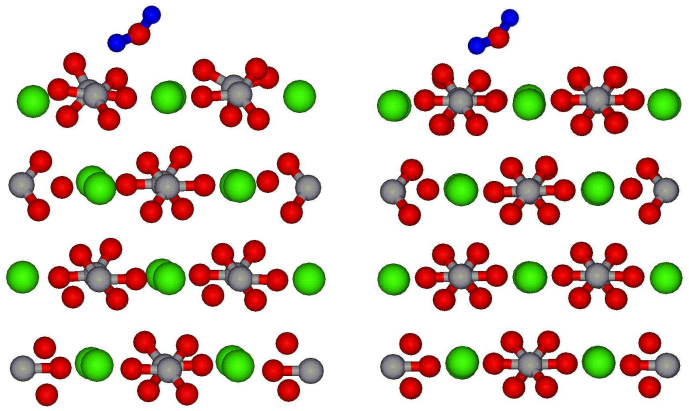

(a) (b)

Figure 6.1: Side views of the final configuration of (a) 4 layer, single cell, calculation with a fixed base and (b) 4 layer, double cell, calculation with a fixed base. In (a) the surface has become disordered during the relaxation, while in (b) the surface structure remains in tact.

These calculations have shown that the adsorption energy obtained in Quickstep is generally comparable to that found for VASP. However, care must be taken to ensure that there are sufficient layers of calcite and that the periodic cell is large enough to achieve reliable results. In all future calculations a periodic cell at least the size of Cell B_b was used.

6.3 Investigation of the imperfect {10$\bar{1}$4} calcite surface interaction with water

After the water adsorption energies found by VASP and Quickstep were found to be consistent it was possible to move on to more complicated systems with confidence. The first system to be investigated was the imperfect {10$\bar{1}$4} calcite surface. A periodic cell with five calcite layers containing 40 $CaCO_3$ units, with 8 units in each layer, was used. To create an imperfect surface one Ca ion and one CO_3 ion were removed from the top layer. Removing one of each ion retained the charge neutrality of the surface and the vacancies were placed as far apart as possible in the cell to limit interactions. The imperfect periodic cell is shown in Figure 6.2.

A series of calculations were then performed in this cell. These calculations investigated the interaction of water with the surface vacancies, exploring the possibilty that these sites are the catalyst for water dissociation. A standard procedure was adopted for these calculations. Firstly, a static relaxation was performed to allow atoms to find a low energy position and to remove as much excess energy as possible before an MD simulation was started. Performing a static relaxation before the MD minimised the possibility of a water molecule desorbing because it had been placed in an unfavourable initial position. The MD simulation was then run for a set amount of time (this time differed depending on which system was being investigated). After the MD simulation, a second static relaxation was performed, which gave a water adsorption energy for the configuration found by the MD simulation.

6.3.1 Water above a CO_3 vacancy

A series of static relaxations were performed in which an isolated H_2O was placed above a CO_3 vacancy in the {10$\bar{1}$4} surface. The calculations investigated the best parameters for the simulations on the defective surface along with the most favourable H_2O configuration. The number of layers in the calcite slab were altered and in some calculations the base layer was fixed, while in others all atoms were allowed to move. The H_2O was placed in both associated and dissociated configurations. The results of these calculations are shown in Table 6.2. The final configurations of the calculations with five layers are shown in Figures 6.3 and 6.4.

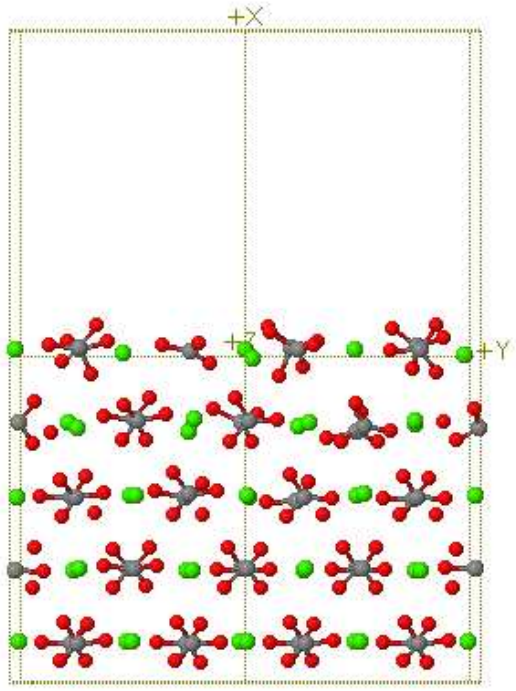

(a)

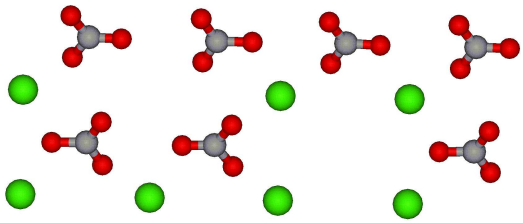

(b)

Figure 6.2: (a) Periodic cell of the imperfect $\{10\bar{1}4\}$ calcite surface. (b) Top layer of defective cell, including Ca and CO_3 vacancies.

Calculation type	Adsorption energy (eV)	
	Associated	Dissociated
4 layers, no fixed atoms	-0.51825	-2.55805
4 layers, base layer fixed	-0.69101	-1.34215
5 layers, base layer fixed	-0.61127*	-1.30228

Table 6.2: Adsorption energies for an isolated H_2O above a CO_3 vacancy. (*The final configuration of this calculation was used as the initial coordinates for the NVT MD simulation.)

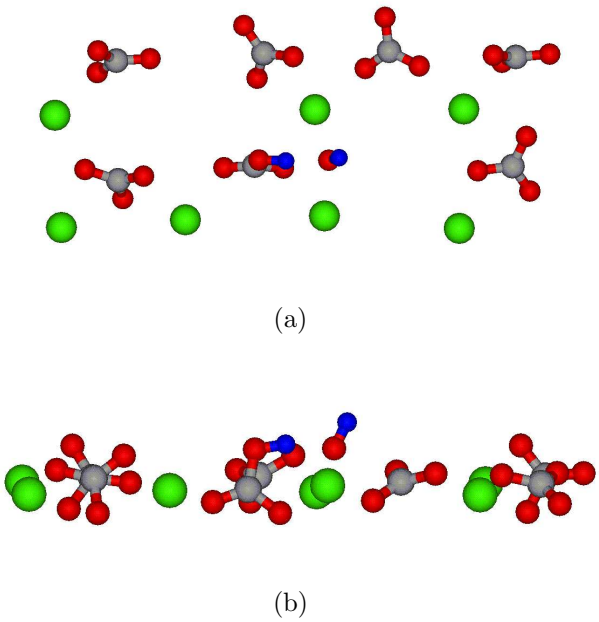

(a)

(b)

Figure 6.3: Final configuration of static relaxation in which a dissociated H_2O molecule was placed above a CO_3 vacancy. (NB 5 layers of calcite were in the original calculation, but only the top layer is shown here for clarity.) (a) Top view. (b) Side view.

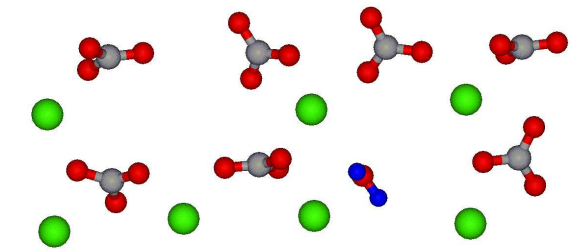

(a)

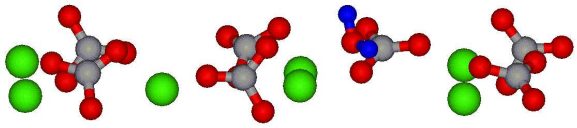

(b)

Figure 6.4: Final configuration of static relaxation in which an associated H_2O molecule was placed above a CO_3 vacancy. (a) Top view. (b) Side view.

The results in Table 6.2 reveal that, above a CO_3 vacancy, dissociated water is more favourable than associated water. By comparing the adsorption energies and observing the ion movement during the relaxation, it is possible to see that the calculations in which the base layer is fixed produce more reliable results, as fixing the base layer gives a 'tether' for upper layers. This observation also suggested that calculations with five layers of calcite were more reliable. Five calcite layers were therefore used in all future calculations of the imperfect surface.

The next step in the procedure was to perform an MD simulation. As this was the first MD simulation to be carried out using Quickstep, a simulation using NVE was undertaken before an NVT simulation was performed. This served as a check that Quickstep could conserve energy in an MD simulation, which proved to be the case.

As the NVE simulation showed that energy could be conserved, NVT simulations could be performed with confidence. To explore more configuration space an NVT MD simulation was run. The starting configuration taken from the final relaxed state of the static relaxation performed with an associated water molecule (marked with a '*' in Table 6.2). The simulation was run for 3.5ps at 300K. This simulation was

designed to investigate whether an H_2O molecule would spontaneously dissociate above a CO_3 vacancy as suggested by the static relaxations, or whether it would remain in its associated state.

During the simulation the water molecule was observed to dissociate after 0.5ps, supporting the finding from the static relaxations that an H_2O molecule favours dissociation above a CO_3 vacancy. Once the H_2O dissociated, the loose H^+ ion joined a surface CO_3 ion, forming an HCO_3. The hydroxyl ion sat nearby between two surface Ca ions, at distances of ∼2.6Å and ∼2.5Å.

An interesting feature of the simulation was the oscillation of the water ion positions. This oscillation resulted in the ions briefly reforming a water molecule before returning to the dissociated state. An analysis of the H-O_{water} bonds, along with the H-$O_{carbonate}$ bond (for the appropriate hydrogen atom) was performed to obtain a quantitive analysis of this fluctuation. The bond lengths were calculated at each time step and the results are shown in Figure 6.5.

From the graphs shown in Figure 6.5 it is clear that the bond between the O_{water} and H(1) (the hydrogen atom that remains in the hydroxyl group after dissociation) does not fluctuate significantly during the simulation, although on closer inspection a small fluctuation at the start of the simulation is visible. The mean bond length is 0.97Å with a standard deviation of 0.02Å (compared to an isolated molecule which has O_{water}-H bonds of 0.97Å in Quickstep). When the standard deviation was calculated, the first 0.5ps of the calculation was excluded from these calculations, ensuring only bond lengths after the H_2O molecule dissociated were included.

The bonds between H(2) (the H-atom that dissociates from the molecule) and the O_{water} and $O_{carbonate}$ are much more interesting. They reveal that after the initial dissociation event the carbonate O-H(2) distance remains almost constant. The mean value is 1.03Å and the standard deviation is 0.05Å. However, the water O-H(2) bond distance continues to fluctuate throughout the simulation. The mean distance is 1.77Å with a standard deviation of 0.2Å. This implies that, while a water molecule appears to reform briefly during the simulation it is not due to the hydrogen 'pulling away' from the CO_3 ion, but the hydroxyl ion moving towards the HCO_3 ion.

The final configuration of the MD simulation was relaxed and the water adsorption

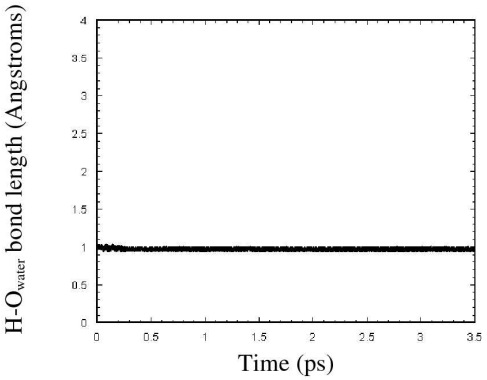

(a)

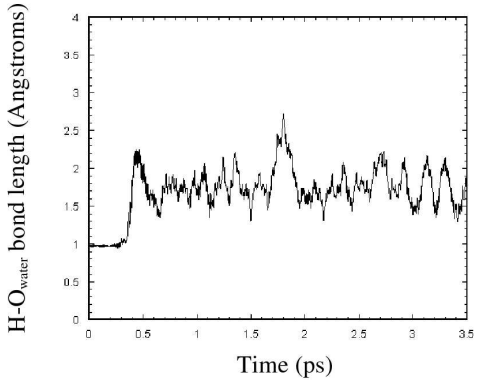

(b)

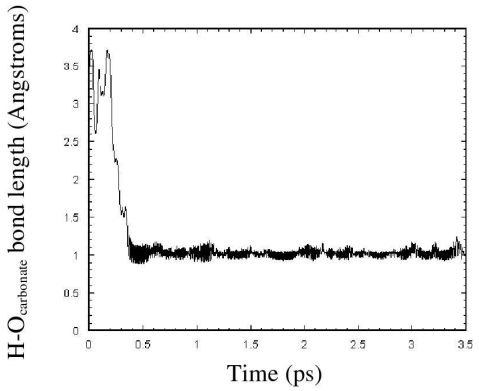

(c)

Figure 6.5: Bond fluctuations during an NVT MD simulation in which an initially associated H_2O molecule dissociated. (a) H(1)-O_{water} bond fluctuation. (b) H(2)-O_{water} bond fluctuation. (c) H(2)-$O_{carbonate}$ bond fluctuation. (H(1) remains bonded to the O_{water}, forming OH. H(2) dissociates and bonds to a CO_3 ion.)

energy was found to be -1.502eV. The H(1)-O_{water} distance was 0.97Å, the H(2)-O_{water} distance was 1.64Å and the H-$O_{carbonate}$ distance was 1.02Å. The dissociation of the H_2O molecule during the MD simulation indicates that CO_3 vacancies are a probable source of dissociated species on the calcite surface.

6.3.2 Water above a Ca vacancy

After water above a CO_3 vacancy had been investigated, Ca vacancies were also tested to explore what effect their presence might have on H_2O. A static relaxation was performed with an H_2O molecule placed above a Ca vacancy in the imperfect $\{10\bar{1}4\}$ surface. During the relaxation, the H_2O molecule remained above the Ca vacancy. The final configuration is shown in Figure 6.6. The water adsorption energy of this configuration was -0.33886eV.

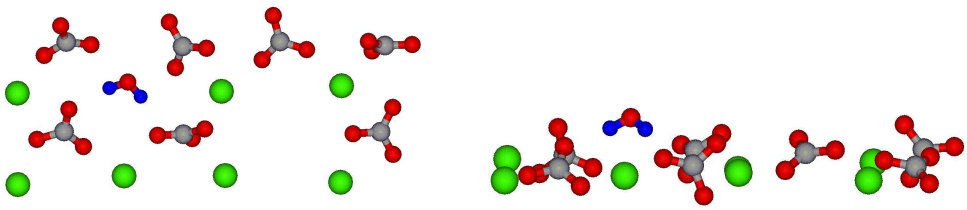

(a) (b)

Figure 6.6: Configuration of an associated H_2O molecule above a Ca vacancy at the end of a static relaxation before an MD simulation was run. (a) Top view. (b) Side view.

After the static relaxation an NVT MD simulation was run for 3ps. During the MD simulation the water molecule was observed to moved away from the Ca vacancy. It diffused across the surface until it formed a bond with the nearest surface Ca ion. The final configuration of the MD simulation, pictured in Figure 6.7, was relaxed. After relaxation the H-$O_{carbonate}$ distances were 1.73Å and 2.36Å, and the Ca-O_{water} distance was 2.48Å. The adsorption energy for this configuration was found to be -1.601eV, which implies the water molecule is strongly bound to the surface.

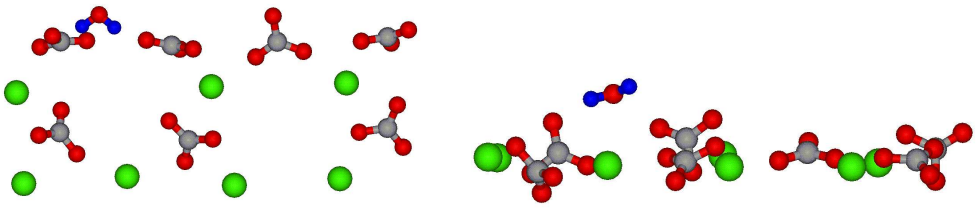

(a) (b)

Figure 6.7: Final configuration of MD simulation of an associated H_2O molecule placed above a Ca vacancy. (a) Top view. (b) Side view.

6.4 Monolayer of water on a defective surface

As an isolated water molecule had been shown to dissociate on the imperfect surface above a CO_3 vacancy, a new simulation was designed to test whether the dissociation was stable when there was more water present on the surface. A simulation with a monolayer of water was performed (a monolayer of water was defined as having the same number of H_2O molecules as there were surface Ca ions). As before, the initial configuration for the MD simulation was obtained by static relaxation. Two initial configurations were chosen for this water coverage, both will be described below.

6.4.1 System A

In the first configuration all the H_2O molecules were associated at the start of the simulation. A standard H_2O orientation was decided upon (taken from the low energy position of an isolated H_2O molecule) and all the H_2O molecules were placed above the surface at this orientation 2.4Å above a surface Ca ion. The initial configuration is shown in Figure 6.8.

During a 3.5ps MD simulation at 300K one of the H_2O molecules (marked as H_2O^{diss} in Figure 6.8) moved away from the Ca ion towards the CO_3 vacancy. Once near the vacancy it dissociated, donating one of its hydrogens to a nearby CO_3, forming a HCO_3 ion. The hydroxyl ion moved to a position inbetween two surface Ca ions at distances of ∼2.4Å and ∼2.6Å, similar to the position taken by an isolated dissociated water molecule. A second water molecule (marked as H_2O^{assoc} in Figure

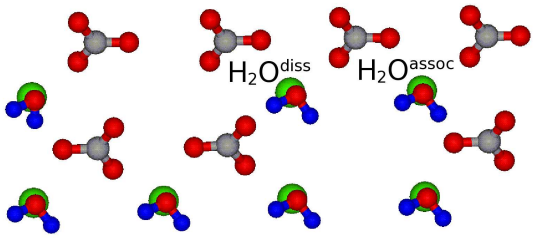

(a)

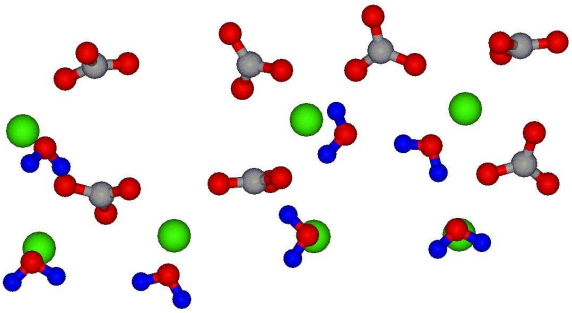

(b)

Figure 6.8: Starting configuration of the monolayer in which all H_2O molecules were initially associated (System A). (a) Before static relaxation. (b) After static relaxation - this configuration was used to initialise the MD simulation.

6.8) then also moved into the vacancy. This molecule remained associated, but was observed to form a hydrogen bond with the hydroxyl ion. The final configuration of the MD simulation is shown in Figure 6.9.

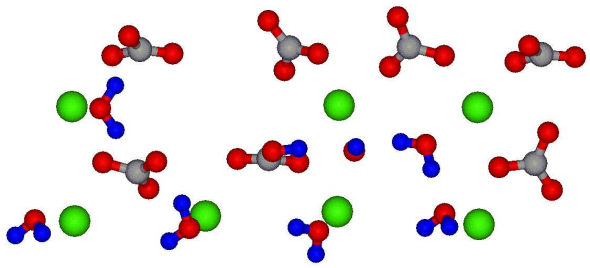

(a)

Figure 6.9: Final configuration of MD simulation during which an H_2O molecule in a monolayer of water dissociated - top view.

The H-O_{water} bonds, along with the H-$O_{carbonate}$ bonds in both these molecules were examined. The bond distances at each time step were calculated, the results are shown in Figures 6.10 and 6.11.

The bond fluctuations shown in Figure 6.10 reveal that the pattern of dissociation in the monolayer is similar to that of an isolated water molecule. In the dissociating H_2O molecule, the H(2)-$O_{carbonate}$ bond fluctuates at the start of the simulation, while the dissociation event is occuring, but does not fluctuate significantly after the dissociation has occured. The H(2)-O_{water} bond, however, continues to fluctuate throughout the simulation.

In Figure 6.11, showing the associated H_2O molecule, neither H-O_{water} bond varies much during the calculation. This suggests the water molecule that moves into the vacancy is stable, and is not tending towards dissociation. However, the H(2)-$O_{hydroxyl}$ bond (the bond between an H of the associated H_2O and the O from the hydroxyl of the dissociated H_2O) does fluctuate considerably, indicating that the whole of this second H_2O molecule oscillates back and forth in the vacancy.

The final configuration of the MD simulation was used to initiate a static relaxation. After the relaxation, the Ca-$O_{hydroxyl}$ distances were 2.50Å and 2.42Å, the $H_{bicarbonate}$-$O_{hydroxyl}$ distance was 1.77Å and the H_{water}-$O_{hydroxyl}$ distance was 1.82Å.

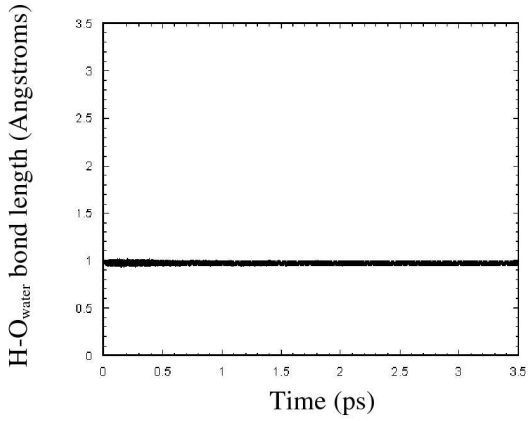

(a)

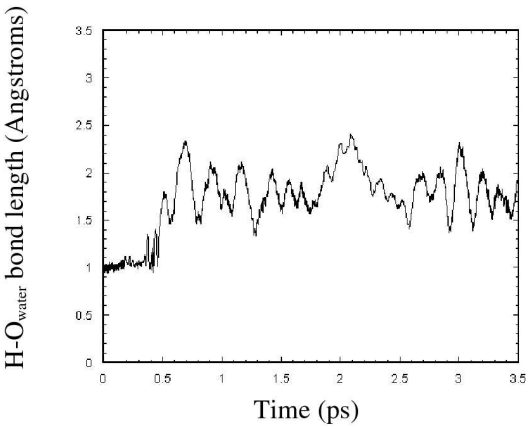

(b)

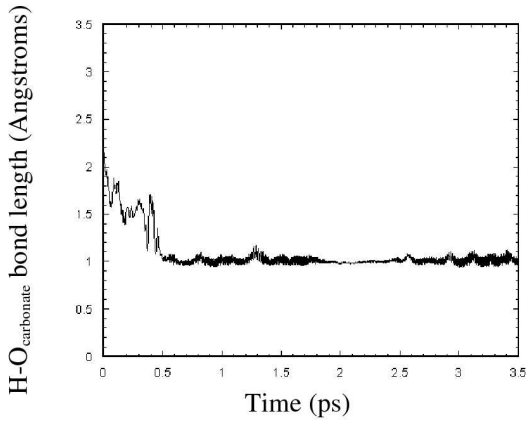

(c)

Figure 6.10: Bond fluctuations of a dissociating H_2O molecule during an NVT MD

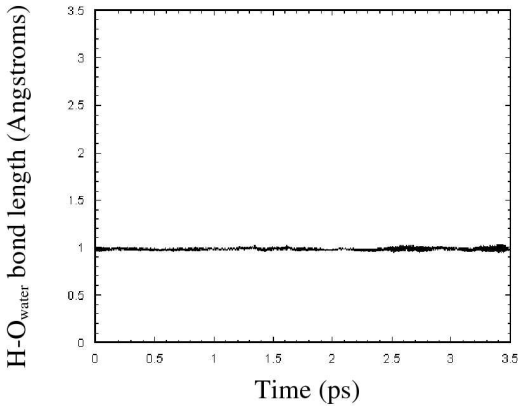

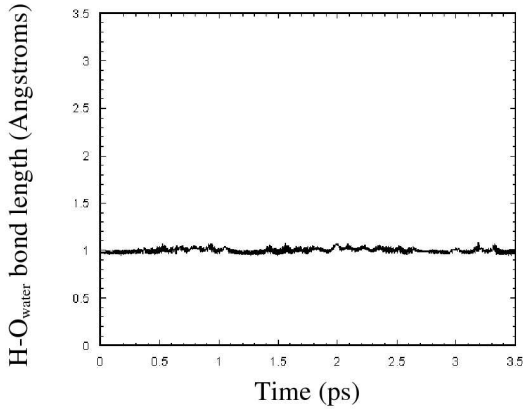

(a)

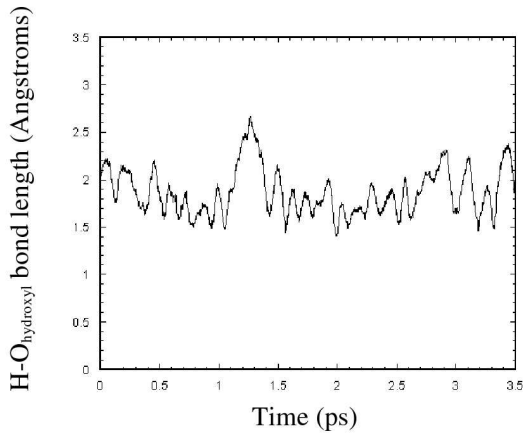

(b)

Figure 6.11: Bond fluctuations of an H_2O molecule that stabilises dissociation during an NVT MD simulation in which an initially associated H_2O molecule dissociated (System A - H_2O^{assoc} molecule). (a) H(1)-O_{water} bond fluctuation. (b) H(2)-O_{water} bond fluctuation. (c) H(2)-$O_{hydroxyl}$ bond fluctuation.

The final adsorption energy was found to be -0.985eV per water molecule. This energy is similar to the adsorption energy of -0.94eV found for water molecules on a perfect $\{10\bar{1}4\}$ surface in Quickstep. However, it is slightly higher in magnitude, indicating that water will favour bonding around vacancies over areas of the surface with a perfect crystal structure.

6.4.2 System B

The second monolayer configuration was initiated with one H_2O molecule already dissociated. To set up the initial state, the configuration from the end of the previous static relaxation of an isolated dissociated water molecule above a CO_3 vacancy was taken as a starting point (see Section 6.3.1). Other water molecules were then placed around the dissociated ions. Most of the associated H_2O molecules were 2.4Å away from a surface Ca ion, however one had to be placed further away, as the hydroxyl ion was sat in the middle of two Ca ions. The starting configuration, and the configuration after static relaxation are shown in Figure 6.12.

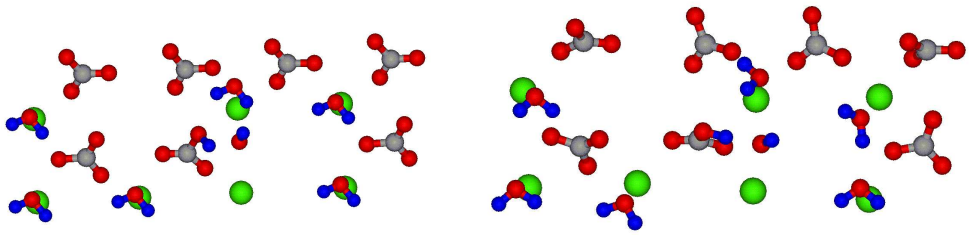

(a) (b)

Figure 6.12: Initial configuration of the monolayer in which one H_2O molecule was initially dissociated, while the others were associated. (a) Before static relaxation. (b) After static relaxation - this configuration was used to initialise the MD simulation.

During a 3.5ps MD simulation at 300K the HCO_3 ion rotated in the crystal and started to pull out of the surface. The ion later moved back into the crystal and ended the simulation only slighty higher in the surface layer than other CO_3 molecules, although it was at an unusual angle. The final MD configuration was relaxed and the adsorption energy was found to be -0.949eV, slightly higher than

for the system that was started with only associated H_2O molecules. This was probably a result of the system being started in an unfavourable position and having to reorientate itself considerably during the simulation. The result was that the HCO_3 ended in an unnatural position, leading to a higher adsorption energy.

6.4.3 Summary of water behaviour on the imperfect {10$\bar{1}$4} calcite surface

Calculations performed on an imperfect $\{10\bar{1}4\}$ surface, which included one CO_3 vacancy and one Ca vacancy, indicated that water dissociation is likely to occur at CO_3 vacancy sites. This vacancy seems to trigger spontaneous dissociation during MD simulations and static relaxations indicate that the dissociated state is energetically favourable when compared to the associated state.

When a water molecule is placed above a Ca vacancy, the tendency of the molecule is to move away from the vacancy to form a bond with the nearest surface Ca ion. It would therefore seem unlikely that Ca vacancies provide a site of dissociation on the calcite surface and are likely to be sites of H_2O absence. However, a high binding energy was found for an H_2O molecule around a Ca vacancy, therefore it would be expected that H_2O molecules around the Ca vacancy will be strongly bound to the surface.

Simulations with a monolayer of water showed dissociation above the CO_3 vacancy. Only one water molecule becomes dissociated during the MD simulation. This dissociation appears to be stabilised by adjacent water molecules. These molecules remain associated and show no sign of dissociation themselves. This implies only one H_2O molecule dissociates per CO_3 vacancy - it does not produce a 'knock-on' effect causing neighbouring H_2O molecules to dissociate.

It seems likely that in real calcite surfaces CO_3 vacancies provide water dissociation sites. As experimental data is necessarily taken from surfaces that contain some imperfections, it is possible to suggest the dissociated species observed in some experiments originate from these crystal sites.

6.5 Investigation of water behaviour at steps on calcite surfaces

Along with vacancies, steps are a possible trigger site for dissociation on calcite surfaces and have previously been investigated using classical simulations [9]. Quickstep calculations were therefore extended to include an exploration of the behaviour of water at steps.

6.5.1 The obtuse step

The first step to be investigated was the obtuse step. The $\{3\,\bar{1}\,\bar{2}\,16\}$ surface was chosen for this investigation. When the crystal is cut to produce this surface the steps are as close together as possible for any calcite surface. This surface therefore has the highest possible density of obtuse steps. Figure 6.13 shows a side view of the plane with the obtuse step clearly visible. Two periodic cells are shown to illustrate the distance between steps on the surface. The base layer of the calcite slab was kept fixed in all calculations to represent the bulk.

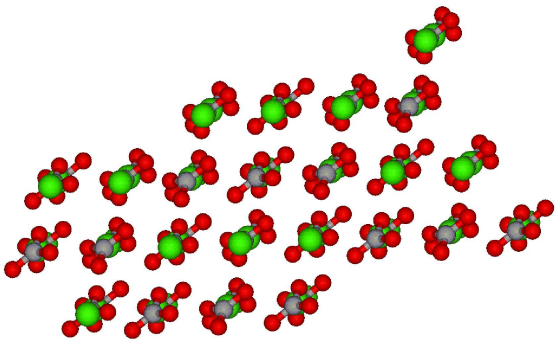

Figure 6.13: Side view of obtuse steps on the $\{3\,\bar{1}\,\bar{2}\,16\}$ surface. Two periodic cells are shown to illustrate the distance between steps. Steps are ∼12Å apart and at an angle of 105^o.

50% water coverage at the step

A series of static relaxations were initially run with an isolated H_2O molecule at an obtuse step on the $\{3\,\bar{1}\,\bar{2}\,16\}$ surface. These calculations were designed to find

the lowest energy configuration for water at the step. Pictures of all the positions attempted are shown in Figure 6.14 and the adsorption energy and final Ca-O_{water} bond distance for each position is shown in Table 6.3.

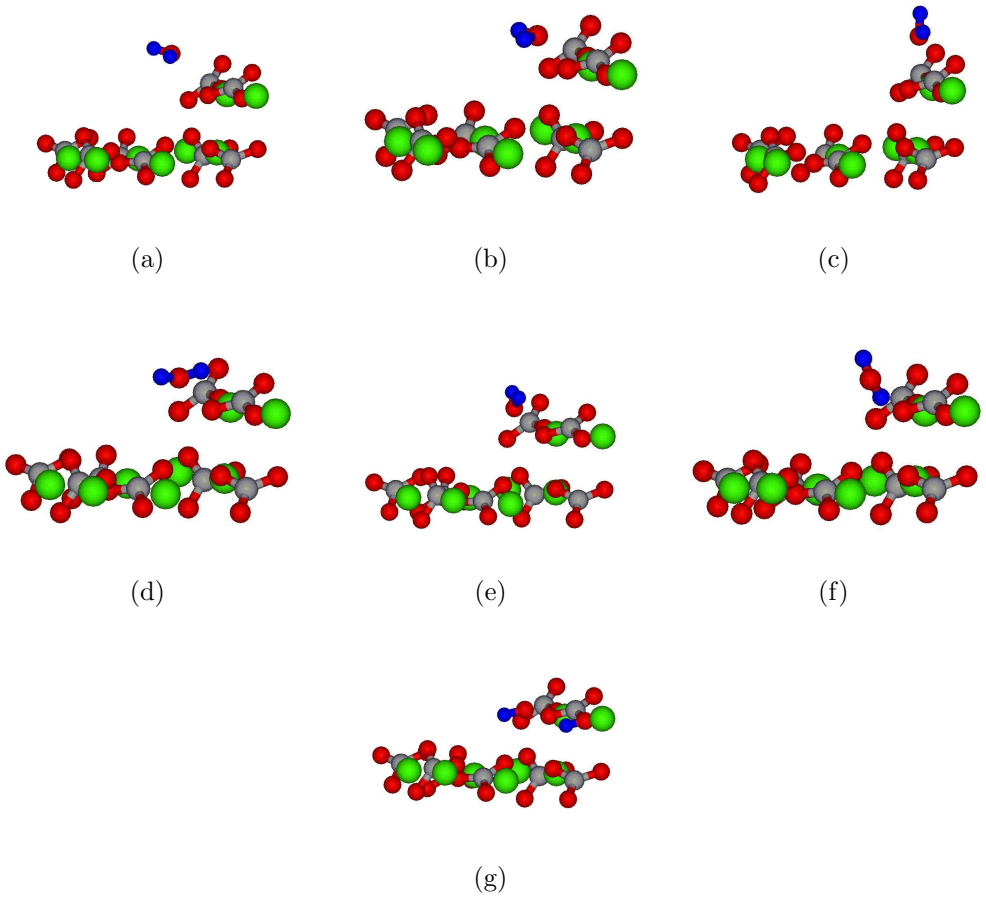

Figure 6.14: The starting configurations for a series of static relaxations of an H_2O molecule at an obtuse step. (a) *Associated, Position 1* (b) *Associated, Position 2* (c) *Associated, Position 3* (d) *Associated, Position 4* (e) *Associated, Position 5* (f) *Associated, Position 6* (g) *Dissociated, Position 1*

From Table 6.3 it is clear that all the different initial configurations for an associated H_2O molecule have resulted in similar final adsorption energies. When the final configuration of each relaxation is visualised, it is revealed that in all calculations the H_2O molecule finished in essentially the same position. The lowest energy position was for the *Associated, Position 3* calculation. The final configuration of this calculation is shown in Figure 6.15. In the relaxation started with a dissociated H_2O molecule, the adsorption energy is positive, indicating that this is very unfavourable

Calculation type	Adsorption energy (eV)	Ca-O_{water} bond distance (Å)
Associated Position 1	-0.850	2.51
Associated Position 2	-0.804	2.51
Associated Position 3	-0.897	2.47
Associated Position 4	-0.850	2.50
Associated Position 5	-0.784	2.49
Associated Position 6	-0.837	2.51
Dissociated Position 1	+3.541	–

Table 6.3: Water adsorption energies and Ca-O_{water} distances for an H_2O molecule on the obtuse step.

and that dissociation is unlikely to occur at the obtuse step.

An MD simulation was run for 3.5ps at 300K starting from the final configuration of the *Associated, Position 3* static relaxation. During the MD simulation the H_2O molecule did not vary its position greatly from that found during the static relaxation. At the end of the simulation the Ca-O_{water} distance was 2.59Å. The final configuration was relaxed and the adsorption energy was found to be -0.970eV. The final configuration of this relaxation is shown in Figure 6.16. It can be noted from the visualisation that the H_2O molecule has positioned itself on top of the step, and has orientated itself so that the hydrogen atoms are directed towards the terrace. After relaxation, the Ca-O_{water} distance was 2.53Å, the H(1)-O_{carb-S}[1] distance was 1.95Å, the H(2)-O_{carb-S} distance was 4.10Å and the H(2)-O_{carb-T} distance was 2.04Å, indicating that H(2) is forming a bond with an $O_{carbonate}$ on the terrace, rather than on the step edge. The magnitude of the adsorption energy of an H_2O molecule on the perfect $\{10\bar{1}4\}$ surface was 0.94eV, indicating that an H_2O at an obtuse step edge is slightly more strongly bound than on a flat surface.

[1]Ions in the step will be denoted by '-S' and ions in the terrace will be denoted by '-T'.

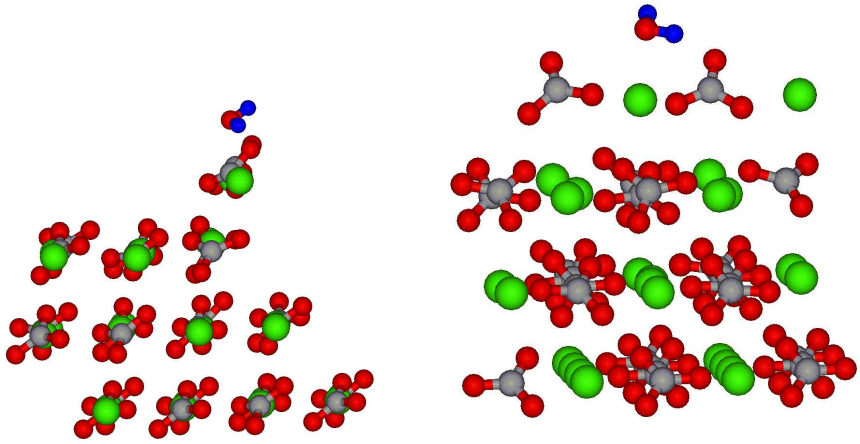

(a) (b)

Figure 6.15: Final configuration of the static relaxation *Associated, Position 3*. (a) Side view. (b) Front view - looking directly at the step.

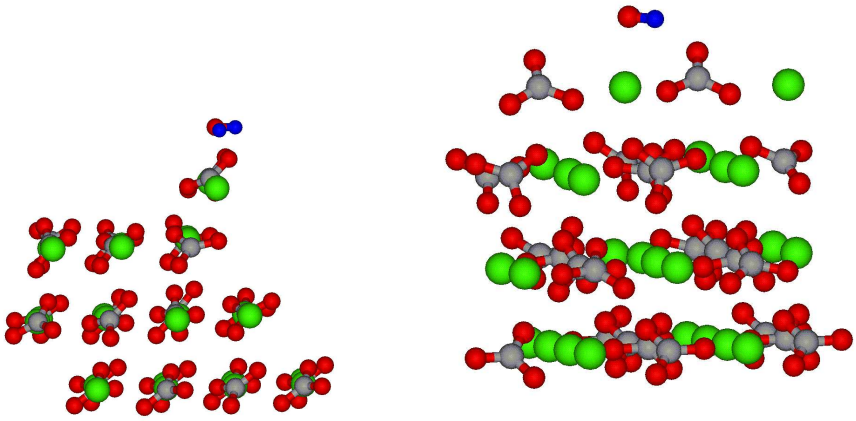

(a) (b)

Figure 6.16: Configuration of water at an obtuse step after relaxation of the MD simulation. (a) Side view. (b) Front view - looking directly at the step.

100% water coverage at the step

A calculation was set up in which there were two H_2O molecules at the obtuse step in the periodic cell. This equated to 100% coverage of the step (one H_2O per Ca ion exposed in the step edge). The two molecules were both positioned in the configuration found to be most stable at 50% coverage (*Associated, Position 3*). A static relaxation was performed and one of the H_2O molecules was seen to turn round so that the molecules were facing opposite directions on the surface (similar to the pattern found on the perfect surface at 100% coverage in VASP, see section 4.3).

An MD simulation was then run for 3.5ps at 300K. Neither molecule moved a large amount during the simulation. The Ca-O_{water} distances were measured at the end of the calculation and were found to be 2.51Å for the H_2O facing 'towards' the step and 2.50Å for the H_2O facing 'away from' the step (as opposed to 2.49Å and 2.48Å at the start of the simulation).

A static relaxation was performed starting from the end of the MD simulation. After relaxation, the water adsorption energy was -1.0235eV per H_2O molecule. The final configuration is shown in Figure 6.17 and the bond distances are shown in Table 6.4.

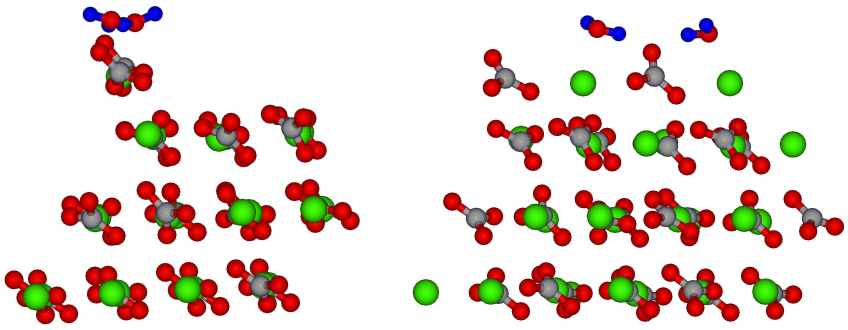

(a) (b)

Figure 6.17: Final configuration after static relaxation of MD simulation of 100% water coverage at the obtuse step (a) Side view. (b) Front view - looking directly at the step.

Bond being measured	Left-hand H_2O measurement (Å)	Right-hand H_2O measurement (Å)
Static relaxation before MD simulation		
Ca_S-O_{water}	2.49	2.48
H(1)-O_{carb-S}	1.68	–
H(2)-O_{carb-T}	3.03	–
H(2)-O_{carb-S}	–	3.30
H(1)-O_{carb-T}	–	0.44
Static relaxation after MD simulation		
Ca_S-O_{water}	2.51	2.51
H(1)-O_{carb-S}	1.72	–
H(2)-O_{carb-T}	2.55	–
H(2)-O_{carb-S}	–	1.88
H(1)-O_{carb-T}	–	4.96

Table 6.4: Bond distances between the H_2O molecules and the obtuse step before and after an MD simulation at 100% step coverage. Left and right hand refers to positions in respect to Figure 6.17(b).

6.5.2 The acute step

The second possible step on the calcite surface is the acute step. The $\{31\bar{4}8\}$ surface was modelled, which contains acute steps at the highest possible density. A side view of the surface is shown in Figure 6.18. The base layer of the calcite slab was kept fixed in all calculations to represent the bulk, providing an anchor for the upper crystal.

50% water coverage at the step

One H_2O molecule was placed in the periodic cell at the step edge, which was equivalent to 50% water coverage of the step. Static relaxations were performed with the molecule at six different orientations and in one dissociated configuration. These configurations are illustrated in Figure 6.19. At the end of the relaxation, the water adsorption energies were calculated and the Ca-O_{water} bond distances were measured. The results are shown in Table 6.5.

When the final configurations of the associated calculations are visualised it is clear that, similar to on the obtuse step, the H_2O molecule has reorientated itself to almost

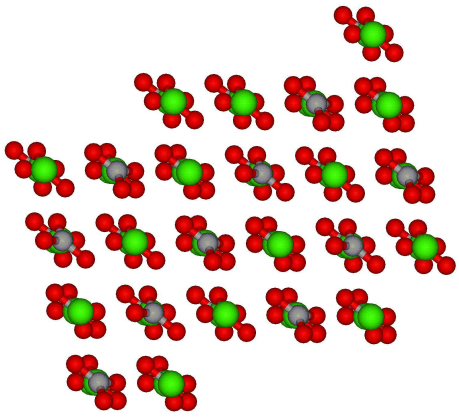

Figure 6.18: A side view of the $\{31\bar{4}8\}$ surface. Two periodic cells are shown to illustrate the distance between steps. The distance between steps is ∼9.5Å and the step has an angle of 80^o.

Calculation type	Adsorption energy (eV)	Ca_T-O_{water} (Angstroms)	Ca_S-O_{water} (Angstroms)
Associated Position 1	-1.223	2.60	2.64
Associated Position 2	-1.249	2.61	2.61
Associated Position 3	-1.242	2.59	2.64
Associated Position 4	-1.216	2.58	2.71
Associated Position 5	-1.130	2.67	2.70
Associated Position 6	-1.236	2.60	2.63
Dissociated Position 1	+1.522	–	–

Table 6.5: Water adsorption energies and Ca-O_{water} distances for an H_2O molecule on the acute step after static relaxation.

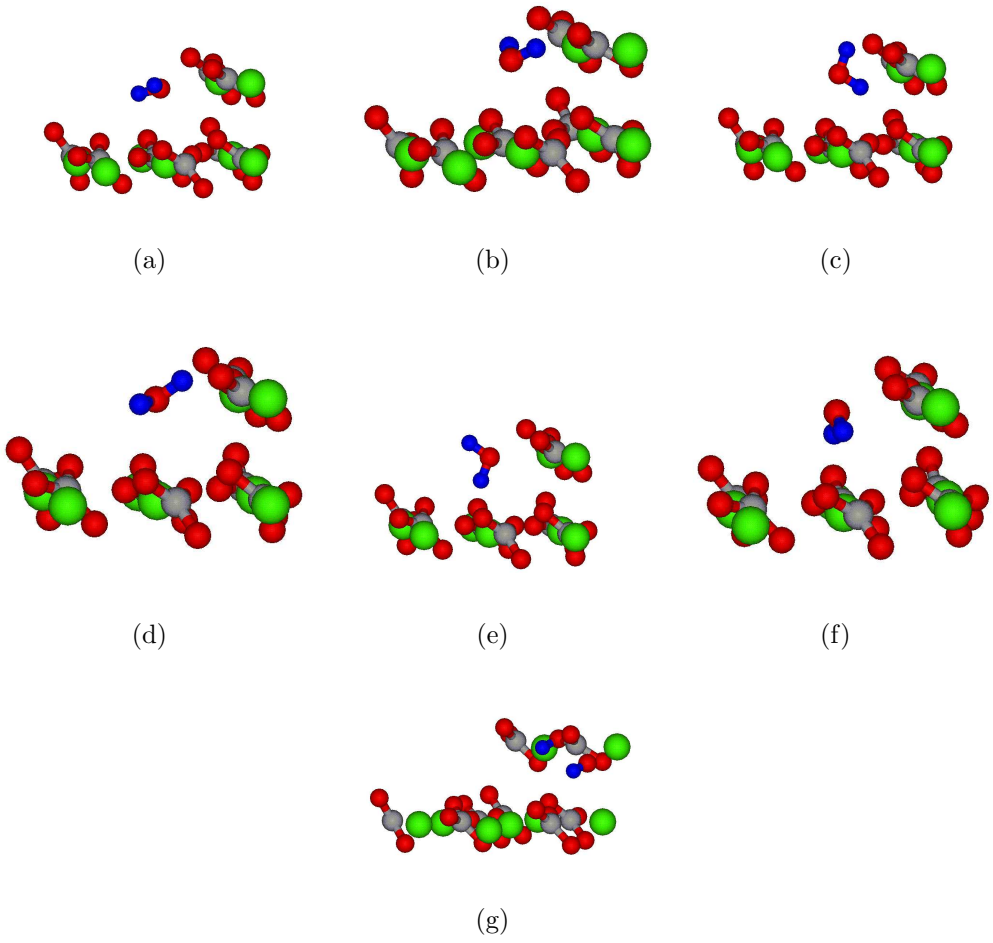

Figure 6.19: The starting configurations for a series of static relaxations of an H_2O molecule at an acute step. (a) *Associated, Position 1* (b) *Associated, Position 2* (c) *Associated, Position 3* (d) *Associated, Position 4* (e) *Associated, Position 5* (f) *Associated, Position 6* (g) *Dissociated, Position 1*

exactly the same position in every relaxation. This is also evident in Table 6.5, where it can be seen that, in all the calculations with an associated H_2O molecule, the water adsorption energies are almost the same. At the acute step, the H_2O molecule forms a bond with two surface Ca ions. Therefore two Ca-O_{water} distances were measured, one between the O_{water} and a terrace Ca ion (Ca_T) and one between the O_{water} and a Ca ion in the step edge (Ca_S). The Ca-O_{water} distances were similar for all the associated configurations, which would be expected as they all assumed a similar position after relaxation. The calculation performed for a dissociated H_2O molecule resulted in a positive adsorption energy, indicating that dissociation is not favourable at the acute step.

The *Associated, Position 2* calculation can be seen to be the most stable in Table 6.5. The final configuration of this calculation is shown in Figure 6.20. An MD simulation at 300K was run for 3.5ps starting with the atoms in these positions. At the end of the simulation the Ca_T-O_{water} distance was 2.83Å and the Ca_S-O_{water} distance was 2.78Å (at the start of the simulation they were both 2.61Å), indicating that during the MD the H_2O molecule sat slightly higher on the surface. No dissociation was observed during the simulation, and there was no indication that the molecule would dissociate during a longer simulation.

After the MD simulation, the final configuration was relaxed. The final O_{water}-Ca_T distance was 2.74Å and the O_{water}-Ca_S distance was 2.65Å, indicating the O_{water} was shared between the two Ca ions. One hydrogen formed a bond with an $O_{carbonate}$ in the terrace at a distance of 3.06Å, while the other hydrogen formed a bond with an $O_{carbonate}$ in the step at a distance of 2.69Å. The final configuration is shown in Figure 6.21. The water adsorption energy was found to be -1.395eV, which, when compared with the adsorption energy on a flat surface (-0.94eV), indicates the water is very strongly bound to the surface in this position.

100% water coverage at the step

A second H_2O molecule was then added to the acute periodic cell, equating to 100% coverage of the step. Both H_2O molecules were placed in the position found to be favourable at 50% coverage (*Associated, Position 2*). A static relaxation was then performed and the adsorption energy of the final configuration was calculated to be

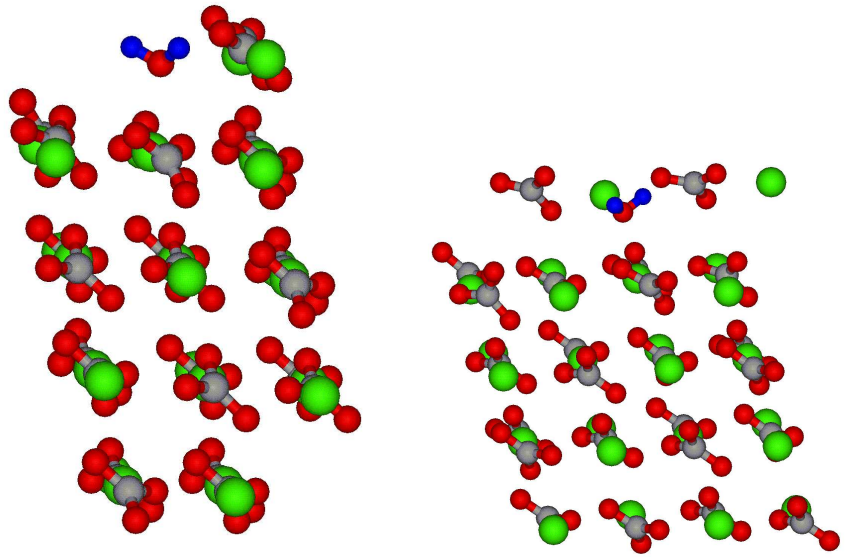

(a) (b)

Figure 6.20: Final configuration of the calculation *Associated, Position 2* on the acute step. (a) Side view. (b) Front view - looking directly at the step.

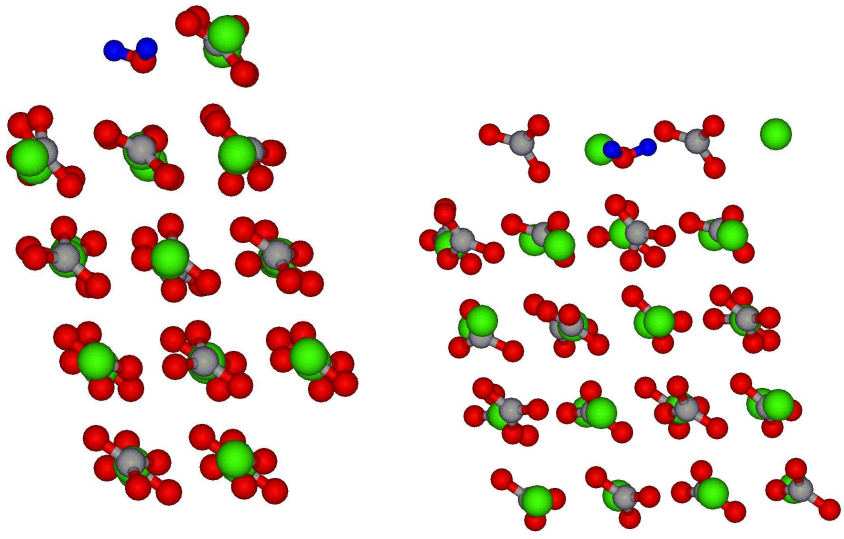

(a) (b)

Figure 6.21: Final configuration of a static relaxation after an MD simulation of *Associated, Position 2* - 50% coverage of the acute step. (a) Side view. (b) Front view - looking directly at the step.

-1.219eV per H_2O molecule. The final configuration of the static relaxation is shown in Figure 6.22 and the bond distances are shown in Table 6.6.

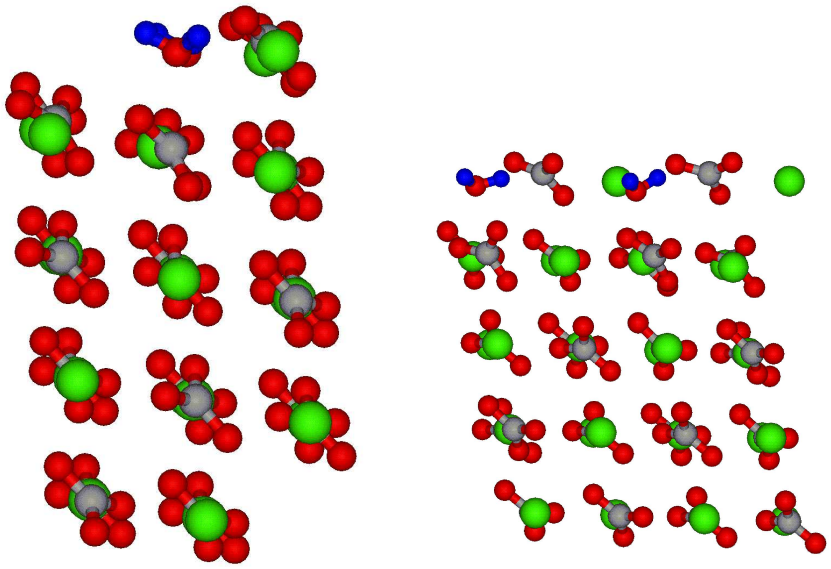

(a) (b)

Figure 6.22: Final configuration of static relaxation with 100% coverage of the acute step. (a) Side view. (b) Front view - looking directly at the step.

An MD simulation was run for 3.5ps at 300K, starting from the final position of the static relaxation. The molecules largely remained in their initial positions during the simulation and did not rotate or diffuse. A static relaxation was then performed, with the starting configuration taken from the final MD coordinates. The final configuration is shown in Figure 6.23 and the bond distances after this relaxation are shown in Table 6.6. These indicate there was a slight shift during the simulation away from the initial positions, but not a substantial movement. However, it is interesting to note that the right-hand molecule formed shorter bonds with the surface than the left-hand molecule. This indicates the molecules were sitting at slightly different positions on the surface. The water adsorption energy per H_2O for this configuration was found to be -1.249eV. Similar to at 50% coverage, although slightly lower in magnitude, this indicates water at the acute step is more strongly bound than on a flat surface.

Bond being measured	Left-hand H_2O measurement (Å)	Right-hand H_2O measurement (Å)
Static relaxation before MD simulation		
Ca_T-O_{water}	2.66	2.61
Ca_S-O_{water}	2.66	2.63
H(1)-O_{carb-S}	2.12	1.69
H(2)-O_{carb-T}	3.23	2.79
Static relaxation after MD simulation		
Ca_T-O_{water}	2.66	2.60
Ca_S-O_{water}	2.64	2.66
H(1)-O_{carb-S}	3.87	1.59
H(2)-O_{carb-T}	4.17	2.75

Table 6.6: Bond distances between the H_2O molecules and the acute step before and after an MD simulation at 100% step coverage. Left and right hand positions are given in respect to Figure 6.22(b).

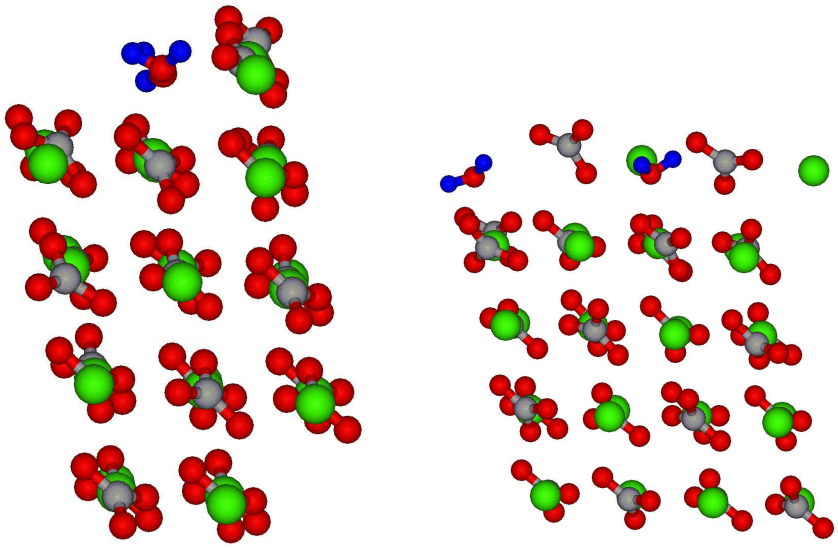

(a) (b)

Figure 6.23: Final configuration of a static relaxation started from the final configuration of an MD simulation of 100% water coverage at the acute step. (a) Side view. (b) Front view - looking directly at the step.

6.5.3 Summary of water behaviour at steps

Calculations of water at both obtuse and acute steps have been performed. While they were initially considered as possible sites of dissociation, no evidence of dissociation was found during any of the simulations performed, and when a water molecule was manually dissociated it was not found to be energetically favourable. This strongly suggests water remains in an associated form at both obtuse and acute steps on the calcite surface.

When the water adsorption energy is calculated for H_2O molecules adsorbed at steps it was found to be noticebly higher in magnitude than for H_2O molecules adsorbed on a flat calcite surface. This was particularly true at acute steps, where the difference between an isolated H_2O on a flat surface and an isolated H_2O at the step was $\sim$0.3eV. This implies that H_2O molecules bind more strongly at steps than on the flat surface. This will impact on the way in which calcite crystals grow in aqueous environments. In the past, experiments have shown that precipitation preferentially happens at the top of obtuse steps [36]. As water will have to be displaced before precipitation can occur, it is perhaps not unexpected that the step with lower water binding energy is the prefered step.

6.6 Summary

Ab-initio simulations of water on imperfect surfaces have revealed CO_3 vacancies as likely sites of water dissociation. However, Ca vacancies and both acute and obtuse steps do not appear to trigger dissociation.

Table 6.7 shows the adsorption energies for water on the surfaces investigated (vacancies, acute steps and obtuse steps). These energies indicate that water is more strongly bound to the surface at defects than on a perfect $\{10\bar{1}4\}$ surface. In particular, water near a Ca vacancy is particularly strongly bound. This water does not sit directly in the Ca vacancy, but binds to a nearby surface Ca ion.

At a CO_3 vacancy, dissociated water was found to be energetically favourable in initial static relaxations and this was confirmed by the spontaneous dissociation of an H_2O molecule during an MD simulation.

Calculation description	Adsorption energy per H_2O (eV)
H_2O on perfect $\{10\bar{1}4\}$ surface	-0.94
H_2O above CO_3 vacancy (dissociated)	-1.50
H_2O above Ca vacancy (associated)	-1.60
Monolayer on imperfect $\{10\bar{1}4\}$ surface (inc. Ca CO_3 vacancies)	-0.99
50% coverage at obtuse step	-0.97
100% coverage at obtuse step	-1.02
50% coverage at acute step	-1.40
100% coverage at acute step	-1.25

Table 6.7: Adsorption enerigies of H_2O molecules on defective calcite surfaces (including at vacanies and at obtuse and acute steps) calculated in Quickstep.

At both obtuse and acute steps, H_2O was found to bond at specific orientations. Calculations that imposed dissociation on the H_2O molecule were shown to be very energetically unfavourable.

Kerisit et al have previously suggested that nonstoichiometric surfaces could play a signficant role in the chemistry of calcite surfaces through their ab-initio work on defective surfaces [35]. Classical simulations on the $\{10\bar{1}3\}$ stepped surface gave a water adsorption energy of -111.9kJmol^{-1} (-1.16eV) at the equivalent of 100% step coverage and a calculation on the stepped $\{10\bar{1}5\}$ surface gave an adsorption energy of -72.2kJmol^{-1} (-0.75eV) at the equivalent of 100% step coverage [8]. The O_{water} at the $\{10\bar{1}3\}$ surface step was coordinated to a Ca ion in the step edge at a distance of 2.47Å and a hydrogen was coordinated with an oxygen in the step edge at a distance of 1.76Å. The O_{water} in the H_2O molecules at the $\{10\bar{1}5\}$ surface step orientated themselves in two different ways. In the first orientation the O_{water}-Ca_S was 2.39Å and in the second it was 2.52Å. The hydrogen bond distances were $\sim$2Å in both molecules. The adsorption energies of the classical simulations are lower in magnitude than those found by the ab-initio simulations, indicating less strong binding.

Chapter 7

Summary and Conclusions

The work in this thesis has investigated the interaction between water and the $\{10\bar{1}4\}$ calcite surface through the use of ab-initio calculations. The motive behind exploring this interaction came from discrepancy between previous experimental and theoretical results; experiments suggested water dissociated on the calcite $\{10\bar{1}4\}$ surface while theoretical calculations suggested the opposite.

One aim of this thesis has therefore been is to shed some light on this contradiction and to try and explain the discrepancy. However, it is also hoped that a better fundamental understanding of the interaction between calcite and water will provide a reliable base for future simulations on a larger scale.

Initially static relaxations were performed on the perfect $\{10\bar{1}4\}$ surface of calcite (Chapter 4), which established a low energy position for water on the surface. These calculations were followed by MD simulations on the same surface (Chapter 5) that allowed more configuration space to be explored. Finally simulations on imperfect $\{10\bar{1}4\}$ surfaces were performed (Chapter 6). These calculations included simulations of water above CO_3 and Ca vacancies as well as simulations of water at the obtuse and acute steps.

Static calculations at a series of water coverages performed using VASP revealed that water is strongly bound to the calcite $\{10\bar{1}4\}$ surface. All coverages up to 100% had similar H_2O adsorption energies. The results of these calculations, along with others in this thesis, are summarised in Table 7.1.

The surface energy was observed to decrease as more water was added to the surface during calculations, which implies water has a stabilising effect. At 200% coverage the surface energy became negative, suggesting more energy is gained from the interaction of the H_2O with the surface than is lost by creating it.

When these findings were compared with previous work they were found to be largely consistent. Classical simulations performed by De Leeuw and Parker also found that the surface energy decreased as more water was added to the surface [6, 8] and that the adsorption energy was -79.1kJmol^{-1} (-0.82eV) at both 12.5% and 100%. Other previous classical simulations performed by Wright et al. at 100% coverage (using a different potential from that of de Leeuw and Parker) found a lower surface energy and less stongly bound water, with an adsorption energy of -53.9kJmol^{-1} (-0.56eV) [39]. The hydrated surface energies presented here are slightly lower, suggesting the ab-initio simulations have stronger binding and a more stable hydrated surface, however the general trend is the same.

In the calculations presented in this thesis, the Ca-O_{water} distance was found to be 2.37Å (on average) at 100% coverage. This compares with a distance of 2.4Å found by De Leeuw and Parker [6, 8] and a distance of 2.55Å found by Wright et al. [39]. These values indicate that, compared with the classical simulations, ab-initio simulations generally have shorter Ca-O_{water} distances and stronger binding.

MD simulations in VASP confirmed the strong binding of water to the $\{10\bar{1}4\}$ surface. Simulations at 25% coverage found desorption did not occur at temperatures as high as 900K. Diffusion and desorption were, however, observed after the temperature had reached 1200K.

At 100% coverage a zig-zag pattern of water formed, this is consistent with previous classical simulations [6] and X-ray experiments [77]. During an MD simulation at 200% coverage the zig-zag pattern was lost and no new pattern was established in its place. Analysis of the height of the O_{water} atoms above the calcite surface showed that they sit at three distinct heights above the surface. This layering occured due to H_2O molecules forming hydrogen bonds not only with the surface, but also with other H_2O molecules.

Table 7.1 shows the strong bonding found at all coverages and all types of surface investigated. It is noticable that on the imperfect surfaces water bonding appears

Calculation description	Adsorption energy per H_2O (eV)	Ca-O_{water} (Å)	H-$O_{carbonate}$ (Å)
VASP calculations			
12.5% coverage perfect surf.	-0.91	2.38	2.00
25% coverage perfect surf.	-0.91	2.39	2.09
33% coverage perfect surf.	-0.88	2.39	1.96
100% coverage perfect surf.	-0.91	2.37	1.95
200% coverage* perfect surf.	-0.74	2.42	2.86
Quickstep calculations			
25% coverage perfect surf.	-0.94	2.47	1.45
Single, dissociated water at CO_3 vacancy	-1.50	–	–
Single, associated water at Ca vacancy	-1.60	2.48	2.05
Monolayer water (inc. diss H_2O) at CO_3 vacancy	-0.99	–	–
50% coverage of obtuse step	-0.97	2.53	2.00
100% coverage of obtuse step	-1.02	2.51	2.91
50% coverage of acute step	-1.40	2.65	2.88
100% coverage of acute step	-1.25	2.64	2.21

Table 7.1: The adsorption energy, Ca-O_{water} and H-O_{water} bond distances for all calculations performed (average bond distances are given when more than one bond of each type was present in a calculation) *At 200% coverage only the lower water molecules were included in the averages.

to be even stronger. It is known from experiments that calcite crystals always have a few layers of absorbed water when in air [81]. The strong binding seen in these calculations corresponds with this observation, as water will favour adsoption to the surface.

The ab-initio calculations performed on the perfect $\{10\bar{1}4\}$ calcite surface did not find any evidence in favour of water dissociation. A metastable dissociated water state was found at 12.5% coverage, however this state was 1.77eV higher in energy than an equivalent associated water state implying it would not occur in nature. No evidence of stable dissociation was found at any of the other coverages.

The H-O_{water} bonds in the MD simulations on this surface were analysed and elongation of the bond was observed when the H_2O molecule was orientated towards a surface CO_3. This indicated the H could be shared between an H_2O and a CO_3 at this orientation. The fluctuation in this bond became smaller as more H_2O molecules were added to the surface, indicating the sharing effect becomes less as more water is added. Overall, these MD simulations support the conclusion that higher coverages do not stabilise dissociation on the $\{10\bar{1}4\}$ surface.

When calculations were extended to explore imperfect calcite surfaces, CO_3 vacancies were revealed as a potential site of dissociation. Ca vacancies, obtuse and acute steps were all also initially considered as potential sites of dissociation, but were found to favour adsorption of associated water. However, at a CO_3 vacancy a water molecule dissociated both during a static relaxation and an MD simulation. Even when a monolayer of water was present on the defective surface, one water molecule would dissociate, although a 'knock-on' effect where this dissociation triggered other nearby water molecules to dissociate was not observed. The dissociation at vacancies would explain the earlier experimental results [82].

The ab-initio calculations presented in this thesis strongly indicate that dissociation of water is unlikely to be found on the perfect $\{10\bar{1}4\}$ calcite surface. Dissociation is also unlikely to occur at either obtuse or acute step edges. However, at CO_3 vacancies water is found to dissociate. At these sites one H_2O molecule will dissociate while the surrounding H_2O molecules will remain associated.

In addition to the discovery of water dissociation at CO_3 vacancies, these calculations have found strong water binding to the calcite surface, it is particularly strong at

defects such as vacancies and steps. This strong binding will have an impact on calcite growth and biomineralization. Biomolecules and other organic molecules will either have to displace the water before binding to the surface or will have to bind to the surface water layer.

Bibliography

[1] R. Frye, editor. *Calcite Group in Encyclopedia of Mineralogy*. Hutchinson Ross Publishing Company, Stroudsbourg, Pennsylvania, USA, 1 edition, 1981.

[2] E. Raisen. The control of scale and corrosion in water systems using magentic fields. In *The International Corrosion Forum Devoted Exclusively to The Protection and Performance of Materials*, 1984.

[3] F. K. Lutgens and E. J. Tarbuck. *Essentials of Geology*. Prentice Hall, Upper Saddle River, New Jersey, USA, 7 edition, 2000.

[4] S. R. Whaley, D. S. English, E. L. Hu, P. F. Barbara, and A. M. Belcher. Selection of peptides with semiconductor binding specificity for directed nanocrystal assembly. *Nature*, 405:665–668, 2000.

[5] K. Henriksen, J. R. Young, P. R. Brown, and S. L. S. Stipp. Coccolith biomineralisation studied with atomic force mircoscopy. *Palaeontology*, 47:725–743, 2004.

[6] N. H. de Leeuw and S. C. Parker. Surface structure and morphology of calcium carbonate polymorphs calcite, aragonite, and vaterite: An atomistic approach. *J. Phys. Chem. B*, 102:2914–2922, 1998.

[7] S. Kerisit, D. J. Cooke, D. Spagnoli, and S. C. Parker. Molecular dynamics simulations of the interactions between water and inorganic solids. *J. Mater. Chem.*, 15:1454–1462, 2005.

[8] N. H. de Leeuw and S. C. Parker. Atomistic simulation of the effect of molecular adsorption of water on the surface structure and energies of calcite surfaces. *J. Chem. Soc., Faraday Trans.*, 93(3):467–475, 1997.

[9] S. Kerisit, S. C. Parker, and J. H. Harding. Atomistic simulation of the dissociative adsorption of water on calcite surfaces. *J. Phys. Chem. B*, 107:7676–7682, 2003.

[10] S.L.S. Stipp. Where the bulk terminates: Experimental evidence for restructuring, chemibonded OH^- and H^+, adsorbed water and hydrocarbons on calcite surfaces. *Molecular Simulation*, 28(6-7):497–516, 2002.

[11] S. L. Stipp and M. F. Hochella Jr. Structure and bonding environments at the calcite surface as observed with X-ray photoelectron spectroscopy (XPS) and low energy electron diffraction (LEED). *Geochimica et Cosmochimica Acta*, 55:1723–1736, 1991.

[12] S. L. S. Stipp. Toward a conceptual model of the calcite surface: Hydration, hydrolysis, and surface potential. *Geochimica et Cosmochimica Acta*, 63:3121–3131, 1999.

[13] S. I. Kuriyavar, R. Vetrivel, S. G. Hegde, A. V. Ramaswamy, D. Chakrabarty, and S. Mahapatra. Insights into the formation of hydroxyl ions in calcium carbonate: temperature dependent FTIR and molecular modelling studies. *Journal of Materials Chemistry*, 10:1835–1840, 2000.

[14] C. L. Freeman, J. H. Harding, D. J. Cooke, J. A. Elliot, J. S. Lardge, and D. M. Duffy. New forcefields for modeling biomineralization processes. *J. Phys. Chem. C*, 111:11943–11951, 2007.

[15] J. H. Harding and D. M. Duffy. The challenge of biominerals to simulations. *J. Mater. Chem.*, 16:1105–1112, 2006.

[16] P. Liu, T. Kendelewicz, G. E. Brown, Jr., and G. A. Parks. Reaction of water with MgO(100) surfaces. Part I: Synchrotron X-ray photoemission studies of low-defect surfaces. *Surface Science*, 412–413:287–314, 1998.

[17] W. Langel and M. Parrinello. Hydrolysis at stepped MgO surfaces. *Physics Review Letters*, 73:504–507, 1994.

[18] W. Langel and M. Parrinello. Ab-initio molecular dynamics of H_2O adsorbed on solid MgO. *Journal of Chemical Physics*, 103:3240–3252, 1995.

[19] L. Giordano, J. Goniakowski, and J. Suzanne. Partial dissociation of water molecules in the (3x2) water monolayer deposited on the MgO (100) surface. *Physical Review Letters*, 81:1271–1273, 1998.

[20] M. Odelius. Mixed molecular and dissociative water adsorption on MgO[100]. *Physical Review Letters*, 82:3919–3922, 1999.

[21] Y. D. Kim, R. M. Lynden-Bell, A. Alavi, J. Stulz, and D. W. Goodman. Evidence for partial dissociation of water on flat MgO(100) surfaces. *Chemical Physics Letters*, 352:318–322, 2002.

[22] J. Goniakowski and M. J. Gillan. The adsorption of H_2O on TiO_2 and SnO_2(110) studied by first-principles calculations. *Surface Science*, 350:145–158, 1996.

[23] R. L. Kurtz, R. Stockbauer, and T. E. Madey. Synchrotron radiation studies of H_2O adsorption on TiO_2(110). *Surface Science*, 218:178–200, 1989.

[24] P. J. Lindan and N. M. Harrison. Mixed dissociative and molecular adsorption of water on the rutile (110) surface. *Physical Review Letters*, 80:762–765, 1998.

[25] P. J. Lindan and C. Zhang. Exothermic water dissociation on the rutile TiO_2(110) surface. *Phys. Rev. B*, 72:075439, 2005.

[26] R. Frye, editor. *Aragonite Group in Encyclopedia of Mineralogy*. Hutchinson Ross Publishing Company, Stroudsbourg, Pennsylvania, USA, 1 edition, 1981.

[27] J. S. Blakemore. *Solid State Physics*. Cambridge University Press, The Pitt Building, Trumpington Street, Cambridge, UK, 2 edition, 1985.

[28] W. A. Deer, R. A. Rowie, and J. Zussman. *An Introduction to the Rock-Forming Minerals*. Longman Group UK Limited, Longman House, Burnt Mill, Harlow, Essex, UK, 2 edition, 1992.

[29] P. Geissbühler, P. Fenter, E. DiMasi, G. Srajer, L. B. Sorenson, and N. C. Sturchio. Three-dimensional structure of the calcite-water interface by surface X-ray scattering. *Surface Science*, 573:191–203, 2004.

[30] Y. Liang, A. S. Lea, D. R. Baer, and M. H. Engelhard. Structure of the cleaved $CaCO_3(10\bar{1}4)$ surface in an aqueous environment. *Surface Science*, 351:172–182, 1996.

[31] S. Hwang, M. Blanco, and W. A. Doddard III. Atomistic simulations of corrosion inhibitors adsorbed on calcite surface I. Force field parameters for calcite. *J. Phys. Chem.*, 105:10746–10752, 2001.

[32] R. Weller. Calcite Photos, Cochise College, April 2009. http://skywalker.cochise.edu/wellerr/mineral/calcite/calcite6.htm.

[33] S. Kerisit and S. C. Parker. Free energy of adsorption of water and calcium on the $\{10\bar{1}4\}$ calcite surface. *Chem. Commun.*, pages 52–53, 2004.

[34] S. Kerisit and S. C. Parker. Free energy of adsorption of water and metal ions on the $\{10\bar{1}4\}$ calcite surface. *J. Am. Chem. Soc.*, 126:10152–10160, 2004.

[35] S. Kerisit, A. Marmier, and S. C. Parker. Ab initio surface phase diagram of the $\{10\bar{1}4\}$ calcite surface. *J. Phys. Chem. B*, 109(39):18211–18213, 2005.

[36] S. L. Stipp, W. Gutmannsbauer, and T. Lehmann. The dynamic nature of calcite surfaces in air. *American Mineralogist*, 81:1–8, 1996.

[37] R. Kristensen and S. L. S. Stipp. Modeling steps and kinks on the surface of calcite. *Journal of Chemical Physics*, 121:8511–8523, 2004.

[38] D. W. Thompson and P. G. Pownall. Surface electrical properties of calcite. *Journal of Colloid and Interface Science*, 131(1):74–82, 1989.

[39] K. Wright, R. T. Cygan, and B. Slater. Structure of the $(10\bar{1}4)$ surfaces of calcite, dolomite and magnesite under wet and dry conditions. *Phys. Chem. Chem. Phys.*, 3:839–844, 2001.

[40] P. Fenter, P. Geissbühler, E. DiMasi, G. Srajer, L. B. Sorensen, and N. C. Sturchio. Surface speciation of calcite observed in situ by high resolution x-ray reflectivity. *Geochim. Cosmochim. Acta*, 64(7):1221–1228, 2000.

[41] N. H. de Leeuw, S. C. Parker, and J. H. Harding. Molecular dynamics simulation of crystal dissolution from calcite steps. *Phys. Rev. B*, 60(19):13792–13799, 1999.

[42] D. Spagnoli, S. Kerisit, and S. C. Parker. Atomistic simulation of the free energies of dissolution of ions from flat and stepped calcite surfaces. *Journal of Crystal Growth*, 294:103–110, 2006.

[43] Y. Liang and D. R. Baer. Anisotropic dissolution at the $CaCO_3(10\bar{1}4)$-water interface. *Surface Science*, 373:275–287, 1997.

[44] S. L. Stipp, M. F. Hochella, Jr., G. A. Parks, and J. O. Leckie. Cd^{2+} uptake by calcite, solid-state diffusion, and the formation of solid-solution: Interface processes observed with near-surface sensitive techniques (XPS,LEED, and AES). *Geochimica et Cosmochimica Acta*, 56:1941–1954, 1992.

[45] S. L. S. Stipp, C. M. Eggleston, and B. S. Nielsen. Calcite surface structure observed at microtopographic and molecular scales with atomic force microscopy (AFM). *Geochimica et Cosmochimica Acta*, 58:3023–3033, 1994.

[46] D. Spagnoli, D. J. Cooke, S. Kerisit, and S. C. Parker. Molecular dynamics simulations of the interaction between the surfaces of polar solids and aqueous solutions. *J. Mater. Chem.*, 16:1997–2006, 2006.

[47] Richard. M. Martin. *Electronic Structure*. Cambridge University Press, The Pitt Building, Trumpington Street, Cambridge, UK, 2 edition, 2005.

[48] Sara M. McMurry. *Quantum Mechanics*. Prentice Hall, Pearson Education Limited, Edinburgh Gate, Harlow, Essex, CM20 2JE, 1 edition, 1993.

[49] P. Hohenberg and W. Kohn. Inhomogeneous electron gas. *Physics Review*, 136(3B):B864–B871, 1964.

[50] W. Kohn and L. J. Sham. Self-consistent equations including exchange and correlation effects. *Physical Review*, 140(4A):A1133A1139, 1965.

[51] J. Perdew and Y. Wang. Accurate and simple analytic representation of the electron-gas correlation-energy. *Phys. Rev. B*, 45:13244–13249, 1992.

[52] John P. Perdew, Kieron Burke, and Matthias Ernzerhof. Generalized gradient approximation made simple. *Physical Review Letters*, 77:3865–5192, 1996.

[53] M. C. Payne, M. P. Teter, D. C. Allan, T. A. Arias, and J. D. Joannopoulos. Iterative minimization techniques for *ab initio* total-energy calculations: molecular dynamics and conjugate gradients. *Reviews of Modern Physics*, 64(4):1045–1097, 1992.

[54] Charles Kittel. *Introduction to Solid State Physics*. John Wiley and Sons, Inc., New York, USA, 7 edition, 1996.

[55] Hendrik J. Monkhorst and James D. Pack. Special points for Brillouin-zone integrations. *Physical Review B*, 13(12):5188–5192, 1976.

[56] Martin Lūders. Electrons in solids. Lecture notes from 'Physics By The Lake', September 2006.

[57] D. Vanderbilt. Soft self-consistent pseudopotentials in a generalized eigenvalue formalism. *Phys. Rev. B*, 41:7892–7895, 1990.

[58] P. E. Blōchl. Projector augmented-wave method. *Physical Review B*, 50(24):17953–17979, 1994.

[59] G. Kresse and D. Joubert. From ultra-soft pseudopotentials to the projector augmented-wave method. *Physical Review B*, 59(3):1758–1775, 1996.

[60] Chè M. S. Gannarelli. *Properties of the Earth's deep interior studied using* ab initio *modelling techniques*. PhD thesis, University College London, 2005.

[61] K. Binder, J. Horbach, W. Kob, W. Paul, and F. Vernik. Molecular dynamics simulations. *Journal of Physics: Condensed Matter*, 16:S429–S453, 2004.

[62] Daan Frenkel and Berend Smit. *Understanding Molecular Simulation: From Alogorithms to Applications*. Academic Press, San Diego, CA, USA, 3 edition, 2000.

[63] A. Pavese, M. Catti, G. D. Price, and R. A. Jackson. Interatomic potentials for $CaCO_3$ polymorphs (calcite and aragonite), fitted to elastic and vibrational data. *Physics and Chemistry of Minerals*, 19:80–87, 1992.

[64] A. Pavese, M. Catti, S. C. Parker, and A. Wall. Modelling of the thermal dependence of structural and elastic properties of calcite, $CaCO_3$. *Physics and Chemistry of Minerals*, 23:89–93, 1996.

[65] K. P. Schroder, J. Sauer, M. Leslie, C. Richard, A. Catlow, and J. M. Thomas. Bridging hydroxyl groups in zeolite catalysts: a computer simulation of their structure, vibrational properties and acidity in protonated faujasites (H-Y zeolites). *Chemical Physics Letters*, 188:320–325, 1992.

[66] G. Kresse and J. Hafner. *Ab initio* molecular dynamics for liquid metals. *Phys. Rev. B*, 47:558–561, 1993.

[67] G. Kresse and J. Hafner. *Ab initio* molecular-dynamics simulation of the liquid-metal-amorphous-semiconductor transition in germanium. *Phys. Rev. B*, 49:14251–14269, 1994.

[68] G. Kresse and J. Furthmüller. Efficient iterative schemes for *ab initio* total-energy calculations using a plane-wave basis set. *Phys. Rev. B*, 54:11169–11186, 1996.

[69] G. Kresse and J. Furthmüller. Efficiency of ab-initio total energy calculations for metals and semiconductors using a plane-wave basis set. *Computational Materials Science*, 6:15–50, 1996.

[70] J. S. Blakemore. *Solid State Physics*. W. B. Saunders Company, 12 Dyott Street, London, WC1, UK, 1 edition, 1969.

[71] Alan Spry. *Metamorphic Textures*. Pergamon Press, 5 edition, 1983.

[72] A. L. Braybrook, B. R. Heywood, R. A. Jackson, and K. Pitt. Parallel computational and experimental studies of the morphological modification of calcium carbonate by cobalt. *Journal of Crystal Growth*, 243:336–344, 2002.

[73] D. Alfé and M. J. Gillan. The energetics of oxide surfaces by quantum Monte Carlo. *Journal of Physics: Condensed Matter*, 18:L435–L440, 2006.

[74] Y. Wang and T. N. Truong. Theoretical study of adsorption of water dimer on the perfect MgO(100) surface: Molecular adsorption versus dissociative chemisorption. *J. Phys. Chem. B*, 108:3289–3294, 2004.

[75] W. Smith and T. R. Forester. DL_POLY_2.0: A general-purpose parallel molecular dynamics simulation package. *Journal of Molecular Graphics*, 14:136–141, 1996.

[76] D. Alfé and M. J. Gillan. *Ab initio* statistical mechanics of surface adsorption and desorption. I. H_2O on MgO (001) at low coverage. *Journal of Chemical Physics*, 127:114709, 2007.

[77] U. Magdans, H. Gies, X. Torrelles, and J. Ruis. Investigation of the 104 surface of calcite under dry and humid atmospheric conditions with grazing incidence X-ray diffraction (GIXRD). *Eur. J. Mineral.*, 18:83–92, 2006.

[78] J. Vande Vondele and J. Hutter. An efficient orbital transformation method for electronic structure calculations. *Journal of Chemical Physics*, 118:4365–4369, 2003.

[79] J. Vande Vondele, M. Krack, F. Mohamed, M. Parrinello, T. Chassaing, and J. Hutter. QUICKSTEP: Fast and accurate density functional calculations using a mixed Gaussian and plane wave approach. *Computer Physics Communications*, 167:103–128, 2005.

[80] Discussion with Matthew Watkins.

[81] J. Bohr, S. L. S. Stipp, P. M. Morris, and R. A. Wogelius. Thickness and structure of the water layer formed from vapour on calcite surfaces. *submitted*, 2009.

[82] S. L. S. Stipp, April 2009. Private email correspondence.